



저작자표시-비영리-변경금지 2.0 대한민국

이용자는 아래의 조건을 따르는 경우에 한하여 자유롭게

- 이 저작물을 복제, 배포, 전송, 전시, 공연 및 방송할 수 있습니다.

다음과 같은 조건을 따라야 합니다:



저작자표시. 귀하는 원저작자를 표시하여야 합니다.



비영리. 귀하는 이 저작물을 영리 목적으로 이용할 수 없습니다.



변경금지. 귀하는 이 저작물을 개작, 변형 또는 가공할 수 없습니다.

- 귀하는, 이 저작물의 재이용이나 배포의 경우, 이 저작물에 적용된 이용허락조건을 명확하게 나타내어야 합니다.
- 저작권자로부터 별도의 허가를 받으면 이러한 조건들은 적용되지 않습니다.

저작권법에 따른 이용자의 권리는 위의 내용에 의하여 영향을 받지 않습니다.

이것은 [이용허락규약\(Legal Code\)](#)을 이해하기 쉽게 요약한 것입니다.

[Disclaimer](#)

# Concentric Tube Robots: Stability Analysis, Optimal Design, and Shape Sensing

JUNHYOUNG HA

SUBMITTED IN PARTIAL FULFILLMENT OF THE  
REQUIREMENTS FOR THE DEGREE OF

DOCTOR OF PHILOSOPHY

in the  
SCHOOL OF MECHANICAL AND AEROSPACE ENGINEERING

at  
SEOUL NATIONAL UNIVERSITY

July 2015



# ABSTRACT

## Concentric Tube Robots: Stability Analysis, Optimal Design, and Shape Sensing

by

Junhyoung Ha

Department of Mechanical and Aerospace Engineering  
Seoul National University

Minimally invasive surgery can involve navigating inside small cavities or reaching around sensitive tissues. Robotic instruments based on concentric tube technology are well suited to these tasks since they are slender and can be designed to take on shapes of high and varying curvature along their length. One limitation of these robots, however, is that elastic instabilities can arise when manipulating the robots by rotating or translating the bases of the tubes. As the tubes rotate and translate with respect to each other, elastic potential energy associated with tube bending and twisting can accumulate; if a configuration is not locally elastically stable,

then a dangerous snapping motion may occur as energy is suddenly released.

To enhance the elastic stability of the concentric tube robots, this paper presents two researches: i) optimal design of tube pair, ii) local stability test to avoid unstable configurations. While prior work has considered tubes of piecewise-constant pre-curvature, the first research in this paper proposes varying tube pre-curvature as a function of arc length as a means to enhance stability. Stability conditions for a planar tube pair are derived and used to define an optimal design problem. This framework enables solving for pre-curvature functions that achieve a desired tip orientation range while maximizing stability and respecting bending strain limits. Analytical and numerical examples of the approach are provided. The second research provide a local stability condition and test to determine if a configuration is a stable equilibrium or not. This condition applies to arbitrary robot designs with any external loads. The local stability test based on this condition is validated by comparison with known stability results, and its utility is demonstrated by application to stable path planning.

Though those two researches address the elastic instability issue of concentric tube robots, they both are based on the theoretical kinematics of the robots. Robot control requires the rapid computation of this kinematics, which involves solving complex mechanics-based models. Furthermore, shape computation based on kinematic input variables can be inaccurate due to parameter errors and model simplification. An alternate approach is to compute the shape in real time from a set of sensors positioned along the length the robot that provide measurements of local curvature, e.g., optical fiber Bragg gratings. In this point of view, the third research in this paper proposes a general framework for selecting the number and placement of such sensors with respect to arc length so as to compute the forward kinematic solution accurately and quickly. The approach is based on

defining numerically efficient shape reconstruction models parameterized by sensor number and location. Optimization techniques are used to solve for the sensor locations that minimize shape and tip error between a reconstruction model and a mechanics-based model. As a specific example, several reconstruction models are proposed and compared for concentric tube robots. These results indicate that the choice of reconstruction model as well as sensor placement can have a substantial effect on shape accuracy.

**Keywords:** Concentric tube robot, continuum robot, elastic stability, shape sensing.

**Student Number:** 2008-22898



# Contents

<b>Abstract</b>	<b>3</b>
<b>List of Tables</b>	<b>11</b>
<b>List of Figures</b>	<b>13</b>
<b>1 Introduction</b>	<b>1</b>
1.1 Contributions of This Thesis . . . . .	4
1.1.1 Achieving Elastic Stability Through Precurvature Optimization	4
1.1.2 Optimizing Curvature Sensor Placement for Fast, Accurate Shape Sensing of Continuum Robots . . . . .	6
1.2 Organization . . . . .	7
<b>2 Achieving Elastic Stability Through Precurvature Optimization</b>	<b>11</b>
2.1 Introduction . . . . .	11
2.2 Kinematics of General Concentric-Tube Robot . . . . .	14
2.3 Kinematics of Planar Tube Pair . . . . .	16
2.4 Stability Condition for Planar Tube Pairs . . . . .	17

2.4.1	Ignoring Straight Transmission Length Inside Collar . . . . .	17
2.4.2	Considering Straight Transmission Length Inside Collar . . . . .	19
2.5	Evaluating Stability for Specific Pre-curvature Functions . . . . .	22
2.5.1	Constant Pre-curvature . . . . .	23
2.5.2	Partially Constant Pre-curvature . . . . .	23
2.5.3	Pre-curvature Function, $\hat{u}_y = \frac{b}{s+a}$ . . . . .	25
2.6	Formulation as an Optimal Design Problem . . . . .	27
2.6.1	Numerical Solution of the Optimal Design Problem . . . . .	29
2.6.2	Analytic Solution of the Optimal Design Problem . . . . .	31
2.6.3	Feasibility of Optimal Design Problem . . . . .	36
2.7	Hardware Experiments . . . . .	37
<b>3</b>	<b>Elastic Stability of Concentric Tube Robots Subject to External Loads</b>	<b>51</b>
3.1	Introduction . . . . .	51
3.2	Concentric Tube Robot Modeling . . . . .	54
3.3	Elastostatic Kinematic Model . . . . .	57
3.3.1	Concentric Tube Robot with No External Load . . . . .	58
3.3.2	Concentric Tube Robot with External Load . . . . .	59
3.3.3	Generalized Force Representation of External loads . . . . .	63
3.4	Evaluating Local Elastic Stability . . . . .	65
3.4.1	Preliminaries . . . . .	65
3.4.2	Jacobi Non-Conjugacy Test for Conservative External Loads . . . . .	66
3.4.3	Physical Interpretation of Jacobi Non-Conjugacy Condition . . . . .	68
3.4.4	Non-Conservative External Loads . . . . .	69
3.5	Examples . . . . .	71

3.5.1	Example 1: Stability of an Unloaded Constant-precvature Tube Pair . . . . .	72
3.5.2	Example 2: Stability of a Constant Precurvature Tube Pair Subject to Elastic Forces . . . . .	73
3.5.3	Example 3: Stability of a Constant-precvature Tube Pair Subject to Constant World-frame Loads . . . . .	77
3.5.4	Example 4: Application to Stable Path Planning . . . . .	80
<b>4</b>	<b>Optimizing Curvature Sensor Placement for Shape Sensing</b>	<b>91</b>
4.1	Introduction . . . . .	91
4.2	Shape Estimation for Continuum Robots . . . . .	94
4.2.1	Kinematics of Continuum Robots . . . . .	94
4.2.2	Shape Reconstruction Models . . . . .	95
4.2.3	Optimal Sensor Location . . . . .	98
4.3	Case Study: Concentric Tube Robots . . . . .	100
4.3.1	Kinematics of Concentric Tube Robots . . . . .	101
4.3.2	Section-Based Principal Component Analysis Model . . . . .	102
4.3.3	Section-based Polynomial Regression Model . . . . .	104
4.4	Numerical Experiments for a Concentric Tube Robot . . . . .	105
4.4.1	Selection of Basis Functions . . . . .	107
4.4.2	Number and Location of Sensors . . . . .	109
4.4.3	Comparison between Reconstruction Models . . . . .	109
<b>5</b>	<b>Conclusion</b>	<b>115</b>
	<b>Bibliography</b>	<b>118</b>



# List of Tables

2.1	Feasibility Test . . . . .	36
2.2	Tube Parameters for First Two Tube Pairs . . . . .	41
3.1	Tube and load parameters for examples. Units for load parameters are normalized with respect to bending stiffness units (force-length <sup>2</sup> ).	74
3.2	Example 4 parameters. Note that $(a_3, b_3)$ vary with translation length of the innermost tube. . . . .	81
3.3	Collision Function . . . . .	84
4.1	Concentric Tube Parameters . . . . .	106
4.2	Average and Maximum Error for Five Sensors . . . . .	111



# List of Figures

1.1	Concentric tube robot consisting of four tubes. . . . .	2
1.2	Fiber Bragg Gratings used as curvature sensors along the length of a continuum robot. . . . .	8
2.1	Effect of torsional twisting when two curved tubes are combined. Tube coordinate frames are denoted by $F_i(s)$ . The relative $z$ -axis twist angle between frames $\alpha(s)$ varies from a maximum $\alpha(0)$ at the base to a minimum $\alpha(L)$ at the tip. The central angles $\beta_i = \theta_{tip,i}$ are proportional to the pre-curvature and to the tube length $L$ . . .	13
2.2	Configurations of stable (left) and unstable (right) tubes slightly varied from straight configurations. Tubes are assumed to have constant pre-curvature. Stable tubes generate consistent direction of relative rotation along arc length while unstable tubes does not. Half of each tube is not visualized to see the inner rotation. . . . .	20
2.3	base versus tip rotation with and without collar. . . . .	21
2.4	Tube with partially constant pre-curvature only at tip. . . . .	24
2.5	$\alpha_0$ versus $\alpha_L$ curves for various $(a, b)$ pairs. . . . .	27

2.6	Numerically computed optimal Pre-curvature. . . . .	31
2.7	Combined curvature of numerical solution with varying base rotation. . . . .	32
2.8	Base rotation versus tip rotation curves of tube pair with optimal pre-curvature and constant pre-curvature. Both pre-curvatures have equal tip orientation angle. . . . .	33
2.9	Comparison between analytic solution and numerical solution. . . . .	35
2.10	Base rotation is generated by motor system. Tubes are mounted on the system. . . . .	38
2.11	EM trackers attached on tips of inner and outer tubes. . . . .	39
2.12	Two tube pairs used in experiments. The upper one is the constant pre-curvature and the lower one is the optimal pre-curvature. . . . .	40
2.13	Base versus tip rotation of tube pair with constant pre-curvature. . . . .	42
2.14	Base versus tip rotation of tube pair with optimal pre-curvature. . . . .	42
2.15	Spiral trajectory on base versus tip rotations plan for tube pair with constant pre-curvature. . . . .	44
2.16	Spiral trajectory on base versus tip rotations plan for tube pair with optimal pre-curvature. . . . .	45
3.1	Concentric tube robot with $n$ tubes. . . . .	55
3.2	Equivalent tube model. . . . .	58
3.3	Variable curvature tube pair. . . . .	73
3.4	Relative rotation of tubes at their tips versus their bases. Dashed lines in (b) show jumps between branches of stable solutions. . . . .	75
3.5	Comparison of relative rotation plot with stability criterion. . . . .	76
3.6	Elastic tip and distributed forces applied to a variable curvature tube pair. . . . .	78

3.7	Relative rotation plots labeled using stability criterion for Example 2. Points on curve labeled stable (o) and unstable (x) using stability criterion. . . . .	79
3.8	Effect of constant world-frame loads depends on both base tube angles. . . . .	80
3.9	Multi-dimensional s-curve. The red 'x' markers denote unstable configurations, and the blue 'o' markers denote stable configurations. . . . .	82
3.10	Tubes comprising robot of Example 4. . . . .	83
3.11	Initial and goal configurations for stable path planning. . . . .	84
3.12	Configuration space maps showing paths and trees generated by RRT for $\epsilon = \{0, 0.9\}$ . Red and green curves are the final paths before and after smoothing, respectively. Colored volumes represent unstable regions. . . . .	88
3.13	Final smoothed stable paths for $\epsilon = \{0, 0.9\}$ . Numbers indicate sequence of configurations along paths. . . . .	89
4.1	Fiber Bragg Gratings used as curvature sensors along the length of a continuum robot. . . . .	92
4.2	Concentric tube robot consisting of four telescoping sections that can be rotated and translated with respect to each other. . . . .	100
4.3	Three tubes comprising the concentric tube robot design used in the examples. Tubes 1 and 2 form a variable-curvature pair that are rotated with respect to each other to vary their composite curvature. Tube 3 can be arbitrarily rotated and extended and conforms to the curvature of the variable curvature pair when retracted. . . . .	105
4.4	PCA bases versus normalized section parameters . . . . .	108

4.5	Average tip position error over the workspace versus the number of sensors. . . . .	110
4.6	Optimized and uniformly spaced locations for four sensors using PCA model. Sensor at robot tip is not shown. . . . .	110
4.7	Histogram of tip position error for three different reconstruction models . . . . .	111
4.8	Histogram of average backbone centerline error for three different reconstruction models . . . . .	112

# 1

## Introduction

Concentric tube robots are a type of continuum robot that are comprised of nested combinations of pre-curved superelastic tubes [1, 2, 3]. The shape of these robots is determined by the bending and torsional elastic interaction of the tubes. They are lightweight and slender, and can assume complex-shaped curves simply by rotating and translating the concentric tubes relative to each other (see Figure 1.1). Since they can be designed to possess sufficient stiffness to both steer through tissue and manipulate tools in body cavities, they are well suited to minimally invasive surgery [4, 5, 6, 7]. For these reasons, concentric tube robots have been regarded with great promise as a surgical device.

Despite many advantages of the robots, the use of the robots in surgical applications is currently very limited because of a couple of practical issues. For instance, the concentric tube robot shows a unique and dangerous behavior at certain configurations with high elastic potential energy. At these high-energy configurations, the torsional elastic energy can be suddenly released through rapid untwisting of one or more tubes [1, 2]. This motion is very dangerous and can

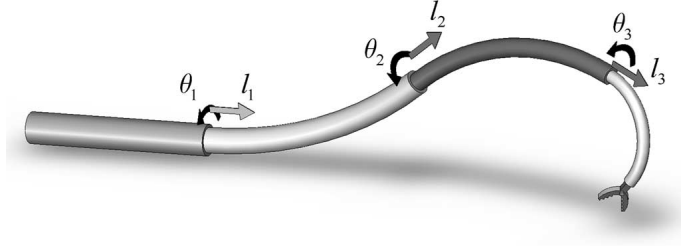


Figure 1.1: Concentric tube robot consisting of four tubes.

damage surrounding tissues or organs when it happens during a surgery. Several approaches have been taken to address this problem. For example, robot design can be constrained to be globally stable, i.e., not exhibit an instability anywhere in their workspace [1, 2]. Assuming each tube is uniformly pre-curved, i.e., tubes with constant pre-curvature are used, a global stability condition for the robot with only two tube is presented as a design constraint in those papers. When arbitrary number and shape of tubes are used, alternately, a stable path planning approach is presented in [8] to avoid passing through unstable configurations. However, the stability condition in [1, 2] does not take account of non-constant pre-curvatures, and they do not consider any external loads in their stability analyses. In fact, a tube pair stably designed based on [1, 2] can be unstable and show the rapid untwisting motion if certain destabilizing external loads are applied. The stable motion planning approach in [8] also assumes no external load, and the presented condition for predicting unstable configurations is somewhat ad hoc and not mathematically rigorous.

Another issue is the computational heaviness and the accuracy of the theoretical kinematics of the concentric tube robot. The kinematics of the concentric tube robot involves solving a set of differential equations with split boundary conditions. Solving this boundary value problem (BVP) requires very heavy computation, and

is hard to solve real-time. Moreover, the shape computed by the theoretical kinematics may not be accurate since it does not take account of some minor tube interactions or material properties, such as frictions, clearances between tubes, and large tube deformations out of linear strain-stress region. Though it is a natural way in many engineering problems to simplify the model and predict the behavior of the system based on the simplified model, a small discordance between the kinematics and the real robot could be sensitive as a surgical robot especially when predicting the rapid untwisting motion.

To address those issues and limitations, this thesis presents the following three researches:

- i) Optimizing pre-curvature of the dominant tube pair to enhance the elastic stability and to design a globally stable tube pair.
- ii) Deriving local stability condition to determine whether given configuration of concentric tube robot is stable or not. The condition can be used in real-time control, motion planning, on-line safety checking or design optimization.
- iii) Fast and accurate shape sensing method for continuum robots using optical fibers with fiber Bragg gratings (FBGs).

The first and the second researches are presented to address the elastic instability, and the third research is presented as a solution of the heavy computation and the inaccuracy of the robot kinematics. Each research includes several numerical and/or hardware experiments to verify the mathematical results.

## 1.1 Contributions of This Thesis

### 1.1.1 Achieving Elastic Stability Through Precurvature Optimization

Minimally invasive surgery can involve navigating inside small cavities or reaching around sensitive tissues. Robotic instruments based on concentric tube technology are well suited to these tasks since they are slender and can be designed to take on shapes of high and varying curvature along their length. One limitation of these robots, however, is that elastic instabilities can arise when rotating one pre-curved tube inside another. This instability has been a constraint in designing pre-curvature of concentric-tube robot. For example, two tubes of equal pre-curvature and Poisson's ratio  $\nu = 0.3$ , are reported to be globally stable for maximum tip orientation angles that are less than  $79^\circ$ . Two possible approaches to enhancing stability are (i) to vary the tube properties so as to modify Poisson's ratio, or (ii) to consider pre-curvatures that vary with the arc length. This work takes the latter approach and its contribution is to prove that, by employing tubes with pre-curvatures that vary with arc length, stability constraints on tube length and tip orientation angle can be eliminated. While prior work has considered tubes of constant or piecewise constant pre-curvature, this work proposes varying tube pre-curvature as a function of arc length as a means to enhance stability. The contributions of this work are summarized as follows:

- stability conditions for a planar tube pair are derived and used to define an optimal design problem,
- this framework enables solving for pre-curvature functions that achieve a desired tip orientation range while maximizing stability and respecting bending strain limits.

### **Elastic Stability of Concentric Tube Robots Subject to External Loads**

The first research presents a way to design a tube pair which is globally stable for any configuration. When it comes to three or more tubes, however, it is very hard to design a tube set that guarantees the elastic stability for any configuration. Even for the tube pair case, moreover, it is still very difficult to take account of external loads in the tube pair design problem. In most cases, unfortunately, the robot has more than two tubes to get enough manipulability, and there could be many types of external loads by the interaction with the environment of the operating space. These facts lead us to use an unstable concentric-tube robot in real world. It is thus very important to make sure that the operating motion or desired configuration is stable.

In the absence of any external load, the elastic stability of given configuration of concentric-tube robot can be measured by checking whether the second variation of the elastic potential energy stored in the tubes are positive definite, i.e., positive for any non-zero variation of the robot configuration:

$$\delta^2 J > 0 \tag{1.1.1}$$

where  $J$  is the potential energy stored in the tubes. This condition is also available in the presence of conservative external loads. When it comes to non-conservative external loads, however, the condition is no longer available since the potential energy  $J$  is defined with the non-conservative loads. Fortunately, the condition (1.1.1) can be generalized through an intuitive physical interpretation. It can be easily shown that the condition (1.1.1) reduces to a condition for the Jacobian matrix of the tube kinematics. Since the Jacobian matrix is also available even in the presence of non-conservative external loads, a general local stability condition can be also derived regardless of whether the external loads are conservative or

not. The contributions of this work are summarized as follows:

- an energy-based local stability condition is derived in the presence of conservative external loads only,
- a Jacobian matrix-based local stability condition is derived for the non-conservative external loads.

### **1.1.2 Optimizing Curvature Sensor Placement for Fast, Accurate Shape Sensing of Continuum Robots**

As opposed to rigid body robots whose shapes are represented by finite dimensional joint variables, the shape representation of a continuum robot consists of infinite dimensional shape variables such as curvatures or centerline position along the arc length of the robot. When a continuum robot has its own mechanics, those shape variables can be computed through a mechanics-based kinematics based on finite number of control variables. In other words, the mechanics-based kinematics expands the finite control variables to infinite dimensional shape variables that are given as functions of arc length. This procedure generally involves solving differential equations over the arc length interval, where the control variables are used in the differential equations or in the boundary conditions. Depending on the complexity of the kinematics or the choice of the precision in solving the differential equations, the shape computation of the continuum robot may not be real-time solvable. In the case of concentric tube robot, for instance, the kinematics of the robot consists of multi-dimensional nonlinear differential equations with boundary conditions given separately at both of the proximal and distal ends. When the robot are subject to external loads, moreover, the complexity of the kinematics equations increases, and it becomes more difficult to compute the shape of the

robot real-time.

Leaving the computational heaviness aside, the mechanics-based kinematics could be inaccurate because of model simplifications. When it comes to a rigid body robot, the rigidness assumption for the comprising links is quite reasonable, and the resulting kinematics is quite accurate. On the contrary to this, the mechanics of a continuum robot is relatively complex, and the mechanics-based kinematics is usually derived under many simplifying assumptions. For example, the kinematics of the concentric tube robot ignores frictions between tubes, and nonlinearity in the compliance of the material. As a result, the kinematics of a continuum robot may not be as much accurate as those of rigid body robots.

If computing the kinematics of continuum robots is heavy and inaccurate, one can alternately consider measuring the shape, not computing it. In this point of view, this research proposes a shape sensing approach using optical fibers with fiber Bragg gratings (FBGs) as local shape sensors. As shown in Figure 1.2, FBG sensors measure local curvatures of a curve at finite number of points.

The contributions of this work are as follows:

- as the procedure of the shape computation based on the sensor measurements, a shape reconstruction algorithm associated with various basis functions is presented,
- and an optimization technique to determine where to place the sensors is proposed.

## 1.2 Organization

This thesis is organized as follows.

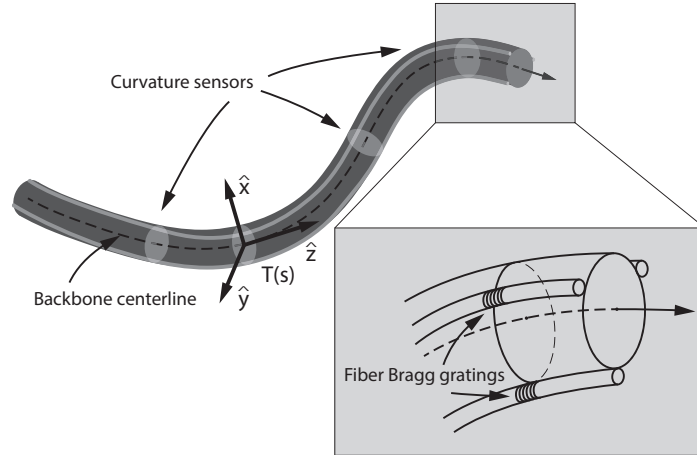


Figure 1.2: Fiber Bragg Gratings used as curvature sensors along the length of a continuum robot.

Chapter 2 proposes a way to achieve elastic stability through pre-curvature optimization. It provides a concise statement of the mechanics-based model for the tubes. And subsequently it presents a necessary and sufficient condition for evaluating the stability of a tube pair with non-constant pre-curvatures based on solving a linear ODE with specified boundary conditions. The approach is demonstrated analytically for two example pre-curvature functions. Then it is followed by formulations of the pre-curvatures optimization as an optimal design problem. Both analytical and numerical examples are provided, and several hardware experiments are provided at the end of the chapter.

In Chapter 3, after deriving the energy-based kinematics of concentric-tube robot in the presence of conservative external loads, a variational approach for deriving the local stability condition is presented subsequently. Then the generalization of the condition to the presence of non-conservative external loads are

derived based on the Jacobian matrix-based physical interpretation of the condition for conservative loads. To validate and demonstrate the new conditions, we presents numerical experiments including several examples with different types of external loads.

Chapter 4 presents a procedure for shape computation of continuum robots using finite number of local curvature measurements by FBG sensors. This procedure is called “reconstruction” since it involves reconstructing the curvature function over the entire length of robot based on the finite number of local curvatures measurements. The presented reconstruction method is associated with choosing basis functions. Several choices of the basis function are also given in this chapter. Finally, in order to increase the reconstruction accuracy with a limited number of sensors, an optimization technique to determine the sensor placements is proposed.

In Chapter 5 conclusion of this thesis is provided as a summary and an evaluation of the results over the thesis. This chapter is comprised of separated conclusions for each of Chapter 2,3 and 4.



# 2

## Achieving Elastic Stability Through Precurvature Optimization

### 2.1 Introduction

A well-known limitation of concentric tube robots is that instabilities can arise in which torsional elastic energy is suddenly released through rapid untwisting of one or more tubes [1, 2]. Several approaches have been taken to address this issue. For example, robots designs can be constrained to be globally stable, i.e., not exhibit an instability anywhere in their workspace. Alternately, path planning can be used to avoid passing through unstable configurations[8].

Nevertheless, elastic instability imposes significant constraints on robot and workspace design. An important example, shown in Figure 2.1, is comprised of a pair of tubes of equal stiffness and with pre-curvatures that are independent of arc length. By rotating these tubes at their base, the combined curvature varies from the maximum pre-curvature value to zero. The latter configuration corresponds to

a base rotation angle of  $\pi$  and is stable, for constant tube pre-curvatures, if and only if the following condition first derived in [9], [1] is met.

$$L\sqrt{(1+\nu)}\|\hat{u}_1\|\|\hat{u}_2\| = \sqrt{\beta_1\beta_2(1+\nu)} < \pi/2 \quad (2.1.1)$$

In this equation,  $L$  is the tube length,  $\nu$  is the Poisson's ratio of the tubes, and  $\hat{u}_i$  and  $\beta_i$  are the pre-curvature and central angle of the  $i$ -th tube, respectively. When this condition is not met, base rotations produce a snapping rotational motion as the tube pair is straightened.

Viewed from different design perspectives, this stability condition places bounds on either the tube length  $L$ , the pre-curvatures,  $\hat{u}_i$ , or the central angles,  $\beta_i$ . In particular, two tubes of equal pre-curvature and Poisson's ratio  $\nu = 0.3$ , are globally stable for maximum tip orientation angles,  $\beta_1 = \beta_2$ , that are less than  $79^\circ$ . There are many clinical applications, however, for which it is desirable for tip orientations to vary smoothly between  $\pm 90^\circ$  or even a wider range. Consequently, the development of techniques to increase the stability of concentric tube robots is important to expanding their clinical utility.

Based on (2.1.1), two possible approaches to enhancing stability are (i) to vary the tube properties so as to modify Poisson's ratio, or (ii) to consider pre-curvatures that vary with the arc length. This paper takes the latter approach and its contribution is to prove that, by employing tubes with pre-curvatures that vary with arc length, stability constraints on tube length,  $L$ , and tip orientation angle,  $\beta$ , can be eliminated. Furthermore, maximum curvature is bounded only by mechanical properties.

The remainder of the paper is organized as follows. The next section provides a concise statement of the mechanics-based model for the tubes. The subsequent section presents a necessary and sufficient condition for evaluating the stability of

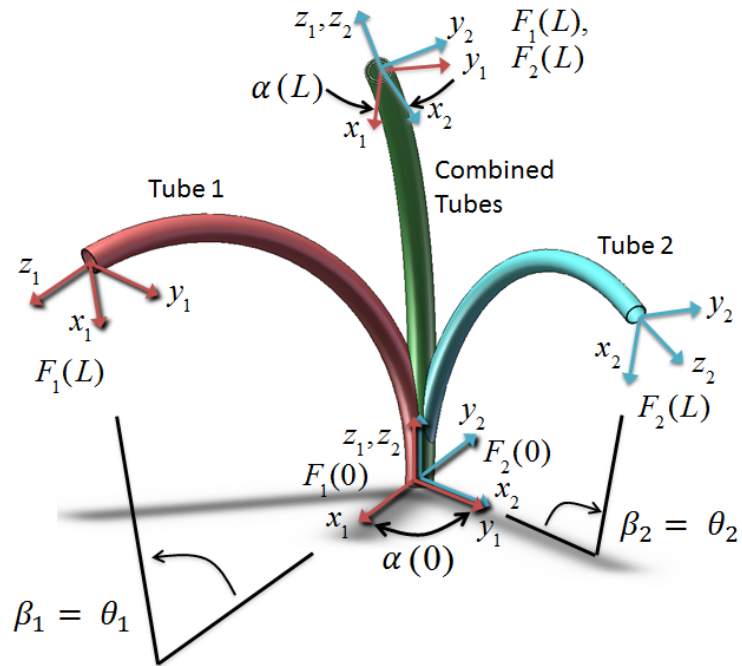


Figure 2.1: Effect of torsional twisting when two curved tubes are combined. Tube coordinate frames are denoted by  $F_i(s)$ . The relative  $z$ -axis twist angle between frames  $\alpha(s)$  varies from a maximum  $\alpha(0)$  at the base to a minimum  $\alpha(L)$  at the tip. The central angles  $\beta_i = \theta_{tip,i}$  are proportional to the pre-curvature and to the tube length  $L$ .

a tube pair with non-constant pre-curvatures based on solving a linear ODE with specified boundary conditions. The approach is demonstrated analytically for two example pre-curvature functions. The subsequent section formulates the selection of pre-curvatures as an optimal design problem and provides both analytical and numerical examples. Conclusions are presented in the final section.

## 2.2 Kinematics of General Concentric-Tube Robot

Consider a concentric-tube robot with  $n$ -tubes. For each tube, material coordinate frame for each cross section is defined by aligning  $z$ -axis tangent to tube's centerline. Each tube is assumed to have varying stiffness  $K_j(s) \in \mathbb{R}^{3 \times 3}$  and pre-curvature  $\hat{u}_j(s) \in \mathbb{R}^3$  along arc-length  $s \in [0, L_j]$ , of which the  $z$ -components  $k_{jz}(s) \in \mathbb{R}$  and  $\hat{u}_{jz}(s) \in \mathbb{R}$  are differentiable. Assume that there is no external loading applied on the tubes. Then the net moment on every cross section equals to zero. This is given by

$$\sum_{j=1}^n R_z(\alpha_j) m_j = 0 \quad (2.2.2)$$

$$m_j = K_j(u_j - \hat{u}_j) \in \mathbb{R}^3. \quad (2.2.3)$$

where  $m_j$  is the moment applied on  $j$ -th tube expressed in its own material coordinate frame.  $R_z(\alpha)$  is a  $3 \times 3$  rotation matrix of the form

$$R_z(\alpha) = \begin{bmatrix} \cos \alpha & -\sin \alpha & 0 \\ \sin \alpha & \cos \alpha & 0 \\ 0 & 0 & 1 \end{bmatrix}$$

and  $\alpha_j$  is relative rotation angle between the material coordinate frame of the first tube and the frame of  $j$ -th tube, i.e.,

$$\dot{\alpha}_j(s) = u_{jz} - u_{1z} \quad (2.2.4)$$

where  $u_j$  is three-component of curvature vector of  $j$ -th tube expressed in tube's material coordinate frame. Note that  $x$  and  $y$  component of  $u_j$  satisfy following frame alignment equation

$$u_j = R_z(\alpha_i)R_z^T(\alpha_j)u_i.$$

Focusing on the  $x$  and  $y$  components of the net moment, Equation (2.2.2) and (2.2.3) is combined to

$$\sum_j R_z(\alpha_j)K_jR_z(\alpha_i)R_z^T(\alpha_j)u_i|_{x,y} = \sum_j R_z(\alpha_j)K_j\hat{u}_j|_{x,y}. \quad (2.2.5)$$

Since the cross section of each tube is circular,  $K_j$  can be defined as following diagonal matrix

$$K_j(s) = \begin{bmatrix} k_{jx}(s) & 0 & 0 \\ 0 & k_{jx}(s) & 0 \\ 0 & 0 & k_{jz}(s) \end{bmatrix}$$

of which the  $x, y$  components are the same. Since the multiplication of  $R_z$  and  $K_j$  is invariant to order, Equation (2.2.5) reduces to

$$u_i|_{x,y} = \left( \sum_j K_j \right)^{-1} R_z^T(\alpha_i) \sum_j R_z(\alpha_j)K_j\hat{u}_j \Big|_{x,y}. \quad (2.2.6)$$

Now an ODE for  $z$ -components of  $u_i$  will be derived. From the equilibrium equation of the special Cosserat rod model, the bending moment  $m_i \in \mathbb{R}^3$  and shear force  $n_i \in \mathbb{R}^3$  on the cross section of  $i$ -th tube satisfy

$$\dot{m}_i = -[u_i]m_i - [v_i]n_i \quad (2.2.7)$$

where  $v_i = [0 \ 0 \ 1]^T$ .  $[\cdot]$  denotes skew-symmetric representation

$$[v] = \begin{bmatrix} 0 & -v_3 & v_2 \\ v_3 & 0 & -v_1 \\ -v_2 & v_1 & 0 \end{bmatrix}. \quad (2.2.8)$$

Substituting (2.2.3) into (2.2.7) results in

$$K_i(\dot{u}_i - \dot{\hat{u}})_i + \dot{K}_i(u_i - \hat{u}_i) = -[u_i]K_i(u_i - \hat{u}_i) - [v_i]n_i. \quad (2.2.9)$$

The  $z$ -component of Equation (2.2.9) provides an ODE for  $u_{iz}$  given by

$$\dot{u}_{iz} = \dot{\hat{u}}_{iz} + \frac{k_{ix}}{k_{iz}}(u_{ix}\hat{u}_{iy} - u_{iy}\hat{u}_{ix}) + \frac{\dot{k}_{iz}}{k_{iz}}(\hat{u}_{iz} - u_{iz}). \quad (2.2.10)$$

Equation (2.2.4), (2.2.6) and (2.2.10) give us the kinematic model of general concentric-tube robot. Since no external load is applied, the torsional bending moments is zero at the tip of each tube. This yields a boundary condition

$$u_{iz}(L_i) = \hat{u}_{iz}(L_i)$$

where  $L_i$  is determined by insertion length of  $i$ -th tube.

## 2.3 Kinematics of Planar Tube Pair

In this section, the kinematic equations are presented for the planar tube pair. Without loss of generality, the planar pre-curvature can be defined as

$$\hat{u}_i = \begin{bmatrix} 0 \\ \hat{u}_{iy}(s) \\ 0 \end{bmatrix}, \quad i = 1, 2.$$

Let us define  $\alpha$  as the relative rotation between the first and the second tubes, i.e.,  $\alpha = \alpha_2$ . For a tube pair with above pre-curvature, the kinematic equations (2.2.6) and (2.2.10) reduce respectively to

$$u_{1x} = -\frac{k_{2x}}{k_{1x} + k_{2x}}\hat{u}_{2y} \sin \alpha \quad (2.3.11)$$

$$\dot{u}_{1z} = \frac{k_{1x}}{k_{1z}}u_{1x}\hat{u}_{1y} - \frac{\dot{k}_{1z}}{k_{1z}}u_{1z}. \quad (2.3.12)$$

Substituting (2.3.11) into (2.3.12) yields

$$\dot{u}_{1z} = -\frac{k_{1x}k_{2x}}{k_{1z}(k_{1x} + k_{2x})}\hat{u}_{1y}\hat{u}_{2y}\sin\alpha - \frac{\dot{k}_{1z}}{k_{1z}}u_{1z}. \quad (2.3.13)$$

By Equation (2.2.4) and  $k_{1z}u_{1z} + k_{2z}u_{2z} = 0$  which is the  $z$ -component of Equation (2.2.2),  $\dot{\alpha}$  is given by

$$\begin{aligned} \dot{\alpha} &= u_{2z} - u_{1z} \\ &= -\frac{k_{1z} + k_{2z}}{k_{2z}}u_{1z} \end{aligned} \quad (2.3.14)$$

and combining (2.3.13) and (2.3.14) yields the following ODE

$$\begin{aligned} \ddot{\alpha} &= \frac{k_{1x}k_{2x}(k_{1z} + k_{2z})}{k_{1z}k_{2z}(k_{1x} + k_{2x})}\hat{u}_{1y}\hat{u}_{2y}\sin\alpha \\ &+ \left( \frac{\dot{k}_{1z} + \dot{k}_{2z}}{k_{1z} + k_{2z}} - \frac{\dot{k}_{1z}}{k_{1z}} - \frac{\dot{k}_{2z}}{k_{2z}} \right) \dot{\alpha} \end{aligned} \quad (2.3.15)$$

with the boundary condition

$$\dot{\alpha}(L) = 0.$$

In practice, Assuming homogeneous material used for tubes, the bending and torsional stiffnesses become constant and Equation (2.3.15) reduces to

$$\ddot{\alpha} = \frac{k_{1x}k_{2x}(k_{1z} + k_{2z})}{k_{1z}k_{2z}(k_{1x} + k_{2x})}\hat{u}_{1y}(s)\hat{u}_{2y}(s)\sin\alpha \quad (2.3.16)$$

with the same boundary condition

$$\dot{\alpha}(L) = 0. \quad (2.3.17)$$

## 2.4 Stability Condition for Planar Tube Pairs

### 2.4.1 Ignoring Straight Transmission Length Inside Collar

Since the differential equation (2.3.16) is second-order, there should be an additional boundary condition besides (2.3.17) in order to obtain a unique solution.

Generally, a base rotation  $\alpha_0$  can be given as the boundary condition. In this case, however, it becomes a two-point boundary value problem for which multiple solutions can exist. On the other hand, if a rotation at the distal end of the robot  $\alpha_L$  is given as the boundary condition, it becomes a backward initial value problem for which a unique solution exists. Let  $\alpha(s, \alpha_L)$  denote the solution to (2.3.16) given the boundary conditions (2.3.17) and

$$\alpha(L) = \alpha_L. \quad (2.4.18)$$

Note that our study is focused on solutions for  $\alpha_L \in [0, \pi]$  rather than  $\alpha_L \in [0, 2\pi]$ . The remaining  $\alpha_L \in [\pi, 2\pi]$  provide symmetric solutions to those for  $\alpha_L \in [0, \pi]$ . As stated in [1], a stable tube pair features a curve in which  $\alpha_0$  increases monotonically with  $\alpha_L$ , or equivalently,

$$\frac{\partial \alpha}{\partial \alpha_L}(0, \alpha_L) > 0 \text{ for } \alpha_L \in [0, \pi]. \quad (2.4.19)$$

A result on the stability of tube pairs can be derived from the following proposition, whose proof can be found in the Appendix 2.7.

**Proposition 2.1.** *Let  $\alpha(s, \alpha_L)$  denotes the solution to (2.3.16)-(2.4.18). If  $\hat{u}_{1y}(s), \hat{u}_{2y}(s) \geq 0$ , the condition*

$$\frac{\partial \alpha}{\partial \alpha_L}(0, \alpha_L) > 0 \text{ for } \alpha_L \in [0, \pi]$$

*is equivalent to*

$$\frac{\partial \alpha}{\partial \alpha_L}(s, \pi) > 0 \text{ for } s \in [0, L]. \quad (2.4.20)$$

Note that the inequalities  $\hat{u}_{1y}(s), \hat{u}_{2y}(s) \geq 0$  are conditions for unloaded shapes of tubes not to ripple. A physical interpretation of this proposition is possible by noting that  $\alpha(s) = \pi$  is the solution to (2.3.16)-(2.4.18) when  $\alpha_L = \pi$ , for which the tube centerlines are straight. Imagine a small configuration change corresponding to a small negative variation of  $\alpha_L$  at this configuration as depicted in Figure 2.2: if the rotational displacement is always negative along the arc length, then from the proposition the tube pair is stable. The same explanation is possible with a positive variation and corresponding positive rotation along the arc length. We just choose the negative sign here in order to bound our scope within  $\alpha_L \in [0, \pi]$ . More precisely, consider the linear differential equation

$$\frac{d^2}{ds^2} \frac{\partial \alpha}{\partial \alpha_L}(s, \pi) = -\frac{k_{1x}k_{2x}(k_{1z} + k_{2z})}{k_{1z}k_{2z}(k_{1x} + k_{2x})} \hat{u}_{1y}(s) \hat{u}_{2y}(s) \frac{\partial \alpha}{\partial \alpha_L}(s, \pi) \quad (2.4.21)$$

with boundary conditions

$$\frac{\partial \alpha}{\partial \alpha_L}(L, \pi) = 1, \quad \frac{d}{ds} \frac{\partial \alpha}{\partial \alpha_L}(L, \pi) = 0. \quad (2.4.22)$$

These equations are obtained by differentiating (2.3.16)-(2.4.18) with respect to  $\alpha_L$  at  $\alpha(s) = \pi$ . If the solution to (2.4.21)-(2.4.22) is always positive over  $s \in [0, L]$ , the tube pair is stable. This allows us to determine the stability of the given tube pair by examining the solution of the linear differential equation for a set of specific boundary conditions, instead of solving (2.3.16) subject to the general boundary conditions (2.3.17) and (2.4.18) for  $\alpha_L \in [0, \pi]$ .

### 2.4.2 Considering Straight Transmission Length Inside Collar

In practice every tube has a finite length of collar in order for the user to hold and rotate the tube. In the case of tube pair, there is an additional elastic part

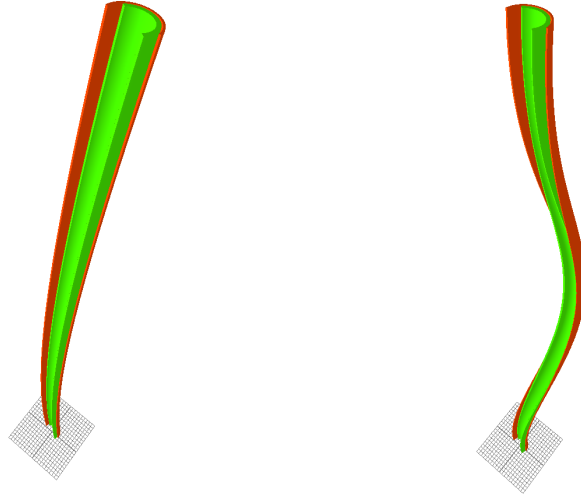


Figure 2.2: Configurations of stable (left) and unstable (right) tubes slightly varied from straight configurations. Tubes are assumed to have constant pre-curvature. Stable tubes generate consistent direction of relative rotation along arc length while unstable tubes does not. Half of each tube is not visualized to see the inner rotation.

of the inner tube inside the collar of the outer tube, that is not taken into account in the stability condition of the previous section. Since the elastic stability of concentric-tube robot is caused by the sudden release of elastic potential energy, the additional potential energy stored in this section has negative effect on the elastic stability. Numerical plots of the base versus tip rotations in the cases with and without considering the collar length are given in Figure 2.3. As shown in this figure, a stable curve can become unstable when the elastic part of the inner tube inside the collar is taken into account. This means that the stability condition (2.4.19) is no longer applicable when the transmission length of the inner

tube inside the collar length is considered.

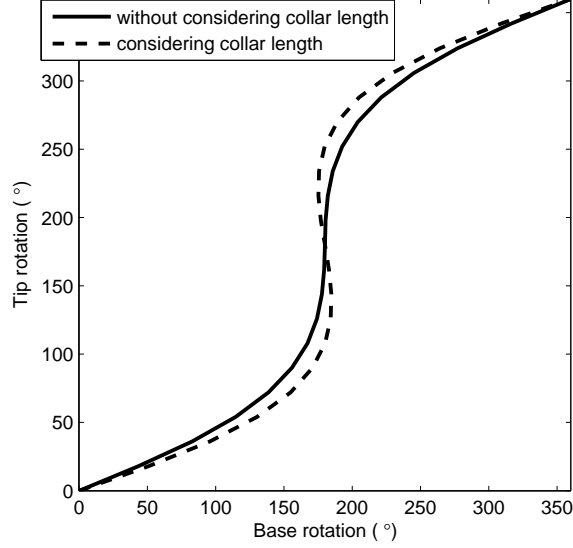


Figure 2.3: base versus tip rotation with and without collar.

Let  $l_c$  denote the collar length of outer tube and  $\alpha(-l_c, \alpha_L)$  denote the actual base rotation given the tip rotation  $\alpha_L$ . Then the following inequality

$$\frac{\partial \alpha}{\partial \alpha_L}(-l_c, \alpha_L) > 0$$

should satisfy for  $\alpha_L \in [0, \pi]$  in order for a tube pair to be stable. Assuming that collar is stiff enough not to twist, it satisfies

$$\alpha(-l_c, \alpha_L) = \alpha(0, \alpha_L) + u_{1z}(0)l_c. \quad (2.4.23)$$

Note that the twist rate of the inner tube inside the collar of the outer tube is the constant value,  $u_{1z}(0)$ , and  $u_{1z}(0)l_c$  is the corresponding twist angle. Substituting

Equation (2.3.14) into (2.4.23) and differentiating it with respect to  $\alpha_L$  yields

$$\frac{\partial \alpha}{\partial \alpha_L}(-l_c, \alpha_L) = \frac{\partial \alpha}{\partial \alpha_L}(0, \alpha_L) - \frac{k_{2z} l_c}{k_{1z} + k_{2z}} \frac{d}{ds} \frac{\partial \alpha}{\partial \alpha_L}(0, \alpha_L). \quad (2.4.24)$$

Since (2.4.24) should be also positive for a stable tube pair, we have an additional condition besides (2.4.19) for  $\frac{\partial \alpha}{\partial \alpha_L}(-l_c, \alpha_L)$  to be positive. By Proposition 2.3 in Appendix and using the fact that  $\frac{d}{ds} \frac{\partial \alpha}{\partial \alpha_L}(0, \alpha_L)$  is obtained by backward integration of Equation (2.4.21) with the initial value in (2.4.22), it is easily shown to satisfy

$$\begin{aligned} \min_{\alpha_L \in [0, \pi]} \frac{\partial \alpha}{\partial \alpha_L}(0, \alpha_L) &= \frac{\partial \alpha}{\partial \alpha_L}(0, \pi) \\ \max_{\alpha_L \in [0, \pi]} \frac{d}{ds} \frac{\partial \alpha}{\partial \alpha_L}(0, \alpha_L) &= \frac{d}{ds} \frac{\partial \alpha}{\partial \alpha_L}(0, \pi). \end{aligned}$$

We can find the additional stability condition by setting the minimum value of Equation (2.4.24) to be positive, which is given by

$$\frac{\partial \alpha}{\partial \alpha_L}(0, \pi) - \frac{k_{2z} l_c}{k_{1z} + k_{2z}} \frac{d}{ds} \frac{\partial \alpha}{\partial \alpha_L}(0, \pi) > 0. \quad (2.4.25)$$

## 2.5 Evaluating Stability for Specific Pre-curvature Functions

To both validate and demonstrate the applicability of our stability results, we now consider three examples in which the pre-curvature is prescribed analytically. In the first example, we show that for the constant pre-curvature case, our stability result reduces to the previously published result given by (2.1.1). The second example considers pre-curvatures of the form  $\hat{u}_y = \frac{b}{s+a}$  with  $\{a, b\} \in \mathbb{R}^+$ .

### 2.5.1 Constant Pre-curvature

If  $\hat{u}_{y1}$  and  $\hat{u}_{y2}$  are a constant function, there exists an analytic solution to (2.4.21) given by

$$\frac{\partial \alpha}{\partial \alpha_L}(s, \pi) = \cos(c_1(L - s))$$

where

$$c_1 = \sqrt{\frac{k_{1x}k_{2x}(k_{1z} + k_{2z})}{k_{1z}k_{2z}(k_{1x} + k_{2x})}} \hat{u}_{1y}\hat{u}_{2y}. \quad (2.5.26)$$

The stability conditions (2.4.20) and (2.4.25) reduce to

$$\begin{aligned} c_1 L &< \frac{\pi}{2} \\ \cos(c_1 L) - c_1 c_2 \sin(c_1 L) &> 0 \end{aligned}$$

where

$$c_2 = \frac{k_{2z} l_c}{k_{1z} + k_{2z}}. \quad (2.5.27)$$

Since  $\cos(c_1 L)$  in the second inequality is positive by the first inequality, they reduce again to

$$c_1 L < \frac{\pi}{2} \quad (2.5.28)$$

$$c_1 L < \tan^{-1} \frac{1}{c_1 c_2}. \quad (2.5.29)$$

Note that (2.5.28) is the same result reported in [1], and (2.5.29) converges to (2.5.28) as  $l_c \rightarrow 0$ , i.e.,  $c_2 \rightarrow 0$ .

### 2.5.2 Partially Constant Pre-curvature

One of the most famous shape of tube for concentric-tube robot is described in Figure 2.4. Each tube in the figure has straight section at the base and curved

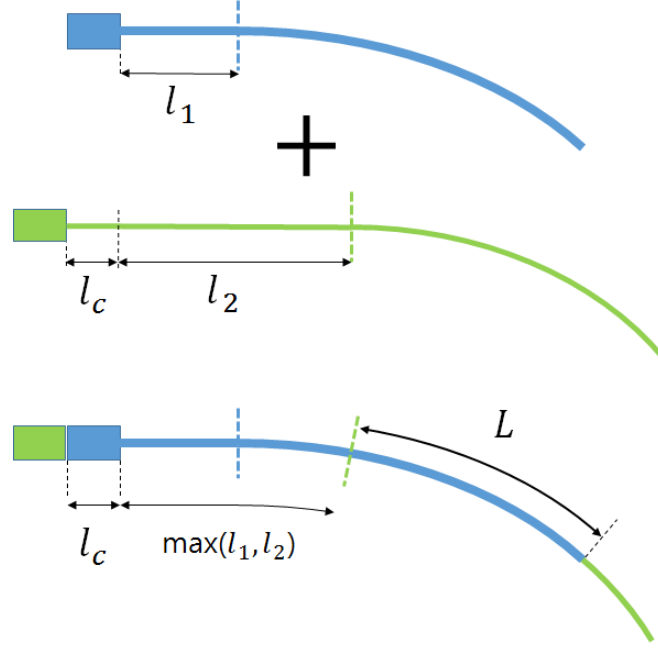


Figure 2.4: Tube with partially constant pre-curvature only at tip.

section at the tip. The pre-curvature functions are given by

$$\hat{u}_{1y}(s) = \begin{cases} 0, & \text{if } s < l_1 \\ \hat{u}_1, & \text{if } s \geq l_1 \end{cases} \quad (2.5.30)$$

$$\hat{u}_{2y}(s) = \begin{cases} 0, & \text{if } s < l_2 \\ \hat{u}_2, & \text{if } s \geq l_2 \end{cases} \quad (2.5.31)$$

where  $l_i$  is the length of straight section of  $i$ -th tube. We remark that  $L$  is not the total insertion length, which is defined in Figure 2.4. Defining  $\bar{l}$  by  $\bar{l} = \max(l_1, l_2)$ , the analytic solution to (2.4.21) is given by

$$\frac{\partial \alpha}{\partial \alpha_L}(s, \pi) = \begin{cases} \cos(c_1 L) + c_1(s - \bar{l}) \sin(c_1 L), & \text{if } s < \bar{l} \\ \cos(c_1(L + \bar{l} - s)), & \text{if } s \geq \bar{l}. \end{cases}$$

with the same  $c_1$  in (2.5.26). Then the stability conditions (2.4.20) and (2.4.25) reduce to

$$c_1 L < \tan^{-1} \frac{1}{c_1 \bar{l}} \quad (2.5.32)$$

$$c_1 L < \tan^{-1} \frac{1}{c_1 (\bar{l} + c_2)} \quad (2.5.33)$$

where  $c_2$  is defined in (2.5.27). Again, (2.5.33) converges to (2.5.32) as  $l_c \rightarrow 0$ . Note that the conditions for the constant pre-curvature are a particular case of these conditions when  $\bar{l} = 0$ .

### 2.5.3 Pre-curvature Function, $\hat{u}_y = \frac{b}{s+a}$

Assume that  $\hat{u}_y(s) = \frac{b}{s+a}$  with positive scalars  $a \in \mathbb{R}^+$  and  $b \in \mathbb{R}^+$ . The analytic solution to (2.4.21) is given by

$$\frac{\partial \alpha}{\partial \alpha_L}(s, \pi) = \begin{cases} -\frac{c_2}{c_1} \left( \frac{s+a}{L+a} \right)^{c_3} + \frac{c_3}{c_1} \left( \frac{s+a}{L+a} \right)^{c_2} & \text{if } c_0 < \frac{1}{4} \\ \sqrt{\frac{s+a}{L+a}} \left( 1 - \frac{1}{2} \ln \frac{s+a}{L+a} \right) & \text{if } c_0 = \frac{1}{4} \\ -\frac{c_0}{c_5} \sqrt{\frac{s+a}{L+a}} \sin \left( c_5 \ln \frac{s+a}{L+a} - c_6 \right) & \text{if } c_0 > \frac{1}{4} \end{cases} \quad (2.5.34)$$

where

$$\begin{aligned} c_0 &= \frac{k_x}{k_z} b^2, \quad c_1 = \sqrt{1 - 4c_0}, \quad c_2 = \frac{1}{2} - \sqrt{\frac{1}{4} - c_0} \\ c_3 &= \frac{1}{2} + \sqrt{\frac{1}{4} - c_0}, \quad c_4 = \sqrt{\frac{1}{4} + c_0}, \quad c_5 = \sqrt{c_0 - \frac{1}{4}} \\ c_6 &= \tan^{-1} 2c_3. \end{aligned}$$

When  $c_0 \leq \frac{1}{4}$ , it is easily shown that  $\frac{\partial \alpha}{\partial \alpha_L}(s, \pi) > 0$  for  $s \in [0, L]$ ; In other words, it can be verified that the tube pair is stable simply by checking  $\frac{\partial \alpha}{\partial \alpha_L}(0, \pi) > 0$  and  $\frac{d}{ds} \frac{\partial \alpha}{\partial \alpha_L}(s, \pi) \geq 0$ . This implies that any pre-curvature with  $(a, b)$  satisfying  $c_0 \leq \frac{1}{4}$  can be used for a stable tube pair. Since  $c_0$  is invariant to  $a$ , the choice of  $a$  is unbounded in  $\mathbb{R}^+$ . Defining the central angle  $\theta_{tip}$  swept out by the initial curvature

of the tubes as

$$\theta_{tip} = \int_0^L \hat{u}_y ds = b \ln \frac{L+a}{a},$$

an arbitrarily large  $\theta_{tip}$  can be achieved by selecting  $a$  to be a very small positive scalar. From a theoretical perspective, this result is quite meaningful, since the swept angle  $\theta_{tip}$  is bounded by the inequality (2.5.28) for the constant precurvature case. A more detailed discussion is presented in Section 2.6.

On the other hand, when  $c_0 > \frac{1}{4}$ , the following inequality must hold in order to satisfy  $\frac{\partial \alpha}{\partial \alpha_L}(s) > 0$ :

$$\sqrt{c_0 - \frac{1}{4}} \ln \frac{s+a}{L+a} - \tan^{-1} 2\sqrt{c_0 - \frac{1}{4}} > -\pi.$$

Noting that the left side attains a minimum at  $s = 0$ , the inequality reduces to

$$\frac{a}{L} > \left( \exp \frac{\pi - \tan^{-1} 2\sqrt{c_0 - \frac{1}{4}}}{\sqrt{c_0 - \frac{1}{4}}} - 1 \right)^{-1}. \quad (2.5.35)$$

In practice it is hard to achieve  $c_0 \leq \frac{1}{4}$  due to the yield strain of the material used for tubes, which is also discussed in more detail in Section 2.6. The inequality (2.5.35) should in practice be regarded as a general stability condition for the pre-curvature  $\hat{u}_y = \frac{b}{s+a}$ .

The stability condition (2.5.35) can be validated by plotting  $\alpha_0$  versus  $\alpha_L$  curves for various  $(a, b)$  pairs. The curves are depicted in Figure 2.5. To plot each curve in the figure,  $\alpha_L$  is discretized into 21 values between 0 and  $2\pi$  and given as boundary conditions for the general kinematic equations (2.2.4), (2.2.6) and (2.2.10). If a pair  $(a, b)$  satisfies the stability condition (2.5.35), the curve is monotonically increasing as expected. Similarly, for a pair  $(a, b)$  on the boundary of the inequality (2.5.35), the curve is still increasing, but possesses an infinitely steep slope at  $(\alpha_0, \alpha_L) = (\pi, \pi)$ . Otherwise, the slope is negative over some parts of the curve.

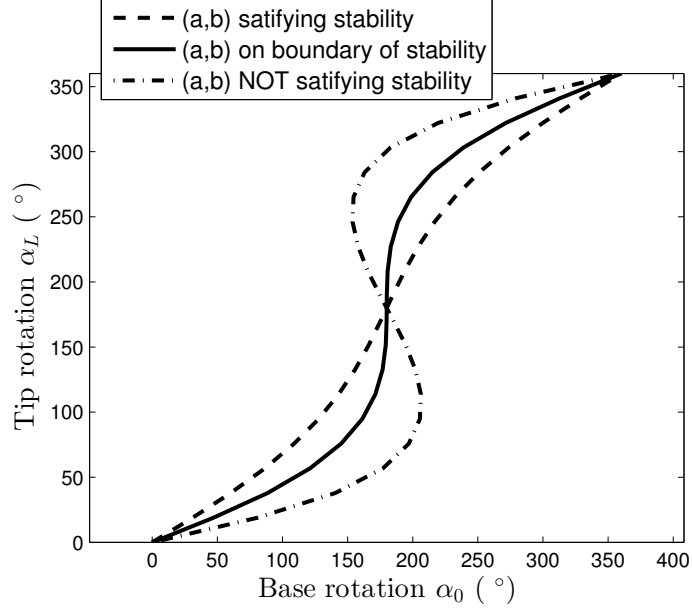


Figure 2.5:  $\alpha_0$  versus  $\alpha_L$  curves for various  $(a, b)$  pairs.

## 2.6 Formulation as an Optimal Design Problem

In this section we formulate the selection of pre-curvatures as an optimal design problem. Since the balanced tube pair is generally comprised of tubes with equal stiffness and pre-curvature, it is assumed in this section that the tubes have the same pre-curvature function  $\hat{u}(s)$  and the same bending and torsional stiffnesses  $k_x$  and  $k_z$ . These assumptions simplify the optimal design problem to be solvable.

First of all, it is necessary to discuss the definition of the optimal design for a tube pair. Given a desired value of  $\theta_{tip}$ , a tube pair is stable if and only if the solution to (2.3.16)-(2.4.18),  $\alpha(s, \alpha_L)$ , satisfies the inequality

$$\frac{\partial \alpha}{\partial \alpha_L}(0, \alpha_L) > 0 \text{ for } \alpha_L \in [0, \pi]. \quad (2.6.36)$$

If there exist multiple pre-curvature function candidates that satisfy (2.6.36), it is desirable to choose the most stable solution. Note that  $\frac{\partial\alpha}{\partial\alpha_L}(0, \alpha_L)$  is the inverse slope of  $\alpha_0$  versus  $\alpha_L$  curve. If this value is excessively small (but still positive) for some value of  $\alpha_L \in [0, \pi]$ , even a small base rotation can cause the tube pair to snap very quickly. An optimal pre-curvature can therefore be defined as one that maximizes the minimum value of  $\frac{\partial\alpha}{\partial\alpha_L}(0, \alpha_L)$  over  $\alpha_L \in [0, \pi]$ . The resulting optimal design problem is formulated as follows.

$$\max_{\hat{u}_y(s)} \left( \min_{\alpha_L} \frac{\partial\alpha}{\partial\alpha_L}(0, \alpha_L) \right)$$

subject to the constraints

$$\begin{aligned} \int_0^L \hat{u}_y(s) ds &= \theta_{tip} \\ \frac{\partial\alpha}{\partial\alpha_L}(0, \alpha_L) &> 0. \end{aligned}$$

If  $\frac{\partial\alpha}{\partial\alpha_L}(0, \alpha_L) > 0$ , then it satisfies

$$\min_{\alpha_L} \frac{\partial\alpha}{\partial\alpha_L}(s, \alpha_L) = \frac{\partial\alpha}{\partial\alpha_L}(s, \pi) \quad (2.6.37)$$

for any  $s \in [0, L]$ ; this is proven in Proposition 2.3, which is used in the proof of Proposition 2.1 given in the appendix. Using (2.6.37) and Proposition 2.1 to respectively reformulate the cost function and the last constraint, the optimization reduces equivalently to

$$\max_{\hat{u}_y(s)} \frac{\partial\alpha}{\partial\alpha_L}(0, \pi) \quad (2.6.38)$$

subject to the modified constraints

$$\begin{aligned} \int_0^L \hat{u}_y(s) ds &= \theta_{tip} \\ \frac{\partial\alpha}{\partial\alpha_L}(s, \pi) &> 0. \end{aligned}$$

In practice, a high pre-curvature causes yielding problems, especially when the tubes are straightened. One possible pre-curvature function that does not cause yielding is given by

$$\hat{u}_y(s) < \frac{2\bar{\epsilon}}{d(\bar{\epsilon} + 1)}$$

where  $\bar{\epsilon}$  and  $d$  are the yield strain and outer diameter of the tube, respectively.

To include this feature in the optimization, one can add the constraint

$$\hat{u}_y(s) \leq \hat{u}_{max} \quad (2.6.39)$$

to the optimization, with  $\hat{u}_{max}$  chosen to satisfy  $\hat{u}_{max} < \frac{2\bar{\epsilon}}{d(\bar{\epsilon}+1)}$ .

### 2.6.1 Numerical Solution of the Optimal Design Problem

As an alternative to specifying a pre-curvature function a priori, numerical techniques can be used to generate solutions. A simple way to solve the problem defined above is to recast it in the form of an optimal control problem and to employ, e.g., the steepest descent method described in [10].

For notational simplicity, we define

$$x_1(s) = \frac{\partial \alpha}{\partial \alpha_L}(s, \pi), \quad x_2(s) = \frac{d}{ds} \frac{\partial \alpha}{\partial \alpha_L}(s, \pi).$$

Equation (2.4.21) and the boundary conditions (2.4.22) can then be written

$$\begin{pmatrix} \dot{x}_1(s) \\ \dot{x}_2(s) \end{pmatrix} = \begin{pmatrix} x_2(s) \\ -\frac{k_x}{k_z} \hat{u}_y^2(s) x_1(s) \end{pmatrix}, \quad x(L) = \begin{pmatrix} 1 \\ 0 \end{pmatrix}. \quad (2.6.40)$$

The cost function to be minimized is given by

$$J = -\frac{\partial \alpha}{\partial \alpha_L}(0, \pi) = \int_0^L x_2(s) ds - 1.$$

Ignoring the constant term  $-1$ , the Hamiltonian and costate equation are respectively given by

$$\begin{aligned} \mathcal{H} &= x_2(s) + p_1(s)x_2(s) - \frac{k_x}{k_z}\hat{u}_y^2(s)p_2(s)x_1(s) \\ \begin{pmatrix} \dot{p}_1(s) \\ \dot{p}_2(s) \end{pmatrix} &= \begin{pmatrix} \frac{k_x}{k_z}\hat{u}_y^2(s)p_2(s) \\ -1 - p_1(s) \end{pmatrix}, \quad p(0) = \begin{pmatrix} 0 \\ 0 \end{pmatrix}. \end{aligned} \quad (2.6.41)$$

The update direction  $\frac{dH}{du}$  is given by

$$\frac{d\mathcal{H}}{du} = -2\frac{k_x}{k_z}\hat{u}_y(s)p_2(s)x_1(s). \quad (2.6.42)$$

In the numerical implementation, the constraints  $\hat{u}_y(s) \leq u_{max}$  and  $\int_0^L \hat{u}_y(s)ds = \theta_{tip}$  are given as linear constraints of the form

$$\begin{aligned} \hat{u}_y^i &\leq u_{max}, \quad i = 1, \dots, N \\ \sum_{i=1}^N \hat{u}_y^i \Delta s &= \theta_{tip} \end{aligned}$$

where  $N$  is the dimension of  $\hat{u}_y$  discretized by the step size  $\Delta s$ , and  $\hat{u}_y^i$  is its  $i$ -th component. Then  $\frac{dH}{du}$  is the  $N$ -dimensional gradient vector of the cost  $J$ , which can be computed by solving the initial value problem (2.6.40), (2.6.41) and Equation (2.6.42) sequentially. The results are given in Figure 2.6-2.8.

In Figure 2.6, the numerical solution tends to have higher pre-curvature at the base and lower pre-curvature at the distal end. If the pre-curvature is high at the distal end, both tubes are bound to each other tightly at the distal end, causing a large twist along the arc length as the base rotates. Consequently, this increases the possibility of a rapid untwisting motion by a sudden release of the stored energy.

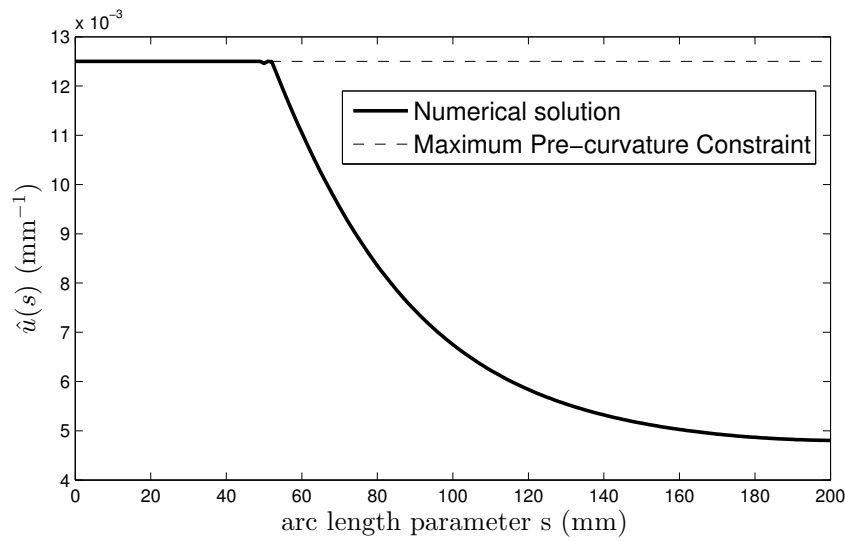


Figure 2.6: Numerically computed optimal Pre-curvature.

### 2.6.2 Analytic Solution of the Optimal Design Problem

Though the numerical method presented in the previous section is derived by optimizing the continuous pre-curvature function  $\hat{u}(s)$  based on the optimal control theory, the numerical implementation of the algorithm is just a high dimensional vector space optimization. If the pre-curvature function is discretized into  $N$  values, for example, the problem is  $N$ -dimensional vector space optimization with  $N$  number of inequality constraints and a equality constraint. It is well-known that the performance of vector space optimization drops near the boundary of multiple inequality constraints. In our problem we have observed some numerical convergence issues such as slow and shaking convergence. To address these problems, the analytic equation of the solution to the optimal design problem is derived in this section.

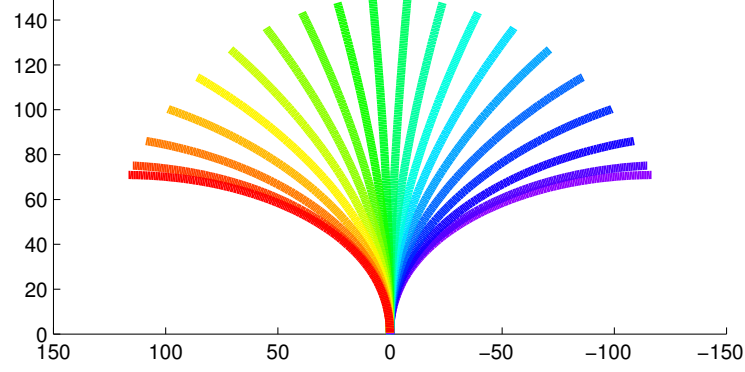


Figure 2.7: Combined curvature of numerical solution with varying base rotation.

First, let us introduce a Lagrangian function

$$\begin{aligned}
 \mathcal{L} &= \mathcal{H} + \lambda(s)(\hat{u}_y(s) - u_{max}) + \mu\hat{u}_y(s) \\
 &= x_2(s) + p_1(s)x_2(s) - \frac{k_x}{k_z}\hat{u}_y^2(s)p_2(s)x_1(s) \\
 &\quad + \lambda(s)(\hat{u}_y(s) - u_{max}) + \mu\hat{u}_y(s)
 \end{aligned}$$

where  $\mu \in \mathbb{R}$  is Lagrangian multiplier of the equality constraint  $\int_0^L \hat{u}_y(s)ds = \theta_{tip}$  and  $\lambda(s)$  is Lagrangian multiplier function of the inequality constraint  $\hat{u}_y(s) \leq \hat{u}_{max}$  that satisfies  $\lambda(s) \geq 0$  and  $\lambda(s)(\hat{u}_y(s) - u_{max}) = 0$ . The necessary conditions for optimal control is given by

$$\begin{aligned}
 \dot{x} &= \frac{d\mathcal{L}}{dp}, \quad x(L) = \begin{pmatrix} 1 \\ 0 \end{pmatrix} \\
 \dot{p} &= -\frac{d\mathcal{L}}{dx}, \quad p(0) = \begin{pmatrix} 0 \\ 0 \end{pmatrix} \\
 \frac{d\mathcal{L}}{du} &= 0.
 \end{aligned}$$

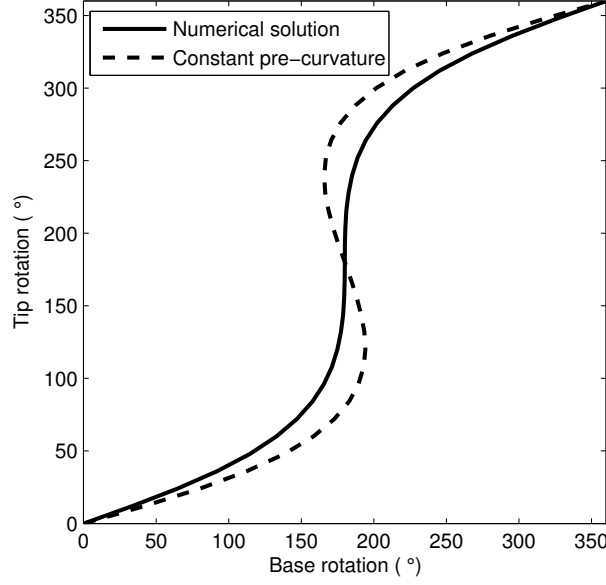


Figure 2.8: Base rotation versus tip rotation curves of tube pair with optimal pre-curvature and constant pre-curvature. Both pre-curvatures have equal tip orientation angle.

The problem is summarized as follows

$$\begin{aligned} \begin{pmatrix} \dot{x}_1(s) \\ \dot{x}_2(s) \end{pmatrix} &= \begin{pmatrix} x_2(s) \\ -\frac{k_x}{k_z} \hat{u}_y^2(s) x_1(s) \end{pmatrix}, \quad x(L) = \begin{pmatrix} 1 \\ 0 \end{pmatrix} \\ \begin{pmatrix} \dot{p}_1(s) \\ \dot{p}_2(s) \end{pmatrix} &= \begin{pmatrix} \frac{k_x}{k_z} \hat{u}_y^2(s) p_2(s) \\ -1 - p_1(s) \end{pmatrix}, \quad p(0) = \begin{pmatrix} 0 \\ 0 \end{pmatrix} \\ &-2\frac{k_x}{k_z} \hat{u}_y(s) p_2(s) x_1(s) + \lambda(s) + \mu = 0 \\ \lambda(s)(\hat{u}_y(s) - u_{max}) &= 0, \quad \lambda(s) \geq 0, \quad \hat{u}_y(s) - u_{max} \leq 0 \\ &\int_0^L \hat{u}_y(s) ds = \theta_{tip} \end{aligned}$$

where  $x_1(s), x_2(s), p_1(s), p_2(s), \hat{u}(s)_y, \lambda(s)$  and  $\mu$  are unknowns. Since these are the necessary conditions, they may have multiple solutions including every local minimizer and maximizer. From many times of observations of the numerical solutions, we have assumed that the solution has a single saturation point of which the left side attains the upper bound and the right side decreases gradually as depicted in Figure 2.6. Under this assumption, the solution is given by

$$\hat{u}_y(s) = \begin{cases} u_{max} & \text{if } s < l \\ \frac{a}{f(s)} & \text{if } s \geq l \end{cases} \quad (2.6.43)$$

where

$$\begin{aligned} t &= \tan \sqrt{\frac{k_x}{k_z}} u_{max} l \\ a &= \frac{\sqrt{\frac{k_x}{k_z}} t}{l - L - \frac{1}{\sqrt{\frac{k_x}{k_z}} u_{max}} t} \\ b &= \frac{L - l + (l + L)t^2 + \frac{1}{\sqrt{\frac{k_x}{k_z}} u_{max}} t}{2t^2} \\ c_2 &= a^2(L - b)^2 \\ f(s) &= c_2 + \frac{k_x}{k_z} - a^2(s - b)^2 \\ \theta_{tip} &= \frac{\tanh^{-1} \frac{a(L-b)}{\sqrt{c_2 + \frac{k_x}{k_z}}}}{\sqrt{c_2 + \frac{k_x}{k_z}}} - \frac{\tanh^{-1} \frac{a(l-b)}{\sqrt{c_2 + \frac{k_x}{k_z}}}}{\sqrt{c_2 + \frac{k_x}{k_z}}} + u_{max} l. \end{aligned} \quad (2.6.44)$$

The saturation point  $l$  should be computed by a root finding of Equation (2.6.44) for the given tip orientation angle  $\theta_{tip}$ . The comparison between the analytic solution and the numerical solution is given in Figure 2.9. The figure shows just a typical case. The quality of the numerical solution depends on the optimal design parameters such as the tip orientation angle  $\theta_{tip}$  or the maximum pre-curvature  $u_{max}$ .

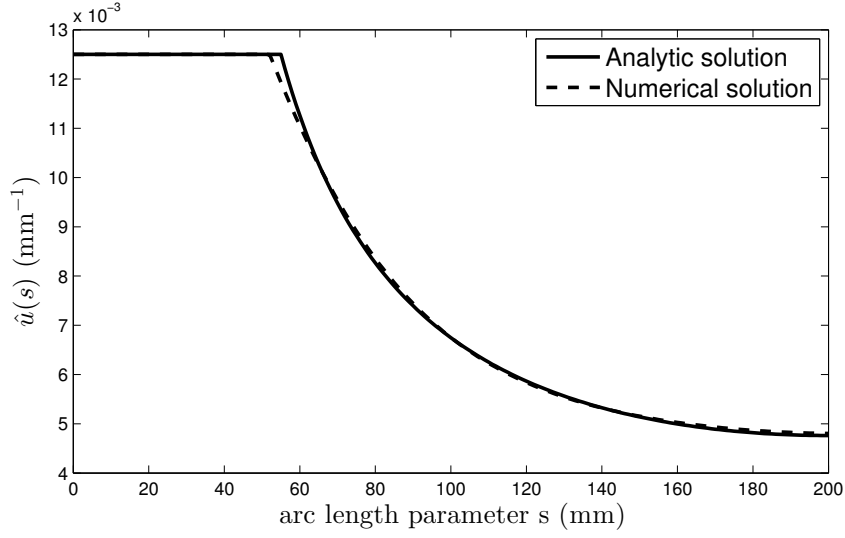


Figure 2.9: Comparison between analytic solution and numerical solution.

Though the quality of the numerical solution is not significantly different from the analytic solution in many cases, there is a remarkable advantage of the analytic solution in providing a feasibility condition of the optimal design problem. If the given tip orientation angle is too large, the solution  $\hat{u}(s)$  does not satisfy the stability conditions (2.4.20) and (2.4.25). Substituting the analytic equation of  $x_1(x)$

$$x_1(s) = \begin{cases} x_1(l) \cos \sqrt{\frac{k_x}{k_z}} u_{max}(s-l) \\ + \dot{x}_1(l) \sin \sqrt{\frac{k_x}{k_z}} u_{max}(s-l) & \text{if } s < l \\ c_1 \sqrt{f(s)} \exp \left( -\sqrt{\frac{c_2}{c_2 + \frac{k_x}{k_z}}} \tanh^{-1} \frac{a(s-b)}{\sqrt{c_2 + \frac{k_x}{k_z}}} \right) & \text{if } s \geq l \end{cases} \quad (2.6.45)$$

into the conditions (2.4.20), (2.4.25) yields the following feasibility conditions

$$0 < l < \frac{\pi}{2\sqrt{\frac{k_x}{k_z}} u_{max}} \quad (2.6.46)$$

$$t^2 + \frac{t}{\sqrt{\frac{k_x}{k_z}} u_{max}(l-L)} - 1 < 0. \quad (2.6.47)$$

These inequalities are used to compute the exact upper bound of the tip orientation angle in the next section. Note that  $x_1(l)$ ,  $\dot{x}_1(l)$  and  $c_1$  are given by straightforward calculations from the boundary conditions  $x_1(l^+) = x_1(l^-)$ ,  $\dot{x}_1(l^+) = \dot{x}_1(l^-)$  and  $x_1(L) = 1$ . The specific equations are not presented since the inequalities (2.6.46) and (2.6.47) are invariant to these values.

### 2.6.3 Feasibility of Optimal Design Problem

This section presents an algorithmic representation of feasibility test to determine if the given problem has a feasible solution, i.e., a stable pre-curvature function. When a desired tip orientation angle is too large, it is impossible to get a pre-curvature function for a tube pair to be stable. Let  $\Theta_{tip}$  denote the exact upper bound of the tip orientation angle. Then  $\Theta_{tip}$  is computed and compared to the desired tip orientation angle in Table 2.1.

Table 2.1: Feasibility Test

---

<b>FEASIBILITY_TEST</b> ( $L, u_{max}, \theta_{tip}$ )
<b>1</b> Perform a root finding in the interval (2.6.46) to find $l$ on the boundary of inequality (2.6.47) for given $L$ and $u_{max}$ .
<b>2</b> Compute $\Theta_{tip}$ by substituting $l$ from <b>1</b> into Equation (2.6.44).
<b>3</b> If $\theta_{tip} < \Theta_{tip}$ ,
return <b>true</b>
Else,
return <b>false</b>

---

Note that **1** in Table 2.1 always guarantees a unique solution since the left side of (2.6.47) is monotonically increasing from  $-1$  to  $\infty$  in the interval (2.6.46).

If the problem is feasible, the optimal pre-curvature is then obtained by Equation (2.6.43). If the problem is not feasible, on the other hand, there does not exist any pre-curvature function for a tube pair to be stable with given  $(L, u_{max}, \theta_{tip})$ . In this case one should increase the tube length  $L$  or the maximum pre-curvature  $u_{max}$ , or decrease the desired tip orientation angle  $\theta_{tip}$  in order to make the problem feasible.

## 2.7 Hardware Experiments

To validate the theoretical results in the previous sections, a set of hardware experiments have been performed in this section. The experiments compare the elastic stabilities of i) a tube pair with constant pre-curvature and ii) a tube pair with optimal pre-curvature. Both tube pairs are designed to have the same tip orientation angle and tube length for fair comparisons. Our experiments consist of the following steps:

- i) Each tube pair is mounted on the motor system and the base of the outer tube is rotated by controlling the motor. The system is shown in Figure 2.10.
- ii) While the base is rotating, the base rotations and tip movements are being recorded. The base rotation is recorded by reading the encoder of the motor, and the tip movement is tracked by the position and orientation reads of two EM trackers independently attached on the tips of inner and outer tubes. Figure 2.11 shows the EM trackers attached on the tips. A sequence of relative orientations between two EM trackers,  $\{R_i\}_{i=1, \dots, m}$ , are recorded for the later computations of the relative tip rotations between the tubes.
- iii) As a post processing, the relative tip rotation angles are computed from the

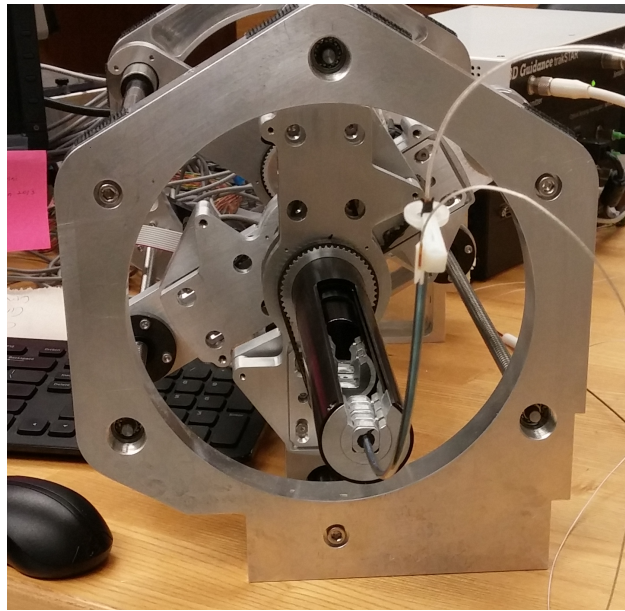


Figure 2.10: Base rotation is generated by motor system. Tubes are mounted on the system.

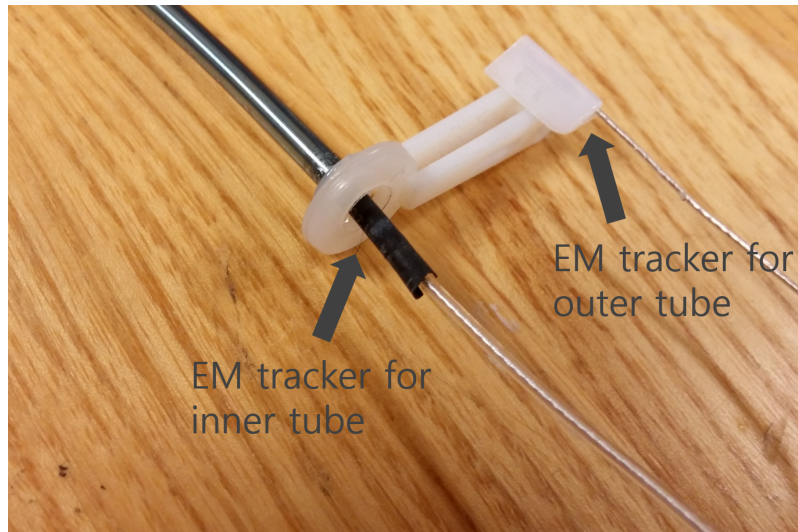


Figure 2.11: EM trackers attached on tips of inner and outer tubes.

EM tracker measurements,  $\{R_i\}_{i=1,\dots,m}$ . The relative movement between two EM trackers is a screw motion, i.e.,

$$R_i = R_0 e^{\hat{w}\alpha_i} \in SO(3)$$

where  $R_0$ ,  $\hat{w}$  and  $\alpha_i$  are the initial relative orientation, the skew axis and the tip rotation angles respectively.  $R_0$ ,  $\hat{w}$  and  $\alpha_i$  are computed by a series of least squares problems, but the detailed formulations are skipped for the concentration to the results.

The tube pairs used in the experiments are shown in Figure 2.12. The specific tube parameters are given in Table 2.2. The diameters, lengths and tip orientation angles are the same in both tube pairs. The only difference between the tube pairs is the pre-curvature function along the arc length. The optimal pre-curvature is computed by Equation (2.6.43) for the given tube parameters in Table 2.2.



Figure 2.12: Two tube pairs used in experiments. The upper one is the constant pre-curvature and the lower one is the optimal pre-curvature.

Table 2.2: Tube Parameters for First Two Tube Pairs

Length (mm)		200
Collar Length (mm)		17
OD (mm) \ ID (mm)	Inner Tube	3\2.75
	Outer Tube	3.1\3.28
Tip Orientation Angle ( $^{\circ}$ )		90
Maximum Pre-curvature for Optimal Pre-curvature ( $\text{mm}^{-1}$ )		$\frac{1}{90}$
Relative Stiffness of Outer Tube with respect to Inner Tube		0.98
Expected Poisson's Ratio		0.3

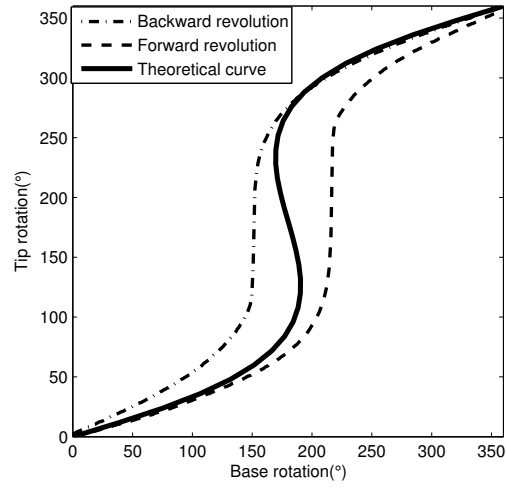


Figure 2.13: Base versus tip rotation of tube pair with constant pre-curvedness.

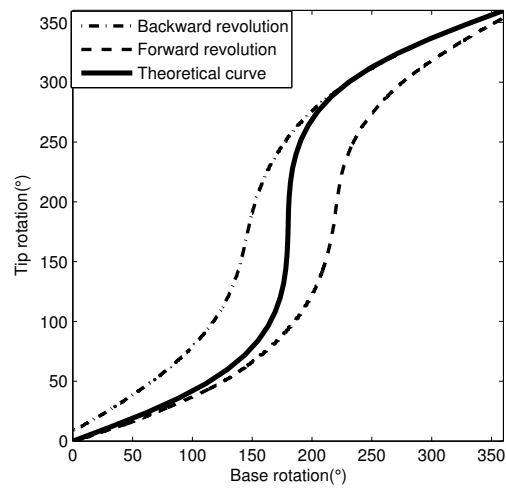


Figure 2.14: Base versus tip rotation of tube pair with optimal pre-curvedness.

The first experiment performed in this section is the comparison of the base versus tip rotation curve between the mechanics-based kinematics and the hardware experiment. Theoretical curve and measured curves of base versus tip rotation are over-plotted in Figure 2.13 and 2.14. The measured curves for forward and backward revolutions construct a band in each figure. It is due to the friction between inner tube and the outer tube which is not taken account into the derivation of mechanics-based kinematics. The theoretical curve is thus placed inside the band.

The most remarkable feature in these figures is that the tube pair with the optimal pre-curvedness presents more stable behavior, i.e., straighter curve compared to the tube pair with constant pre-curvedness. This implies that the pre-curvedness optimization presented in the previous sections are effective in the real hardware operation.

The last thing we would like to remark is that these figures does not provide much information on whether the given tube pair is stable or not. Though the tube pair with the constant pre-curvedness is intended to have unstable behavior, it is not able to observe non-monotonic increasing curve since the non-monotonic curve is not trackable with the base rotation. Instead, we can observe a jump in the workspace behavior when the tube pair snaps. However, there is no way to strictly distinguish the snapping behavior from just a fast but continuous tip movement. For this reason, we need to consider a new definition of stability/instability in practical sense.

**Definition 1.** *The given tube pair is (practically) stable if and only if the tube pair can reach any point inside the band between base versus tip curves of forward and backward revolutions by controlling the base rotation.*

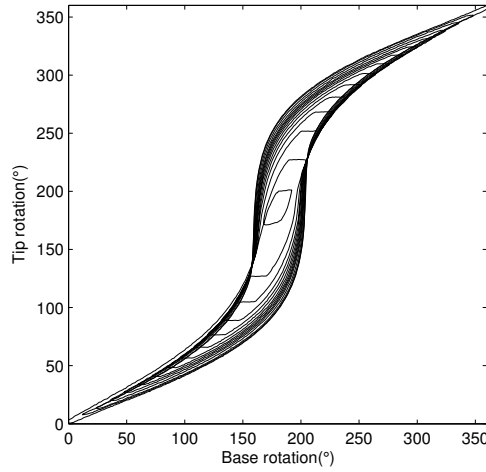


Figure 2.15: Spiral trajectory on base versus tip rotations plan for tube pair with constant pre-curvedure.

To figure out if our tube pairs are practically stable or not, we have generated a spiral trajectory inside the band. Figure 2.15 and 2.16 show the base versus tip rotations trajectory by controlling the base rotation converging to  $180^\circ$ . This results in a spiral trajectory inside the band. According to Definition 1 the tube pairs are both practically stable. It seems that the friction has stabilized the tubes by preventing tubes from snapping rapidly. That's why the both tube pairs are unintentionally stable. However, we have observed that the tube pair with constant pre-curvedure generated huge snaps at the very first revolutions. After several experiments, this snapping motions disappear and finally it is stabilized. This stabilization is observed in the curve changes between the figures. Since the experiments for Figure 2.15 and 2.16 are performed after several revolutions, the

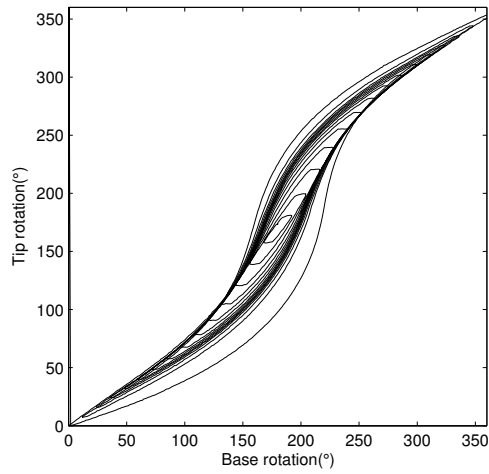


Figure 2.16: Spiral trajectory on base versus tip rotations plan for tube pair with optimal pre-curvature.

bands have become narrower and the curves become straighter compared to Figure 2.13 and 2.14. We guess that this stabilization might be caused by microscopic deformations of the tubes.

## APPENDIX: Proof of Proposition 2.1

We first prove the following two propositions:

**Proposition 2.2.** *Let  $\alpha(s, \alpha_L)$  denotes the solution to (2.3.16)-(2.4.18), and assume that  $\hat{u}_{1y}(s)$  and  $\hat{u}_{2y}(s)$  satisfy  $\hat{u}_{1y}(s), \hat{u}_{2y}(s) \geq 0$ . Then*

$$\frac{\partial \alpha}{\partial \alpha_L}(0, \alpha_L) > 0 \text{ for } \alpha_L \in [0, \pi] \quad (2.7.48)$$

if and only if

$$\frac{\partial \alpha}{\partial \alpha_L}(s, \alpha_L) > 0 \text{ for } s \in [0, L] \text{ and } \alpha_L \in [0, \pi].$$

*Proof.* The backward direction is obvious, requiring only proof of the forward direction. For notational simplicity,  $\frac{\partial \alpha}{\partial \alpha_L}$  and  $\frac{k_{1x}k_{2x}(k_{1z}+k_{2z})}{k_{1z}k_{2z}(k_{1x}+k_{2x})}$  are replaced by  $x$  and  $\kappa$ . Differentiating (2.3.16)-(2.4.18) with respect to  $\alpha_L$  yields a linear ODE

$$\ddot{x}(s, \alpha_L) = \kappa \hat{u}_{1y}(s) \hat{u}_{2y}(s) \cos(\alpha) x(s, \alpha_L) \quad (2.7.49)$$

with boundary conditions

$$x(L, \alpha_L) = 1, \quad \dot{x}(L, \alpha_L) = 0. \quad (2.7.50)$$

When  $\alpha_L = 0$ , the solution to (2.3.16)-(2.4.18) is  $\alpha(s, 0) = 0$ . In this case, Equation (2.7.49) reduces to

$$\ddot{x}(s, 0) = \kappa \hat{u}_{1y}(s) \hat{u}_{2y}(s) x(s, 0).$$

Given the boundary conditions (2.7.50) together with a positive value of  $\kappa \hat{u}_{1y} \hat{u}_{2y}$ ,  $x(s, 0)$  results in a decreasing function in  $s \in [0, L]$ , which satisfies  $x(s, 0) \geq 1$ .

Suppose there exists a solution to (2.7.49),  $x(s, \gamma)$ , which is not always positive in  $s \in [0, L]$ . Differentiating Equation (2.7.49) again with respect to  $\alpha_L$  yields

$$\begin{aligned} \frac{d^2}{ds^2} \frac{\partial x}{\partial \alpha_L}(s, \alpha_L) &= \kappa \hat{u}_{1y}(s) \hat{u}_{2y}(s) \cos(\alpha) \frac{\partial x}{\partial \alpha_L}(s, \alpha_L) \\ &\quad - \kappa \hat{u}_{1y}(s) \hat{u}_{2y}(s) \sin(\alpha) x^2(s, \alpha_L) \end{aligned}$$

Since this is also a linear ODE in  $\frac{\partial x}{\partial \alpha_L}(s, \alpha_L)$  for which the system input is associated with  $x(s, \alpha_L)$ , it leads to a finite value of  $\frac{\partial x}{\partial \alpha_L}(s, \alpha_L)$  for a finite  $x(s, \alpha_L)$ .

Consequently,  $x(s, \alpha_L)$  as well as its minimum value over  $s \in [0, L]$  is continuously varying over  $\alpha_L \in [0, \gamma]$ . Since the minimum value of  $x(s, \gamma)$  is not positive while that of  $x(s, 0)$  is 1, there exists at least one  $\alpha_L$  between 0 and  $\gamma$  for which the minimum value of  $x(s, \alpha_L)$  is zero. Let  $\beta$  and  $t$  denote this  $\alpha_L$  and corresponding minimizer, respectively. Then

$$x(t, \beta) = 0. \quad (2.7.51)$$

By (2.7.48) and (2.7.50),  $t$  is neither 0 nor  $L$ . The first-order necessary condition for the minimizer  $t$  which is not on the boundary of the domain  $s \in [0, L]$  is given by

$$\dot{x}(t, \beta) = 0. \quad (2.7.52)$$

However, this is not possible since the only solution to (2.7.49) given (2.7.51) and (2.7.52) is a constant function  $x(s, \beta) = 0$ , which does not satisfy the boundary condition (2.7.50). Thus, there does not exist any solution to (2.7.49) that is not always positive in  $s \in [0, L]$ .

□

**Proposition 2.3.** *Let  $\alpha(s, \alpha_L)$  denote the solution to (2.3.16)-(2.4.18). If*

$$\frac{\partial \alpha}{\partial \alpha_L}(s, \pi) > 0 \text{ for } s \in [0, L], \quad (2.7.53)$$

*then it satisfies*

$$\frac{\partial \alpha}{\partial \alpha_L}(s, \alpha_L) \geq \frac{\partial \alpha}{\partial \alpha_L}(s, \pi)$$

*for any  $s \in [0, L]$  and  $\alpha_L \in [0, \pi]$ .*

*Proof.* Let  $x$  and  $\kappa$  denote  $\frac{\partial \alpha}{\partial \alpha_L}$  and  $\frac{k_{1x}k_{2x}(k_{1z}+k_{2z})}{k_{1z}k_{2z}(k_{1x}+k_{2x})}$  again. By differentiating (2.3.16)-(2.4.18) with respect to  $\alpha_L$ , the same equations (2.7.49)-(2.7.50) are obtained. When  $\alpha_L = \pi$ , the solution to (2.3.16)-(2.4.18) is  $\alpha(s, \pi) = \pi$ . In this case, Equation (2.7.49) reduces to

$$\ddot{x}(s, \pi) = -\kappa \hat{u}_{1y}(s) \hat{u}_{2y}(s) x(s, \pi).$$

The proposition is clearly satisfied when  $s = L$  or  $\alpha_L = \pi$ . Suppose there exists  $t \in [0, L)$  and  $\beta \in [0, \pi)$  that does not satisfy the proposition, i.e.,

$$x(t, \beta) < x(t, \pi). \quad (2.7.54)$$

By (2.7.53), the following inequalities hold:

$$\begin{aligned} \ddot{x}(s, \pi) &\leq \kappa \hat{u}_{1y}(s) \hat{u}_{2y}(s) \cos(\alpha(s, \beta)) x(s, \pi), \\ x(t, \pi) &\geq x(t, \beta), \quad x(L, \pi) \geq x(L, \beta) \end{aligned}$$

These are the conditions for  $x(s, \pi)$  to be an upper solution [11] to  $x(s, \beta)$  over  $s \in [t, L]$ . It has been proven that any solution to an ODE lies below the upper solution. However, because of the same boundary conditions  $x(L, \beta) = x(L, \pi) = 1$ ,  $\dot{x}(L, \beta) = \dot{x}(L, \pi) = 0$  and the smaller value of the second derivative

$$\{\ddot{x}(L, \pi) = -\kappa \hat{u}_{1y}(L) \hat{u}_{2y}(L)\} < \{\ddot{x}(L, \beta) = \kappa \hat{u}_{1y}(L) \hat{u}_{2y}(L) \cos(\beta)\},$$

it follows that  $x(t, \pi)$  cannot be the upper solution near  $s = L$ . This can be shown via a Taylor expansion for a small positive scalar  $\epsilon$ :

$$x(L - \epsilon, \pi) - x(L - \epsilon, \beta) \approx \frac{1}{2} \epsilon^2 (\ddot{x}(L, \pi) - \ddot{x}(L, \beta)) < 0$$

Thus, there does not exist any  $t \in [0, L)$  and  $\beta \in [0, \pi)$  satisfying (2.7.54).

□

The forward direction of Proposition 2.1 is satisfied straightforwardly by Proposition 2.2. The backward direction is also satisfied by Proposition 2.3, i.e.,

$$\frac{\partial \alpha}{\partial \alpha_L}(s, \alpha_L) \geq \frac{\partial \alpha}{\partial \alpha_L}(s, \pi) > 0.$$



# 3

## Elastic Stability of Concentric Tube Robots Subject to External Loads

### 3.1 Introduction

Concentric tube robots are being developed for procedures throughout the body. In neurosurgery, for example, designs have been developed to access and remove skull base tumors [12] as well as to perform intraventricular procedures [4]. Lung procedures are also an area of interest since bronchoscopes are limited in how deeply they can navigate into the lungs [13, 14, 15]. Robotic catheters are being tested as a means of converting procedures currently performed via open surgery into beating-heart interventions [16, 6, 7, 17].

In designing robots for these procedures, tubes with higher pre-curvatures offer better maneuverability. As tube pre-curvature and length increase, however, instabilities can arise [1, 18, 19]. Elastic potential energy stored during bending

and twisting of the individual tubes can be suddenly released at certain configurations, creating dangerous snapping motions.

From a mechanics perspective, such snapping occurs when a configuration of the robot has a nearby configuration with lower energy, implying that the current configuration is not a stable equilibrium. For this reason an understanding of local stability, in particular an efficient and reliable method for quantitatively evaluating local stability, is important in practical applications involving concentric tube robots.

For example, the design of a concentric tube robot can be cast as a problem of finding a set of design parameters that satisfies local stability over a given range of configurations, or maximizes local stability at the most unstable configuration. In sampling-based path planning algorithms such as those based on the rapidly exploring random tree (RRT) [20], a local stability criterion can be used to define the feasible configuration space. The local stability criterion can also be used for online safety checking during real-time control, to avoid such snapping configurations.

It is also important to be able to understand and predict the effect of external loads on robot stability. A wide range of loading scenarios are possible during medical interventions. For example, concentric tube robots can be employed as steerable needles following 3D curves through solid tissue. In these situations, loads will consist of tip cutting forces and torques as well as distributed forces and torques from the tissue along the inserted length.

When introduced into a body cavity, such as the heart, the inserted portions can operate as a robot performing such tasks as manipulating tissue and deploying devices. In these scenarios, forces and torques are generated at the robot tip. Furthermore, if the robot presses against tissue along its length, this generates

distributed loads on the robot.

Existing results on the elastic stability analysis of concentric tube robots are either limited to planar tubes of constant pre-curvature, do not consider external loads, or otherwise require significant computation. The notion of elastic instabilities was first introduced in [18, 19]. A global stability condition for planar tube pairs with constant pre-curvatures was presented in [1]; here an analytic stability condition for measuring the stability of a tube pair based on the notion of an s-curve was developed. For robots comprised of more than two tubes, a multi-dimensional generalization of the s-curve was developed in [21] to determine both local and global stability.

For robots with non-constant tube pre-curvatures, an analogous stability condition based on the s-curve is presented in [22]: global stability was determined from the existence of positive solutions to a certain initial value problem, and an optimal design problem to maximize global stability was also formulated and solved. An analytic stability condition for tube pairs with constant pre-curvatures and straight transmission lengths is presented in [23], together with an implicit method to design a globally stable robot with more than two tubes.

In summary, existing works on elastic stability assume planar and constant pre-curvatures [1], or those with straight transmission lengths [23]. The multi-dimensional s-curve approach in [21] is based on the global shape of the s-curve, which requires significant off-line computations whenever the tube parameters or transmission lengths are changed. None of the prior works consider external loads in their stability analysis.

This paper presents an energy-based local stability condition for a concentric tube robot in the presence of general external loads, including distributed forces and torques along the tubes as well as concentrated forces and torques at the tip.

While point loads applied along the length are not explicitly included, they can be closely approximated using distributed loads. A mathematical condition for local stability is derived through a variational approach based on optimal control theory. Our results are applicable to robots comprised of any number of tubes. Furthermore, tube pre-curvature and stiffness can be arbitrary functions of arc length. The computations involved in evaluating local elastic stability consist simply of solving a matrix initial value problem together with the evaluation of determinants for numerical integration.

The paper is organized as follows. Section 3.2 presents the definitions and notation behind our concentric tube robot model. The elastostatic kinematic model is derived in a form suitable for stability analysis in Section 3.3 and the question of determining local elastic stability is then formulated as an optimal control problem in Section 3.4. Numerical experiments validating our stability condition are presented in Section 3.5, including tube pair examples with various external loads, and a path planning example involving a three-tube robot.

## **3.2 Concentric Tube Robot Modeling**

The shape of the concentric tube robot is determined by the initial shape and the stiffness of each tube as well as the kinematic inputs including the base rotation and translation of each tube. A rigorous mathematical modeling of the concentric tube robot requires a number of definitions of the curvature variables and coordinate frames that represent the deformed and undeformed shape of the tubes.

Consider the tubes are concentrically combined as depicted in Fig. 3.1. The kinematic inputs are the base rotations and the translations of the tubes about and along  $z$ -axis of the world coordinate frame. Let  $\theta_{0,i}$  and  $a_i$  denote the base

rotation and the translation of  $i$ -th tube, and  $s$  denotes the arc-length parameter of the robot, of which the initial value is  $a_n$  and the final value is  $b_n$ . The material

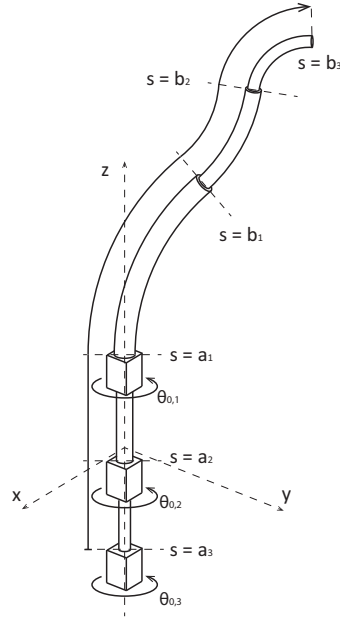


Figure 3.1: Concentric tube robot with  $n$  tubes.

coordinate frame  $R_i(s) \in SO(3)$  is then defined as a body frame rigidly attached on the infinitesimal length of material of tube  $i$  at  $s$ . Its  $z$ -axis is tangentially aligned to the tube's central axis. Then the curvature vector of tube  $i$

$$u_i(s) = \begin{bmatrix} u_{i,x}(s) & u_{i,y}(s) & u_{i,z}(s) \end{bmatrix}^T \in \mathbb{R}^3 \quad (3.2.1)$$

can be computed by

$$[u_i(s)] = \dot{R}_i(s)R_i(s)^T \quad (3.2.2)$$

where  $[r]$  denotes the skew-symmetric representation of  $r = [r_1 \ r_2 \ r_3]^T \in \mathbb{R}^3$  given

by

$$[r] = \begin{bmatrix} 0 & -r_3 & r_2 \\ r_3 & 0 & -r_1 \\ -r_2 & r_1 & 0 \end{bmatrix} \in \mathbb{R}^{3 \times 3}. \quad (3.2.3)$$

The pre-curvature vector of tube  $i$ ,  $\hat{u}_i(s) \in \mathbb{R}^3$ , is defined as the initial curvature of tube  $i$  when the tube is not subject to any external loads due to the interactions between other tubes or the environment.

Since the  $z$ -axes of the material coordinate frames  $R_i(s)$  of all the tubes are aligned tangentially to the backbone curve, they can be expressed with a reference coordinate frame,  $R(s)$ , and relative rotation angles of the tubes about the  $z$ -axis,  $\theta_i(s)$ , i.e.,

$$R_i(s) = R(s)R_z(\theta_i(s)) \quad (3.2.4)$$

where

$$R_z(\beta) = \begin{bmatrix} \cos \beta & -\sin \beta & 0 \\ \sin \beta & \cos \beta & 0 \\ 0 & 0 & 1 \end{bmatrix} \in \mathbb{R}^{2 \times 2} \quad (3.2.5)$$

Note that any arbitrary choice of the reference frame  $R(s)$  is possible. We have chosen a Bishop frame [24] as the reference frame since the curvature vector of a Bishop frame has only two non-zero components, the  $x$  and  $y$  components. The Bishop frame  $R(s)$  and the backbone curve  $p(s) \in \mathbb{R}^3$  are then given by

$$\dot{R}(s) = R(s)[(u_x, u_y, 0)] \quad (3.2.6)$$

$$\dot{p}(s) = R(s)\hat{e}_z \quad (3.2.7)$$

where  $u_x(s), u_y(s) \in \mathbb{R}$  are the backbone bending curvatures, and  $\hat{e}_z$  is the unit vector in the  $z$ -direction, i.e.,  $\hat{e}_z = [0 \ 0 \ 1]^T$ . The initial value of  $R(s)$  is chosen to be an identity matrix, i.e.,  $R(a_n) = I$ .

Additional properties that determine the shape of the combined tubes are the bending stiffness and the torsional stiffness of each of the tubes along the length. Let  $K_i(s) \in \mathbb{R}^{3 \times 3}$  denote the stiffness matrix of tube  $i$  at  $s$ . Since the cross section of each tube is an annulus, the bending moment about  $x$ -axis and  $y$ -axis are the same. The stiffness matrix  $K_i(s)$  is then given by

$$K_i(s) = \begin{bmatrix} k_{i,xy}(s) & 0 & 0 \\ 0 & k_{i,xy}(s) & 0 \\ 0 & 0 & k_{i,z}(s) \end{bmatrix} \quad (3.2.8)$$

where  $k_{i,xy}(s)$  is the bending stiffness and  $k_{i,z}(s)$  is the torsional stiffness.

As shown in Fig. 3.1, tube  $i$  does not exist over the entire arc-length interval  $[a_n, b_n]$ , but only in the interval  $s \in [a_i, b_i]$ . For convenience, let us introduce an equivalent model by imagining virtual tubes at the tips and the bases of the actual tubes.

Fig. 3.2 shows an example of the equivalent model using virtual tubes. At the proximal end, virtual tubes have zero curvature and infinite bending and torsional stiffness, while those at the tips have zero curvature, zero bending stiffness and arbitrary positive torsional stiffness.

### 3.3 Elastostatic Kinematic Model

This section presents an energy-based derivation of the elastostatic kinematics of concentric tube robots subject to distributed loads over the length and concentrated loads at the tip. While prior work has presented concentric tube robot kinematics under external loads [25, 26], a formulation is derived here in a form suitable for assessing local stability. This differs from prior formulations in the representation of external loads and cross-sectional internal moments.

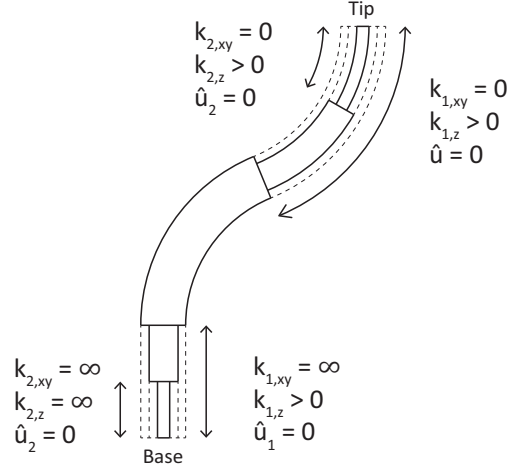


Figure 3.2: Equivalent tube model.

### 3.3.1 Concentric Tube Robot with No External Load

Consider a concentric tube robot with  $n$  tubes in the absence of any external loads. The potential energy of the system is then given by the sum of the elastic potential energies of each of the tubes. The potential energy functional is then given by

$$J = \int_{a_n}^{b_n} \sum_{i=1}^n \frac{1}{2} (u_i(s) - \hat{u}_i(s))^T K_i(s) (u_i(s) - \hat{u}_i(s)) ds. \quad (3.3.9)$$

Since the tubes are concentric, the  $x$ - $y$  curvatures of the tubes are identical to the backbone bending curvature expressed in different material coordinate frames. In order to reduce the number of variables, the bending curvatures of the tubes are expressed as a single variable  $u_{xy}(s) \in \mathbb{R}^2$ , which is the Bishop frame representation of the  $x$ - $y$  curvature of the backbone curve. Let  $\theta_i(s) \in \mathbb{R}$  denote the rotation of tube  $i$  along the arclength, i.e.,

$$\dot{\theta}_i(s) = u_{i,z}(s) \quad (3.3.10)$$

where the upper dot represents the derivative taken with respect to the arclength parameter  $s$ , and  $\theta_i(a)$  is given as a kinematic input. The bending curvature of tube  $i$  is then expressed as

$$u_{i,xy}(s) = R_z(\theta_i(s))|_{xy}^T u_{xy}(s) \in \mathbb{R}^2, \quad (3.3.11)$$

where

$$R_z(\beta)|_{xy} = \begin{bmatrix} \cos \beta & -\sin \beta \\ \sin \beta & \cos \beta \end{bmatrix} \in \mathbb{R}^{2 \times 2}, \quad (3.3.12)$$

$$u_{i,xy}(s) = \begin{bmatrix} u_{i,x}(s) \\ u_{i,y}(s) \end{bmatrix} \in \mathbb{R}^2. \quad (3.3.13)$$

Substituting  $u_{xy}$  into Equation (3.3.9) yields

$$J = \int_a^b g(u_{xy}(s), \theta(s), \dot{\theta}(s)) ds, \quad (3.3.14)$$

where

$$\theta(s) = [\theta_1(s) \cdots \theta_n(s)]^T \in \mathbb{R}^n, \quad (3.3.15)$$

$$g(u_{xy}, \theta, \dot{\theta}) = \sum_{i=1}^n \frac{1}{2} \left\{ k_{i,xy} \| R_z(\theta_i)|_{xy}^T u_{xy} - \hat{u}_{i,xy} \|^2 + k_{i,z} (\dot{\theta}_i - \hat{u}_{i,z})^2 \right\}. \quad (3.3.16)$$

The potential energy  $J$  in the above equation is a functional of  $\dot{\theta}_i(s)$  as well as  $u_{xy}(s), \theta_i(s)$ , which results in a standard calculus of variation problem. The unloaded kinematics is then obtained by applying the Euler-Lagrange equation to (3.3.14).

### 3.3.2 Concentric Tube Robot with External Load

Let us first assume that conservative forces are applied as the external loads. Then there exists a total potential energy, including the elastic potential energy of the

tubes and the potential energy by the external forces, of the form

$$J = \int_{a_n}^{b_n} g(u_{xy}, \theta, u_z) + w(p, R, \theta, s) ds + W(p(b_n), R(b_n), \theta(b_n), b_n) \quad (3.3.17)$$

where  $u_z(s) = [u_{1,z}(s) \cdots u_{n,z}(s)]^T \in \mathbb{R}^n$ ,  $p(s) \in \mathbb{R}^3$  is the backbone curve, and  $R(s) \in \mathbb{R}^{3 \times 3}$  is the Bishop frame along the arc-length; these satisfy

$$\dot{p}(s) = R\hat{e}_z \quad (3.3.18)$$

$$\dot{R}(s) = R[(u_x, u_y, 0)]. \quad (3.3.19)$$

The term  $w(p(s), R(s), \theta(s), s)$  is the potential density function of the distributed loads at  $s \in [a, b]$ , and  $W(p(b_n), R(b_n), \theta(b_n), b_n)$  is the potential energy function of the concentrated load applied to the tip. Solving for the backbone curve, consisting of the state variables  $x(s) = (p(s), R(s), \theta(s))$ , that minimizes elastic potential energy (3.3.17) can be interpreted as an optimal control problem in which  $u(s) = (u_{xy}(s), u_z(s))$  comprise the input variables. The first variation of Equation (3.3.17) should be zero; this yields the well-known first-order necessary condition for optimal control:

$$\dot{x} = \frac{\partial H}{\partial \lambda}, \quad \dot{\lambda} = -\frac{\partial H}{\partial x}, \quad \frac{\partial H}{\partial u} = 0, \quad (3.3.20)$$

with boundary conditions

$$\begin{aligned} x(a_n) & \text{ (given as kinematic inputs)} \\ \lambda(b_n) & = \frac{\partial W}{\partial x}(b_n), \end{aligned} \quad (3.3.21)$$

where the Hamiltonian  $H$  is defined as

$$\begin{aligned}
H = & \frac{1}{2} \sum_{i=1}^n \{k_{i,xy} \|R_z^T(\theta_i)u_{xy} - \hat{u}_{i,xy}\|^2 \\
& + k_{i,z}(\dot{\theta}_i - \hat{u}_{i,z})^2\} + w(p, R, s) \\
& + \lambda_p^T R \hat{e}_z + Tr(\lambda_R^T R[(u_x, u_y, 0)]) + \lambda_\theta^T u_z.
\end{aligned} \tag{3.3.22}$$

The elastostatic kinematics of the concentric tube robot subject to conservative loads is then obtained from the first-order condition (3.3.20). Substituting the Hamiltonian (3.3.22) into (3.3.20) yields the following differential equations:

$$\begin{aligned}
\dot{p} &= R \hat{e}_z, \quad \dot{R} = R[(u_x, u_y, 0)], \quad \dot{\theta}_i = u_{i,z}, \\
\dot{\lambda}_p &= -\frac{\partial w}{\partial p}, \\
\dot{\lambda}_R &= -\frac{\partial w}{\partial R} - \lambda_p \hat{e}_z^T + \lambda_R[(u_x, u_y, 0)], \\
\dot{\lambda}_{\theta_i} &= -\frac{\partial w}{\partial \theta_i} + k_{i,xy} u_{xy}^T \frac{dR_z(\theta_i)}{d\theta_i} \hat{u}_{i,xy}.
\end{aligned} \tag{3.3.23}$$

Here  $u_{xy}, u_{i,z}$  are given by

$$u_{xy} = \frac{- \begin{bmatrix} Tr(\lambda_R^T R[\hat{e}_x]) \\ Tr(\lambda_R^T R[\hat{e}_y]) \end{bmatrix} + \sum_{i=1}^n k_{i,xy} R_z(\theta_i) \begin{bmatrix} \hat{u}_{i,x} \\ \hat{u}_{i,y} \end{bmatrix}}{\sum_{i=1}^n k_{i,xy}} \tag{3.3.24}$$

$$u_{i,z} = -\lambda_{\theta_i} / k_{i,z}$$

where  $\hat{e}_x = [1 \ 0 \ 0]^T$ ,  $\hat{e}_y = [0 \ 1 \ 0]^T$  and  $\hat{e}_z = [0 \ 0 \ 1]^T$ . The boundary conditions are given by

$$\begin{aligned}
p(a_n) &= [0 \ 0 \ a_n]^T, \quad R(a_n) = I, \quad \theta(a_n) = \theta_{\text{base}}, \\
\lambda_p(b_n) &= \frac{\partial W}{\partial p}, \quad \lambda_R(b_n) = \frac{\partial W}{\partial R}, \quad \lambda_\theta(b_n) = \frac{\partial W}{\partial \theta}.
\end{aligned} \tag{3.3.25}$$

Now consider the case when nonconservative loads are applied to the robot. These can consist of non-conservative distributed loads  $v(p(s), R(s), \theta(s), s)$  and

non-conservative concentrated tip loads  $V(p(b_n), R(b_n), \theta(b_n), b_n)$ . Then, in order to be a static equilibrium, the first energy variation,  $\delta J$ , must equate to an infinitesimal increment of work done by the non-conservative loads,  $\delta W_{nc}$ , for any perturbation in  $u(s)$ , i.e.,

$$\delta J = \delta W_{nc}. \quad (3.3.26)$$

In this case, the differential equations involving  $\lambda$  in (3.3.23) become

$$\begin{aligned} \dot{\lambda}_p &= -\frac{\partial w}{\partial p} + v_p, \\ \dot{\lambda}_R &= -\frac{\partial w}{\partial R} + v_R - \lambda_p \hat{e}_z^T + \lambda_R [(u_x, u_y, 0)], \\ \dot{\lambda}_{\theta_i} &= -\frac{\partial w}{\partial \theta_i} + v_{\theta_i} + k_{i,xy} u_{xy}^T \frac{dR_z(\theta_i)}{d\theta_i} \hat{u}_{i,xy} \end{aligned} \quad (3.3.27)$$

with the boundary conditions

$$\lambda_p(b_n) = \frac{\partial W}{\partial p} - V_p, \quad \lambda_R(b_n) = \frac{\partial W}{\partial R} - V_R, \quad \lambda_{\theta}(b_n) = \frac{\partial W}{\partial \theta} - V_{\theta}. \quad (3.3.28)$$

Note that  $v_p$ ,  $v_R$  and  $v_{\theta_i}$  are components of  $v$ . Also,  $V_p$ ,  $V_R$ , and  $V_{\theta}$  are the components of  $V$  corresponding to  $p$ ,  $R$ , and  $\theta_i$ , respectively.

The Lagrange multipliers  $\lambda_p, \lambda_R$  and  $\lambda_{\theta}$  in the equations are physically interpreted as the (negative) generalized forces applied to the generalized coordinates  $p, R$  and  $\theta$ . Note that  $-\lambda_p$  and the  $i$ -th component of  $-\lambda_{\theta}$  are, respectively, the linear force and the  $z$ -directional moment of the  $i$ -th tube on the cross section of the robot. The variable  $-\lambda_R$  also represents the  $x, y$ -moments on the cross section of the robot.

More familiar representations of the  $x, y$ -moments are obtained by projecting the generalized force  $-\lambda_R$  onto the tangent space of the rotation group  $SO(3)$ . We adopt the following exponential local coordinate representation for a rotation matrix about  $R_0$ :

$$R = R_0 \exp([w]) \quad (3.3.29)$$

where  $w \in \mathbb{R}^3$  is the local coordinate variable [27]. Unit velocities along the  $x$ - and  $y$ -directions of the local coordinates yield the tangent vectors of the rotation matrix, whose components are given by

$$t_x = R_0 [\hat{e}_x] \in \mathbb{R}^{3 \times 3} \quad (3.3.30)$$

$$t_y = R_0 [\hat{e}_y] \in \mathbb{R}^{3 \times 3}. \quad (3.3.31)$$

The  $x, y$  moments on the cross section are then given by the inner products of  $-\lambda_R$  with  $t_x$  and  $t_y$ :

$$m_x = -Tr(\lambda_R^T R_0 [\hat{e}_x]) \quad (3.3.32)$$

$$m_y = -Tr(\lambda_R^T R_0 [\hat{e}_y]). \quad (3.3.33)$$

Substituting  $m_x$  and  $m_y$  into (3.3.24), the resulting kinematic equations (3.3.23), (3.3.24) are equivalent to the mechanics-based kinematics derived in [25, 26].

### 3.3.3 Generalized Force Representation of External loads

Just as the Lagrange multipliers  $(\lambda_p, \lambda_R, \lambda_\theta)$  can be interpreted as generalized forces, the distributed loads  $(v_p(s), v_R(s), v_\theta(s))$  and the concentrated tip loads  $(V_p, V_R, V_\theta)$  appearing in the kinematic equations of Section 3.3.2 are now expressed as distributed generalized forces. Since the loads are not expressed in the form of generalized forces, but rather as a moment-force pair (or wrench)  $(m, f) \in \mathbb{R}^3 \times \mathbb{R}^3$ , the generalized force representation of the moment-force pair  $(m, f)$  is derived in this section.

We assume that the distributed load  $(m(s), f(s))$  is expressed in the world frame, and applied to the  $i$ -th tube. Note that it is important to specify which tube the loads are applied to, since a twisting moment applied to a different tube

may result in a different configuration. Now consider an infinitesimal amount of work performed over an infinitesimal displacement in  $R_i(s)$  and  $p(s)$ , i.e.,

$$\begin{aligned}\delta W &= (R_i(s)^T m(s))^T \delta w + f(s)^T \delta p(s) \\ &= Tr \left( \frac{1}{2} [R_i(s)^T m(s)]^T [\delta w] \right) + f(s)^T \delta p(s)\end{aligned}\quad (3.3.34)$$

where  $\delta w \in \mathbb{R}^3$  is an infinitesimal displacement of the local coordinate variable  $w$  about  $R_i(s)$  (also defined in Section 3.3.2). Then the corresponding infinitesimal displacement in  $R_i(s)$ , denoted  $\delta R_i(s) \in \mathbb{R}^{3 \times 3}$ , is given by

$$\delta R_i(s) = R_i(s)[\delta w]. \quad (3.3.35)$$

From the relation  $R_i(s) = R(s)R_z(\theta_i(s))$ ,  $\delta R_i(s)$  can be expressed in terms of infinitesimal displacements in  $R(s)$  and  $\theta_i(s)$ :

$$\delta R_i(s) = \delta R(s)R_z(\theta_i(s)) + R(s)R_z(\theta_i(s))[\hat{e}_z]\delta\theta_i(s). \quad (3.3.36)$$

Substituting (3.3.35) and (3.3.36) into (3.3.34) yields

$$\begin{aligned}\delta W &= Tr \left( \frac{1}{2} R(s)^T [m(s)]^T \delta R(s) \right) \\ &\quad + R(s)^T m(s) \Big|_z \delta\theta_1(s) + f(s) \delta p(s)\end{aligned}\quad (3.3.37)$$

where  $|_z$  denotes the third component of a vector in  $\mathbb{R}^3$ . Since the generalized coordinate representation of the infinitesimal work done by the generalized forces  $v_p(s)$ ,  $v_R(s)$ , and  $v_{\theta_i}(s)$  is given by  $v_p(s)^T \delta p(s) + Tr(v_R^T(s) \delta R(s)) + v_{\theta_1}(s) \delta\theta_1(s)$ , the generalized forces can be expressed as

$$\begin{aligned}v_p(s) &= f(s) \\ v_R(s) &= \frac{1}{2} [m(s)] R(s) \\ v_{\theta_i}(s) &= R(s)^T m(s) \Big|_z.\end{aligned}\quad (3.3.38)$$

In the same manner, the generalized representation of the concentrated tip load,  $(M, F) \in \mathbb{R}^3 \times \mathbb{R}^3$ , is given by

$$\begin{aligned} V_p &= F \\ V_R &= \frac{1}{2}[M]R(b_n) \\ V_{\theta_i} &= R(b_n)^T M|_z. \end{aligned} \tag{3.3.39}$$

Note that if the loads  $(m(s), f(s))$  and  $(M, F)$  are expressed in any other arbitrary frame  $R'$ ,  $(m(s), f(s))$  and  $(M, F)$  in Equation (3.3.38), (3.3.39) are then replaced by  $(R'^T m(s), R'^T f(s))$  and  $(R'^T M, R'^T F)$ , respectively.

## 3.4 Evaluating Local Elastic Stability

### 3.4.1 Preliminaries

We begin with some preliminaries from variational mechanics. Consider an  $n$ -dimensional mechanical system with generalized coordinates  $x = x(t) \in V$ , and a functional  $J(x)$ . The solution  $x^*$  is an equilibrium of  $J$  if the first variation of  $J$  at  $x^*$  is zero for all admissible perturbations,  $\eta \in V$ , i.e.,

$$\delta J|_{x^*}(\eta) = 0, \tag{3.4.40}$$

where the first variation is obtained from a series expansion of  $J(x)$  about  $x^*$ :

$$J(x^* + \eta) = J(x^*) + \delta J|_{x^*}(\eta) + \frac{1}{2} \delta^2 J|_{x^*}(\eta) + \dots \tag{3.4.41}$$

The equilibrium  $x^*$  is stable if its second variation is positive for all admissible perturbations  $\eta \in V$ , i.e.,

$$\delta^2 J|_{x^*}(\eta) > 0. \tag{3.4.42}$$

### 3.4.2 Jacobi Non-Conjugacy Test for Conservative External Loads

When the external loads are conservative, the total potential energy can be defined as given in (3.3.17). In this case, a necessary and sufficient local stability condition can be based on the Jacobi non-conjugacy condition. This condition originates in optimal control and is used to discriminate if a stationary solution satisfying first-order necessary conditions is a local minimum. It provides an efficient and simple test involving the second variation that is equivalent to the condition for the second variation to be positive for any perturbation [28, 29].

For potential energy functions of the form (3.3.17), the second variation evaluated at a stationary solution,  $(x^*, \lambda^*, u^*)$ , satisfying the first order condition is explicitly given by

$$\delta^2 J = \frac{1}{2} \int_{a_n}^{b_n} \begin{bmatrix} \eta^T & \xi^T \end{bmatrix} \begin{bmatrix} A & B \\ B^T & C \end{bmatrix} \begin{bmatrix} \eta \\ \xi \end{bmatrix} ds + \frac{1}{2} \eta^T D \eta \quad (3.4.43)$$

with the matrices  $A(s), B(s), C(s)$  and  $D$  given by

$$\begin{aligned} A &= \frac{\partial^2 H^*}{\partial x^2}, & B &= \frac{\partial^2 H^*}{\partial x \partial u} \\ C &= \frac{\partial^2 H^*}{\partial u^2}, & D &= \frac{\partial^2 W^*}{\partial x^2}. \end{aligned} \quad (3.4.44)$$

Here  $\eta(s)$  and  $\xi(s)$  are the perturbations in the state and input, respectively, satisfying the linear state equation

$$\dot{\eta} = \frac{\partial f^*}{\partial x} \eta + \frac{\partial f^*}{\partial u} \xi, \quad (3.4.45)$$

where  $\dot{x} = f(x, u)$  is the combination of the state equations (3.3.10), (3.3.18) and (3.3.19).

For a second variation of the form (3.4.43), the local stability test using the Jacobi non-conjugacy condition is as follows:

- (i) Solve a backward initial value problem for the differential equation

$$\dot{\Theta} = P\Theta \quad (3.4.46)$$

with the following boundary condition:

$$\Theta(b_n) = I \in \mathbb{R}^{(24+2n) \times (24+2n)}, \quad (3.4.47)$$

where  $P$  is defined as

$$P = \begin{bmatrix} P_1 & -P_2 \\ -P_0 & P_1^T \end{bmatrix} \quad (3.4.48)$$

with

$$\begin{aligned} P_0 &= A - BC^{-1}B^T \\ P_1 &= \frac{\partial f^*}{\partial x} - \frac{\partial f^*}{\partial u} C^{-1}B^T \\ P_2 &= \frac{\partial f^*}{\partial u} C^{-1} \frac{\partial f^{*T}}{\partial u} \end{aligned} \quad (3.4.49)$$

where  $A(s)$ ,  $B(s)$  and  $C(s)$  are given in (3.4.44). We remark again that  $x = f(x, u)$  is the combination of the state equations (3.3.10), (3.3.18) and (3.3.19).

- (ii) Consider a partitioning of  $\Theta$  into  $(12+n) \times (12+n)$  sub-matrices of the form

$$\Theta = \begin{bmatrix} \Theta_{xx} & \Theta_{x\lambda} \\ \Theta_{x\lambda}^T & \Theta_{\lambda\lambda} \end{bmatrix}. \quad (3.4.50)$$

Define  $X(s) \in \mathbb{R}^{(12+n) \times (12+n)}$  as

$$X(s) = \Theta_{xx}(s) + \Theta_{x\lambda}(s)D \quad (3.4.51)$$

where  $D$  is given in (3.4.44). Then Jacobi nonconjugacy condition can now be stated as follows: if there is no  $c \in (a_n, b_n)$  that satisfies  $\det(X(c)) = 0$ , the given stationary solution is a local minimum, which results in local

stability of the concentric tube robot. On the other hand, if there exists  $c \in (a_n, b_n)$  that satisfies  $\det(X(c)) = 0$ , there is a configuration with less energy near the stationary solution.

Note that the computations involved in this stability test consist of solving a matrix initial value problem and computing determinants during the integration. We remark that in the absence of external loads,  $\Theta$  reduces to a  $2n \times 2n$  matrix, and the initial value problem for  $\Theta$  also reduces to a  $2n \times 2n$  IVP defined with  $n \times n$  lower-right sub-matrices  $P_0, P_1, P_2$ , and  $D$ . The resulting  $X(s)$  is then an  $n \times n$  matrix.

### 3.4.3 Physical Interpretation of Jacobi Non-Conjugacy Condition

The non-conjugacy condition presented above has an intuitive interpretation in terms of the differential kinematics of the robot. Consider a solution to the kinematics (3.3.23)-(3.3.24),  $(x^*, \lambda^*, u^*)$ , for the given boundary conditions (3.3.25). Now suppose that the state variables at the tip are slightly varied. In this situation, we can consider a Jacobian matrix  $G(s, b_n)$  that maps the tip variation,  $\delta x(b_n)$ , to the variation at  $s$ ,  $\delta x(s)$ , i.e.,

$$\delta x(s) = G(s, b_n) \delta x(b_n). \quad (3.4.52)$$

The Jacobian matrix  $G(s, b_n)$  can be computed by solving a set of linear ODEs with boundary conditions that are obtained by linearizing the kinematics (3.3.23)-(3.3.24) and the boundary condition (3.3.25) at the solution  $(x^*, \lambda^*, u^*)$ . This is an backward IVP problem whose initial value is given by  $G(b_n, b_n) = I$ . In fact, it can be shown that the Jacobian matrix  $G(s, b_n)$  is given by  $X(s)$  of (3.4.51) when the external loads are conservative. (See Appendix.)

Thus the stability condition is equivalent to a condition for the Jacobian matrix,  $G(s, b_n)$ , to have a nonzero determinant over the entire robot length,  $s \in (a, b)$ . To develop this interpretation further, consider a configuration that has a zero determinant value when evaluated at the base,

$$\det(G(a_n, b_n)) = 0. \quad (3.4.53)$$

In this case, since the matrix  $G(a_n, b_n)$  has a non-zero null space vector, there exists a tip variation  $\delta x(b_n)$  which produces zero variation at the base or, equivalently, a small base variation generates an infinitely large variation at the tip. This is clearly unstable.

Now consider the case of a zero determinant lying inside the interval  $c \in (a_n, b_n)$ , i.e.,

$$\det(G(c, b_n)) = 0. \quad (3.4.54)$$

Consider that the robot is comprised of a serial concatenation of two robots. The first extends over arc length  $s \in (a_n, c)$  and the second extends over  $s \in (c, b_n)$ . With this construction, the tip of the first robot controls the base of the second robot. By the argument of the preceding paragraph, the second robot is clearly unstable and, consequently, so is the concatenation. Thus, local stability, as derived above, corresponds to a physical interpretation that the determinant  $G(s, b_n)$  should be nonzero over the entire interval,  $s \in (a_n, b_n)$ .

#### 3.4.4 Non-Conservative External Loads

The Jacobi non-conjugacy condition cannot be directly applied to cases that include non-conservative external loads since the system is not completely described

by an energy function. In contrast to potential energy, however, the Jacobian matrix can be computed regardless of the types of loads applied. Thus, the Jacobian-based interpretation of local stability can be easily extended to the case of non-conservative loads by simple modification of the matrix  $X(s)$  in (3.4.51). A generalized condition based on the Jacobian matrix can be defined as follows:

- (i) Solve a backward initial value problem for the differential equation

$$\dot{\Theta} = P\Theta \quad (3.4.55)$$

with the following boundary condition:

$$\Theta(b_n) = I \in \mathbb{R}^{(24+2n) \times (24+2n)}, \quad (3.4.56)$$

where  $P$  is defined as

$$P = \begin{bmatrix} P_1 & -P_2 \\ -P_0 & P_1^T \end{bmatrix} \quad (3.4.57)$$

with

$$\begin{aligned} P_0 &= A' - BC^{-1}B^T \\ P_1 &= \frac{\partial f^*}{\partial x} - \frac{\partial f^*}{\partial u} C^{-1}B^T \\ P_2 &= \frac{\partial f^*}{\partial u} C^{-1} \frac{\partial f^{*T}}{\partial u} \end{aligned} \quad (3.4.58)$$

where  $B(s), C(s)$  are given in (3.4.44), and  $A'(s)$  is defined as

$$A'(s) = \frac{\partial^2 H^*}{\partial x} - \frac{\partial v^*}{\partial x}. \quad (3.4.59)$$

Here,  $v(p(s), R(s), \theta(s), s)$  is the non-conservative distributed load at  $s$ .

- (ii) Consider a partitioning of  $\Theta$  into  $(12+n) \times (12+n)$  sub-matrices of the form

$$\Theta = \begin{bmatrix} \Theta_{xx} & \Theta_{x\lambda} \\ \Theta_{x\lambda}^T & \Theta_{\lambda\lambda} \end{bmatrix}. \quad (3.4.60)$$

Define  $X(s) \in \mathbb{R}^{(12+n) \times (12+n)}$  as

$$X(s) = \Theta_{xx}(s) + \Theta_{x\lambda}(s)D' \quad (3.4.61)$$

where  $D'$  is given by

$$D' = \frac{\partial^2 W^*}{\partial x^2} - \frac{\partial V^*}{\partial x}. \quad (3.4.62)$$

$V(p(b_n), R(b_n), \theta(b_n), b_n)$  denotes the non-conservative tip load.

If it satisfies  $\det(X(s)) \neq 0$  over  $s \in (a_n, b_n)$ , the given configuration is stable.

Otherwise, the configuration is unstable.

Note that, when the external loads  $v$  and  $V$  are, in fact, conservative, this condition reduces to the condition for conservative loads presented in Section 3.4.2. Thus, when there are many types of external loads, one does not need to classify the loads into conservative and non-conservative loads. The test above can be employed with all distributed and tip loads, regardless of type, substituted into  $v$  and  $V$ , respectively.

### 3.5 Examples

To facilitate understanding of the stability criterion, a series of examples are presented involving constant curvature tube pairs. These examples are used since their unloaded stability has been previously derived [1, 23] and stability can also be presented graphically. In addition, an example demonstrating use of the criterion for stable path planning of a 3-tube robot is also presented.

### 3.5.1 Example 1: Stability of an Unloaded Constant-precurvature Tube Pair

When a pair of tubes of equal pre-curvature and stiffness are rotated with respect to each other, their mutual curvature varies between the pre-curvature value and zero (straight) as shown in Fig. 3.3. The unloaded stability of such tube pairs has been derived previously and can be represented graphically as shown in Fig. 3.4, which plots relative rotation angle of the tubes at their tip as a function of relative rotation angle at their base [1]. When a tube pair is globally stable, there exists a unique relative rotation angle at the tips of the tubes for each relative rotation angle at the base. This case is depicted in Fig. 3.4(a).

Configurations can be unstable when multiple tip rotations are associated with the same base rotation. This situation is shown in Fig. 3.4(b) for configurations with base rotations in the neighborhood of  $180^\circ$ . The stability of a specific solution depends on whether or not perturbations to that solution lead a lower-energy solution. As the tubes are rotated at their base from  $0^\circ$ , they traverse a stable portion of the curve and then jump over the higher-energy unstable solutions to the other stable branch.

As a specific example, consider a tube pair with Example 1 parameters given in Table 3.1. This tube pair possesses unstable configurations as shown in Fig. 3.5(a). The three labeled points correspond to the three scenarios described in subsection 3.4.3, which are plotted in Fig. 3.5(b). Stable point 3 corresponds to the case when the Jacobian mapping tip variations to variations at  $s$  is nonsingular for the entire length of the tubes. Point 2 corresponds to the Jacobian becoming singular at the base - indicating that an infinite base variation is associated with small tip variation. In Fig. 3.5(a), this corresponds to the jump from one stable

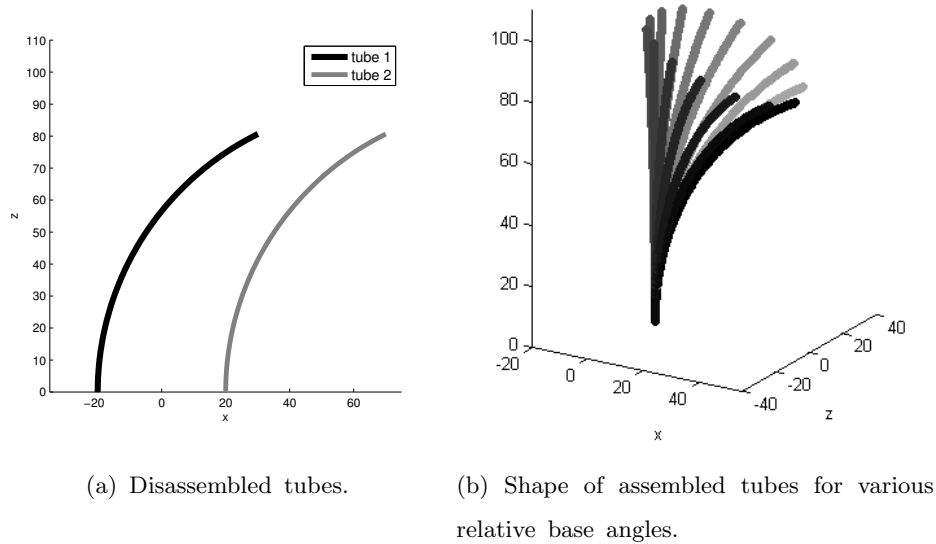


Figure 3.3: Variable curvature tube pair.

branch to the other. Finally, point 3 corresponds to the case when the Jacobian is singular in the interior of the arc length interval.

### 3.5.2 Example 2: Stability of a Constant Precurvature Tube Pair Subject to Elastic Forces

Now consider the effect of elastic forces arising, e.g., from contact with tissue, on the stability of a variable curvature tube pair with Example 2 parameters as given in Table 3.1. As shown in Fig. 3.6, the distributed and concentrated elastic forces,

Table 3.1: Tube and load parameters for examples. Units for load parameters are normalized with respect to bending stiffness units (force-length<sup>2</sup>).

		Tube 1			Tube 2	
		Section 1	Section 1	Section 2		
<b>Example 1</b>	Length (mm)	100	17	100		
	Curvature (mm <sup>-1</sup> )	1/60	0.0	1/60		
	Bending Stiffness	1	1	1		
	Torsional Stiffness	1/1.3	1/1.3	1/1.3		
	$a_i$ (mm)	0	-17			
	$b_i$ (mm)	100	100			
<b>Example 2</b>	Length (mm)	100	17	100		
	Curvature (mm <sup>-1</sup> )	1/79	0.0	1/79		
	Bending Stiffness	1	1	1		
	Torsional Stiffness	1/1.3	1/1.3	1/1.3		
	$a_i$ (mm)	0	-17			
	$b_i$ (mm)	100	100			
	$k_{f_e}$ (mm <sup>-4</sup> )	$1.0 \times 10^{-7}$				
	$k_{F_e}$ (mm <sup>-3</sup> )	$1.0 \times 10^{-5}$				
<b>Example 3</b>	Length (mm)	100	17	100		
	Curvature (mm <sup>-1</sup> )	1/60	0.0	1/60		
	Bending Stiffness	1	1	1		
	Torsional Stiffness	1/1.3	1/1.3	1/1.3		
	$a_i$ (mm)	0	-17			
	$b_i$ (mm)	100	100			
	$m$ (mm <sup>-2</sup> )	$[5.0 \ 5.0 \ 5.0]^T \times 10^{-5}$				
	$M$ (mm <sup>-1</sup> )	$[5.0 \ 5.0 \ 5.0]^T \times 10^{-3}$				
	$f$ (mm <sup>-3</sup> )	$[5.0 \ 5.0 \ 5.0]^T \times 10^{-7}$				
	$F$ (mm <sup>-2</sup> )	$[5.0 \ 5.0 \ 5.0]^T \times 10^{-5}$				

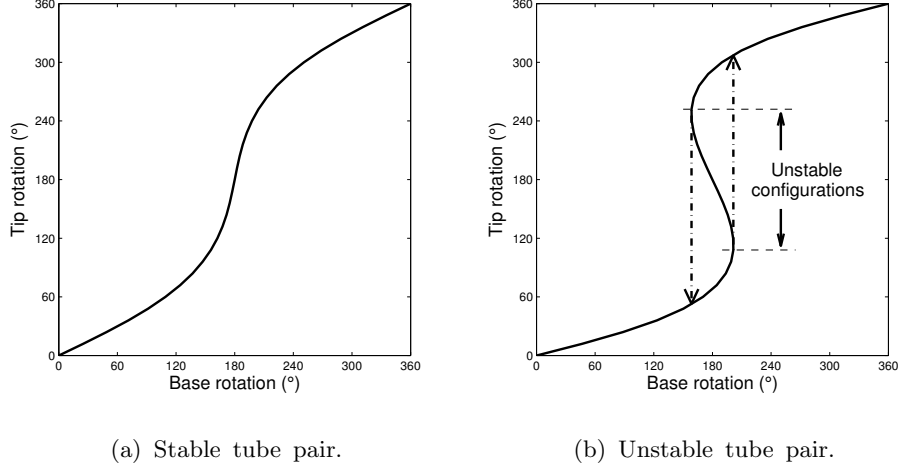


Figure 3.4: Relative rotation of tubes at their tips versus their bases. Dashed lines in (b) show jumps between branches of stable solutions.

$f_e \in \mathbb{R}^3$  and  $F_e \in \mathbb{R}^3$ , are given by

$$f_e(p(s), s) = k_{f_e}(s)(p(s) - c_{f_e}(s)) \quad (3.5.63)$$

$$F_e(p(b_n)) = k_{F_e}(p(b_n) - c_{F_e}) \quad (3.5.64)$$

where  $c_{f_e}(s) \in \mathbb{R}^3$  is the spring centerline for the distributed elastic force, and  $c_{F_e} \in \mathbb{R}^3$  is the spring center of the elastic tip force.  $k_{f_e}(s) \in \mathbb{R}$  and  $k_{F_e} \in \mathbb{R}$  are the stiffness functions of the distributed elastic force and the stiffness of the elastic tip force, respectively.

To compare our results with those obtained from relative rotation plots as shown above, the forces are defined to be invariant under rotations of the tube set about its base. This is equivalent to fixing  $c_{f_e}(s)$  and  $c_{F_e}$  in the world frame and performing relative rotation of the tubes such that the robot's plane of curvature

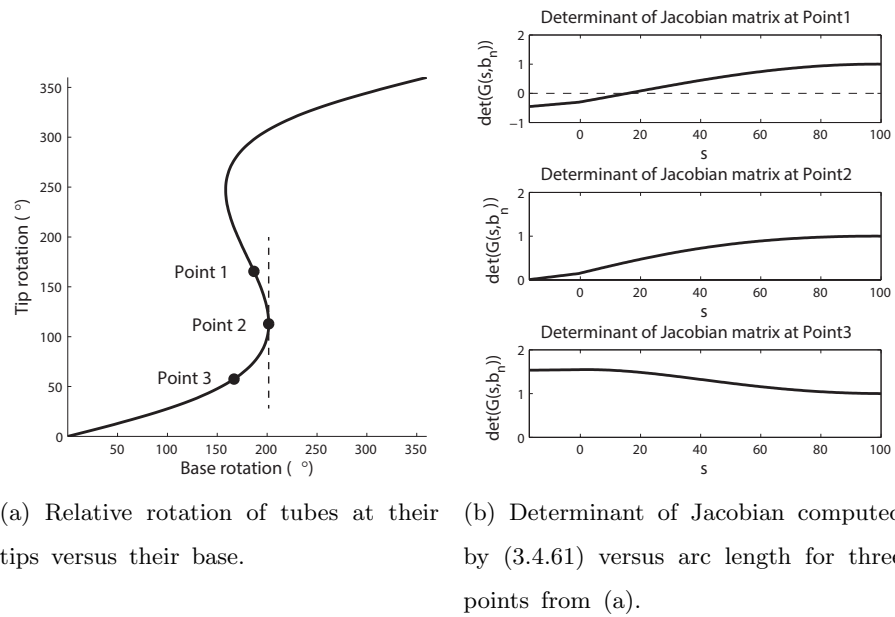


Figure 3.5: Comparison of relative rotation plot with stability criterion.

remains fixed in the world frame. Note that this is done purely for pedagogical reasons and is not a limitation of the proposed method.

By varying the fixation points of the springs,  $c_{f_e}(s)$  and  $c_{F_e}$ , it is possible to produce forces that either increase or decrease the curvature of the tube pair (Fig. 3.6(b)). These are given, respectively, by:

$$\text{Set 1} \begin{cases} f_e(p(s), s) = -k_{f_e}(p(s) - [0 \ 0 \ (a_n + s)/10]^T) \\ F_e(p(b_n), b_n) = -k_{F_e}(p(b_n) - [0 \ 0 \ b_n/10]^T), \end{cases} \quad (3.5.65)$$

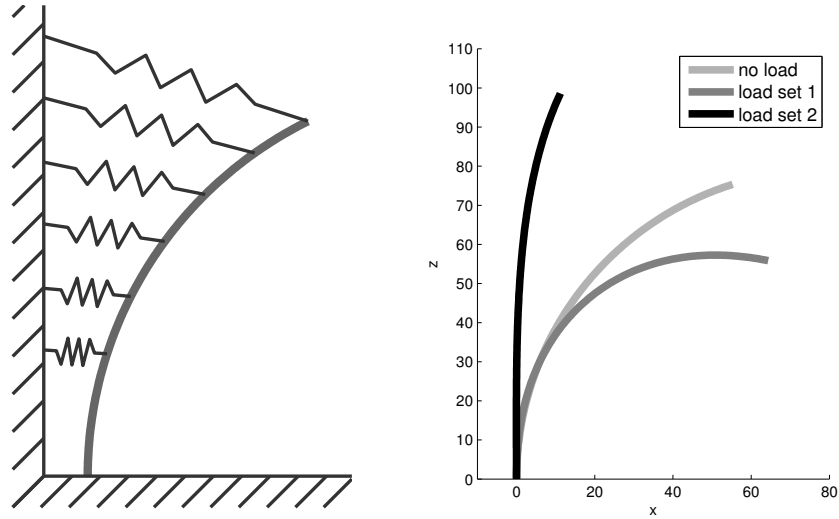
and

$$\text{Set 2} \begin{cases} f_e(p(s), s) = -k_{f_e}(p(s) - [0 \ 0 \ 2(a_n + s)]^T) \\ F_e(p(b_n), b_n) = -k_{F_e}(p(b_n) - [0 \ 0 \ 2b_n]^T). \end{cases} \quad (3.5.66)$$

The effect of these external loads on stability is compared with the unloaded case in Fig. 3.7 using the parameter values for Example 2 in Table 3.1. Force set 1, which increases the curvature, destabilizes the robot. This can be seen by the shape of the relative rotation curve in Fig. 3.7(a) as well as by the determinant plot in Fig. 3.7(b). Force set 2, in contrast, reduces robot curvature and, in so doing, stabilizes the robot.

### 3.5.3 Example 3: Stability of a Constant-precvature Tube Pair Subject to Constant World-frame Loads

This example examines the general case of constant world-frame external loads without the constraint of the preceding example that the loads remain invariant to rotations of the tube set about its base. This general case is depicted in Fig. 3.8 where it can be seen that the effect of the loads depends not only on the relative angles of the tubes at the robot base, but also the actual tube base angles. To verify the local stability criteria for this case, a 3D plot is needed showing tip twist angle as a function of the two base rotation angles.



(a) Load schematic.

(b) Shape of robot at maximum curvature for no load, load set 1 and load set 2.

Figure 3.6: Elastic tip and distributed forces applied to a variable curvature tube pair.

Let  $(m, f) \in \mathbb{R}^3 \times \mathbb{R}^3$  and  $(M, F) \in \mathbb{R}^3 \times \mathbb{R}^3$  denote the constant distributed load and the constant tip load, respectively. Note that constant moments expressed in the world frame are generally non-conservative. This can be easily shown by computing the net work of a rigid body following an arbitrary closed motion of rotation with a constant moment expressed in the world frame. From (3.3.38) and

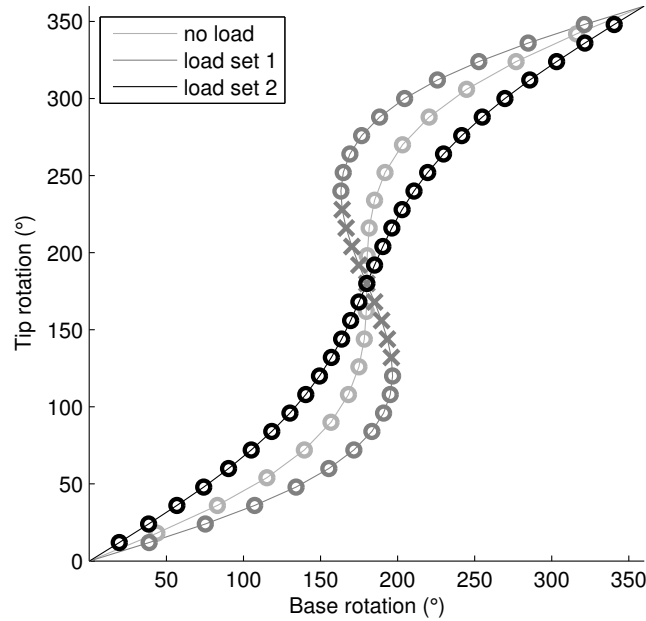


Figure 3.7: Relative rotation plots labeled using stability criterion for Example 2. Points on curve labeled stable (o) and unstable (x) using stability criterion.

(3.3.39), the generalized forces are given by

$$\begin{aligned}
 v_p(s) &= f, \quad V_P = F, \\
 v_R(s) &= \frac{1}{2}[m]R(s), \quad V_R = \frac{1}{2}[M]R(b_n), \\
 v_{\theta_1}(s) &= R(s)^T m|_z, \quad V_{\theta_1} = R(b_n)^T M|_z.
 \end{aligned} \tag{3.5.67}$$

For the parameter values given for Example 4 in Table 3.1, the 3D stability plot is shown in Fig. 3.9. This plot can be interpreted analogously to Fig. 3.4. The tubes are stable under the external load when the mapping from the two base angles to relative tip angle is unique. In the case of solution multiplicity, some solutions are unstable.

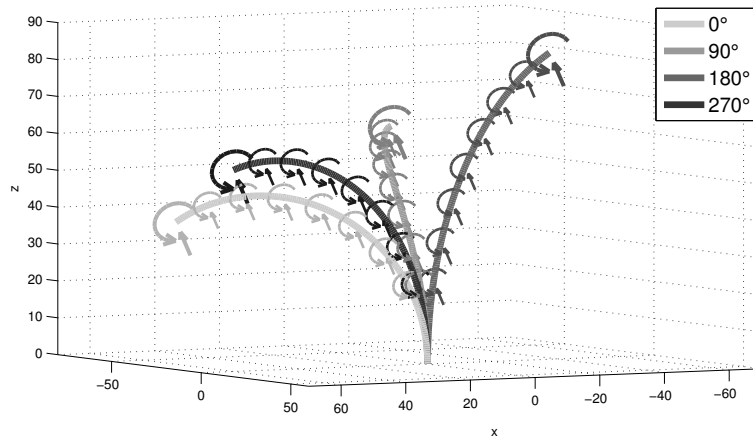


Figure 3.8: Effect of constant world-frame loads depends on both base tube angles.

The stability criteria was used to label a grid of points on the surface of Fig. 3.9. Unstable points are marked with a red ‘x’ and stable points are marked with a blue ‘o’. Note that the boundary between the regions of unstable and stable configurations consists of a curve on which the tangent planes are parallel to the vertical axis. This is consistent with the observation for the preceding 2D plots that the stability boundary corresponds to points of infinite slope.

#### 3.5.4 Example 4: Application to Stable Path Planning

To illustrate use of the stability criterion, an example of stable path planning using the RRT algorithm is presented here. A three-tube robot design, shown in Fig. 3.10, is employed using parameters in Table 3.2.

To enable easy interpretation of results, external loads, which have been covered thoroughly in the preceding examples, are not included here. Furthermore, while the three tubes possess a total of 6 degrees of freedom, only three kinematic

Table 3.2: Example 4 parameters. Note that  $(a_3, b_3)$  vary with translation length of the innermost tube.

	<b>Tube 1</b>	<b>Tube 2</b>		<b>Tube 3</b>	
	Section 1	Section 1	Section 2	Section 1	Section 2
Length (mm)	100	17	150	184	100
Curvature ( $\text{mm}^{-1}$ )	1/120	0.0	1/120	0.0	1/60
Bending Stiffness	1	1	1	0.5	0.5
Torsional Stiffness	1/1.3	1/1.3	1/1.3	0.5/1.3	0.5/1.3
$a_i$ (mm)	0	-17		$-134 \sim -34$	
$b_i$ (mm)	100	150		$150 \sim 250$	
Initial conf.	$(\theta_2(b_3), \theta_3(b_3), b_3) = (360^\circ, 0^\circ, 170\text{mm})$				
Goal conf.	$(\theta_2(b_3), \theta_3(b_3), b_3) = (200^\circ, 200^\circ, 170\text{mm})$				

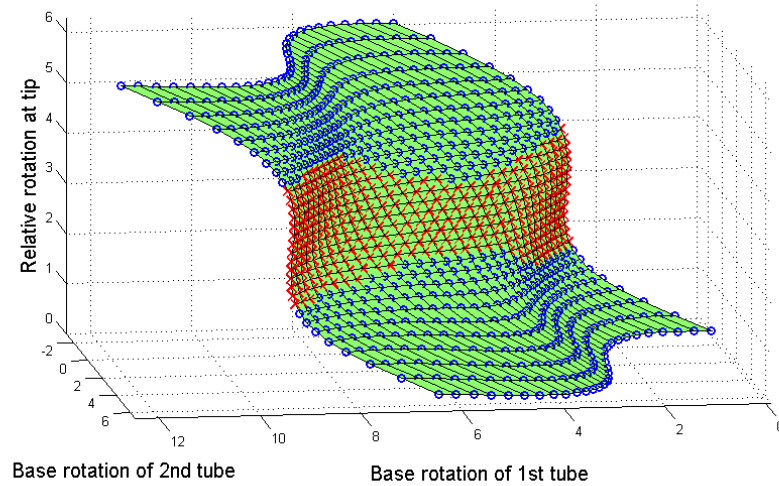


Figure 3.9: Multi-dimensional s-curve. The red ‘x’ markers denote unstable configurations, and the blue ‘o’ markers denote stable configurations.

inputs are considered so that results can be viewed as a 3D plot. The kinematic inputs are comprised of rotation of the middle tube as well as translation and rotation of the innermost tube.

Instability can occur in this tube set when the innermost tube is rotated while retracted inside the outer two tubes. To evaluate whether or not path planning using the stability criterion can be used to avoid the unstable configurations, the initial and goal configurations of the robot are defined as shown in Fig. 3.11 and given in Table 3.2.

Normally, path planning involves solving for a robot path that avoids collisions with obstacles. To plan a stable path, we define here a ‘collision function’ for detecting instability. The final path from RRT after smoothing, however, tends to

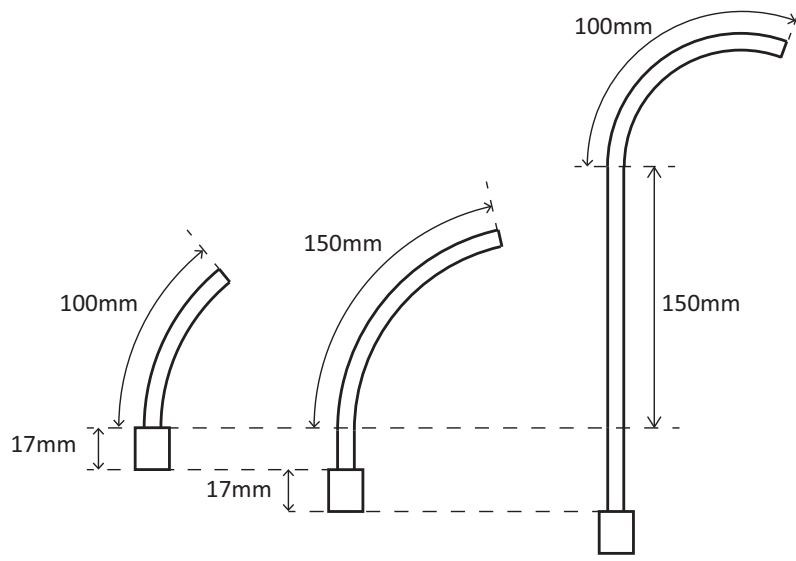


Figure 3.10: Tubes comprising robot of Example 4.

slide over the surfaces of obstacles. For ensuring stability, this is not a safe approach since it corresponds to operating on the border of instability. We would like to enforce a stability margin, equivalent to a minimum safe distance from obstacles. This is easily accomplished by enforcing an inequality constraint on  $\det(X(s))$  from (3.4.61):

$$\det(X(s)) > \epsilon \quad (3.5.68)$$

where  $\epsilon \in \mathbb{R}$  defines the desired stability margin. This approach is used in the collision function defined in Table 3.3.

Fig. 3.12 depicts the trees and paths generated by the RRT algorithm for stability margin values of  $\epsilon = \{0, 0.9\}$ . The red curves are the final paths before smoothing, and the green ones are after smoothing. The colored volumes represent the unstable regions. Each color represents the minimum value of  $\det(X(s))$  over the length  $s \in [a_n, b_n]$ . The minimum values of  $\det(X(s))$  in the red regions

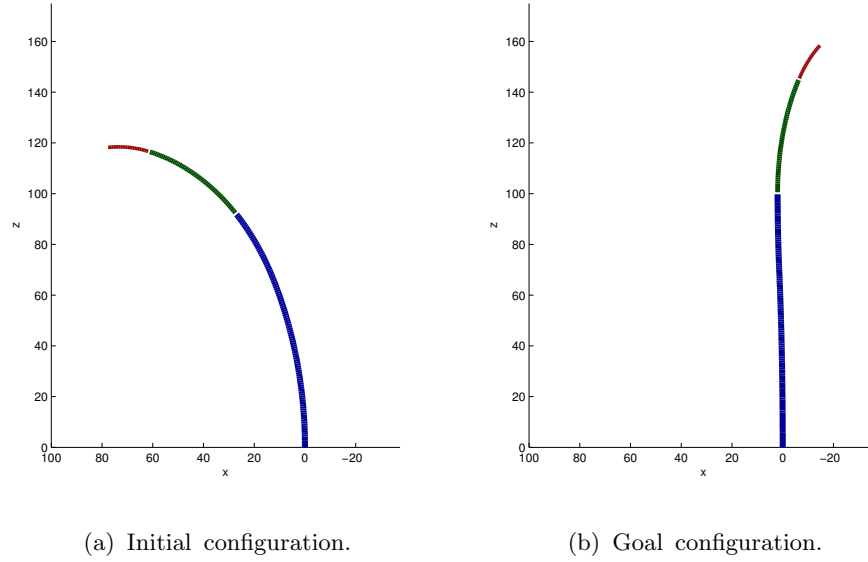


Figure 3.11: Initial and goal configurations for stable path planning.

Table 3.3: Collision Function

---

**COLLISION\_CHECK** $(x^*, \lambda^*, u^*, \epsilon)$

---

- 1** Compute  $X(s)$  over  $s \in [a_n, b_n]$  for the given stationary solution  $(x^*, \lambda^*, u^*)$ , using Equation (3.4.51).
  - 2** If  $\det(X(s)) > \epsilon$  for  $s \in [a_n, b_n]$ ,  
     return **false**.  
   Else,  
     return **true**.
- 

are more negative than those in the blue regions. The corresponding motions of the tubes are shown in Fig. 3.13.

As expected, the direct path between the initial and goal configurations leads through the unstable region. The RRT algorithm has solved for paths in which the innermost tube is first extended and then rotated before being retracted again. Notice in Fig. 3.12 that, for  $\epsilon = 0$ , the smoothed green path follows the boundary of the unstable region. When a stability margin is imposed with  $\epsilon = 0.9$ , however, the smoothed path moves away from the stability boundary to create a condition of robust stability. Physically, increased stability is achieved through greater extension of the innermost tube as shown in Fig. 3.13.

## APPENDIX: Derivation of Jacobian Matrix

In the presence of conservative and non-conservative external loads, the kinematics of the concentric tube robot are given by

$$\dot{x} = \frac{\partial H}{\partial \lambda}, \quad \dot{\lambda} = -\frac{\partial H}{\partial x} + v, \quad \frac{\partial H}{\partial u} = 0 \quad (3.5.69)$$

with the boundary condition

$$\lambda(b_n) = \frac{\partial W}{\partial x} - V. \quad (3.5.70)$$

Noting that  $f(x, u)$  is given by  $f(x, u) = \partial H / \partial \lambda$ , linearizing the kinematic equations and the boundary condition yields a set of linear ODEs

$$\delta \dot{x} = \frac{\partial f}{\partial x} \delta x + \frac{\partial f}{\partial u} \delta u \quad (3.5.71)$$

$$\delta \dot{\lambda} = -\frac{\partial^2 H}{\partial x^2} \delta x - \frac{\partial f^T}{\partial x} \delta \lambda - \frac{\partial^2 H}{\partial x \partial u} \delta u + \frac{\partial v}{\partial x} \delta x \quad (3.5.72)$$

$$\frac{\partial^2 H}{\partial u \partial x} \delta x + \frac{\partial f^T}{\partial u} \delta \lambda + \frac{\partial^2 H}{\partial u^2} \delta u = 0 \quad (3.5.73)$$

and a boundary condition

$$\delta \lambda(b_n) = \frac{\partial^2 W}{\partial x^2} \delta x(b_n) - \frac{\partial V}{\partial x} \delta x(b_n). \quad (3.5.74)$$

From Equation (3.5.73),  $\delta u$  is given by

$$\delta u = -\frac{\partial^2 H^{-1}}{\partial u^2} \frac{\partial^2 H}{\partial u \partial x} \delta x - \frac{\partial^2 H^{-1}}{\partial u^2} \frac{\partial f^T}{\partial u} \delta \lambda, \quad (3.5.75)$$

and substituting Equation (3.5.75) into (3.5.71)-(3.5.72) yields

$$\begin{bmatrix} \dot{\delta x} \\ \dot{\delta \lambda} \end{bmatrix} = \begin{bmatrix} P_1 & -P_2 \\ -P_0 & P_1^T \end{bmatrix} \begin{bmatrix} \delta x \\ \delta \lambda \end{bmatrix} \quad (3.5.76)$$

where

$$\begin{aligned} P_0 &= \frac{\partial^2 H}{\partial x^2} - \frac{\partial^2 H}{\partial x \partial u} \frac{\partial^2 H^{-1}}{\partial u^2} \frac{\partial^2 H}{\partial u \partial x} - \frac{\partial v}{\partial x} \\ P_1 &= \frac{\partial f}{\partial x} - \frac{\partial f}{\partial u} \frac{\partial^2 H^{-1}}{\partial u^2} \frac{\partial^2 H}{\partial u \partial x} \\ P_2 &= \frac{\partial f}{\partial u} \frac{\partial^2 H^{-1}}{\partial u^2} \frac{\partial f^T}{\partial u}. \end{aligned} \quad (3.5.77)$$

Let  $\Theta(s)$  denote the state transition matrix of the linear ODE given by (3.5.77), which satisfies

$$\begin{bmatrix} \delta x(s) \\ \delta \lambda(s) \end{bmatrix} = \Theta(s) \begin{bmatrix} \delta x(b_n) \\ \delta \lambda(b_n) \end{bmatrix}. \quad (3.5.78)$$

Note that  $\Theta(s)$  can be computed by a IVP

$$\dot{\Theta} = P\Theta, \quad \Theta(b_n) = I. \quad (3.5.79)$$

Partitioning  $\Theta$  as

$$\Theta = \begin{bmatrix} \Theta_{xx} & \Theta_{x\lambda} \\ \Theta_{\lambda x} & \Theta_{\lambda\lambda} \end{bmatrix}, \quad (3.5.80)$$

the variation  $\delta x(s)$  is given by

$$\delta x(s) = \Theta_{xx}(s) \delta x(b_n) + \Theta_{x\lambda}(s) \delta \lambda(b_n). \quad (3.5.81)$$

Substituting (3.5.74) into (3.5.81),  $\delta\lambda(b_n)$  is eliminated, and the right side of (3.5.81) becomes linear in  $\delta x(b_n)$ :

$$\delta x(s) = G(s, b_n)\delta x(b_n) \quad (3.5.82)$$

where  $G(s, b_n)$  is the Jacobian matrix, given by

$$G(s, b_n) = \left( \Theta_{xx}(s) + \Theta_{x\lambda}(s) \left( \frac{\partial^2 W}{\partial x^2} - \frac{\partial V}{\partial x} \delta x(b_n) \right) \right). \quad (3.5.83)$$

This matrix is equivalent to  $X(s)$  in (3.4.61) in the presence of non-conservative external loads, and to  $X(s)$  in (3.4.51) when there is no non-conservative external load, i.e.,  $v = 0$  and  $V = 0$ .

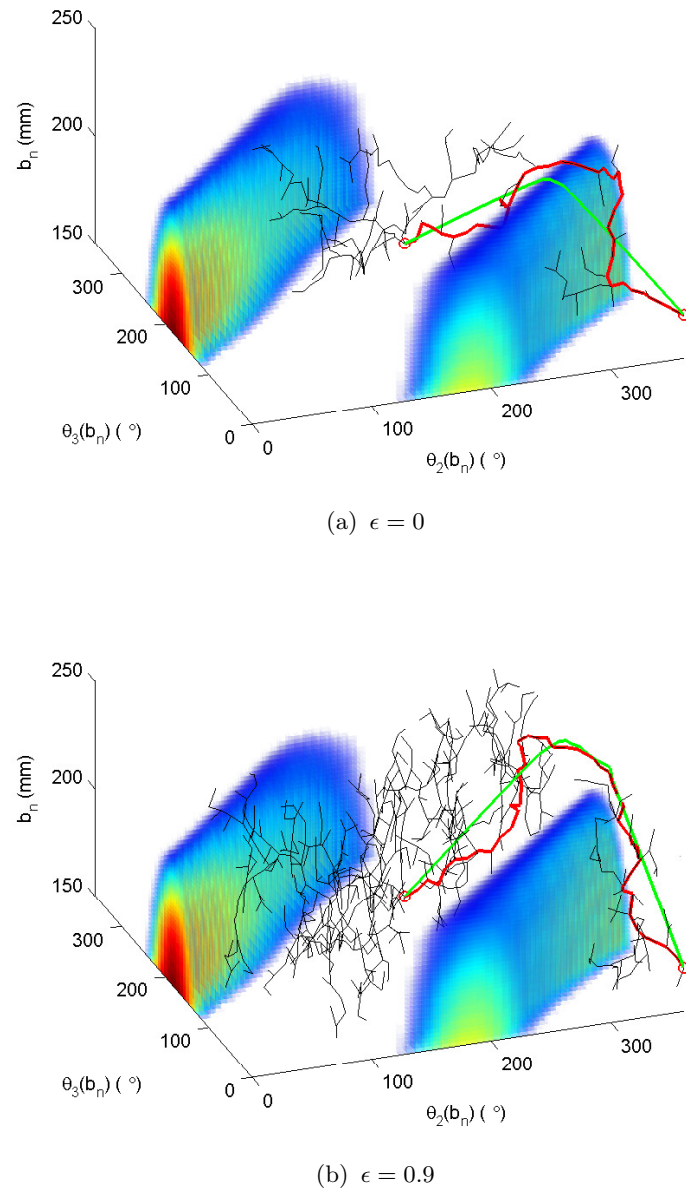


Figure 3.12: Configuration space maps showing paths and trees generated by RRT for  $\epsilon = \{0, 0.9\}$ . Red and green curves are the final paths before and after smoothing, respectively. Colored volumes represent unstable regions.

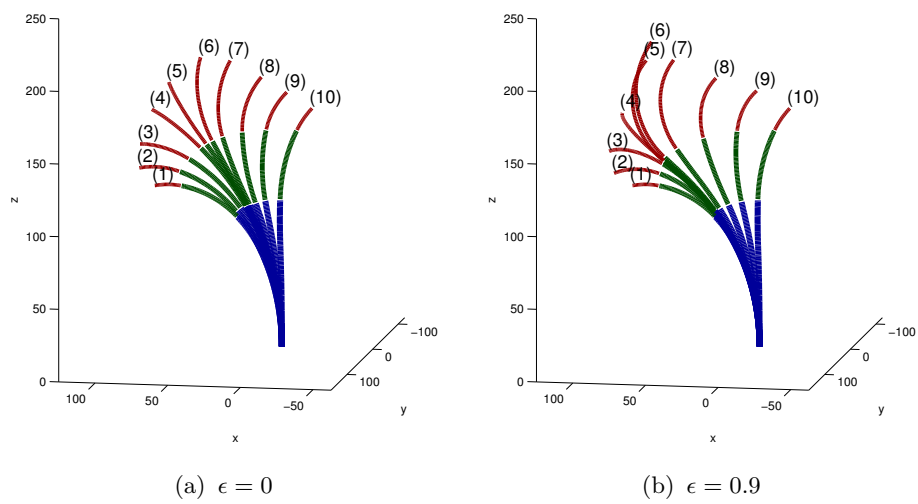


Figure 3.13: Final smoothed stable paths for  $\epsilon = \{0, 0.9\}$ . Numbers indicate sequence of configurations along paths.



# 4

## Optimizing Curvature Sensor Placement for Shape Sensing

### 4.1 Introduction

Many approaches to robot control involve solving the forward kinematics problem in real time as a means to compute the desired twist (velocity) vector for the tip coordinate frame. For robots comprised of links and discrete joints, the kinematic model is composed of algebraic equations and is trivial to compute. Continuum robots, however, that obtain their shape through flexure of their structural components, often require more complex mechanics-based models [1], [30], [31] and [26].

For example, the kinematics of concentric tube robots are modeled by a boundary value problem [1], [26]. These models can be difficult to compute in real time. Furthermore, continuum robots flex when they apply forces to their environment. Accounting for this flexure adds even more complexity to the model [30], [26], [25]

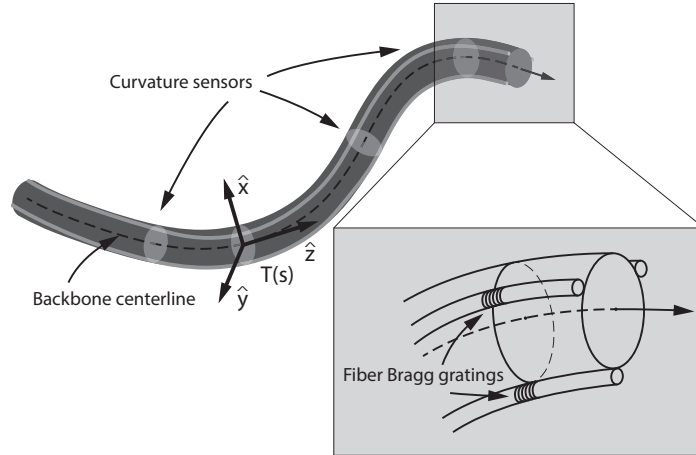


Figure 4.1: Fiber Bragg Gratings used as curvature sensors along the length of a continuum robot.

and, in addition, sensing is needed to measure flexion.

Approaches to measuring the shape of a continuum robot include image-based methods [32],[33], electromagnetic tracking [34] and force sensing in control tendons [30]. While each of these approaches can be useful in certain circumstances, they can also pose challenges. For example, image-based methods can be computationally intensive leading to low update rates. Electromagnetic tracking is subject to magnetic field distortions and often only provides robot tip location and not robot shape. Tendon force sensing is corrupted by tendon sliding friction and also does not provide local shape information.

An alternative approach used to measure needle deflection [35], [36] and also recently for continuum robot shape estimation [37] is to use optical fibers with fiber Bragg gratings (FBG's). By arranging multiple fibers (typically three or four) around the circumference of a cylinder at fixed distance from the neutral axis of

bending, the strain-induced frequency shift in a set of FBG's can be used to compute the  $x$  and  $y$  curvature of a cross section. This is shown in Fig. 4.1. By including multiple FBG's along the length of a fiber, each possessing its own center frequency, the curvature at a discrete set of points along the length of a curved tubular object can be measured. The estimated shape of the object's centerline as well as its tip location can be reconstructed by integrating these curvature measurements using a model describing how curvature varies between sensors.

In prior work, sensors are placed uniformly along the length and use the  $k$ -nearest neighbor interpolation model [35] to reconstruct the curvature functions or use a second order polynomial model for curvature functions and solve for the coefficients from the boundary conditions using one-dimensional beam theory [36].

FBG's represent a promising alternative for continuum robot shape sensing and the cost of optical interrogators used to measure frequency shift has decreased considerably in recent years. In order to provide a basis of comparison between this technology and the alternate approaches described earlier, however, several important issues need be addressed. These include characterizing the dependence of centerline and tip frame error on the reconstruction model used as well as on the number of sensors and their location along the length of the robot.

The contributions of this paper are to provide a framework for addressing this problem, to propose several types of reconstruction models and to illustrate the use of these models in the context of concentric tube robots. The paper is arranged as follows. The next section introduces the general framework for optimizing sensor locations and proposes three reconstruction models parameterized by a set of curvature measurements. Section 4.3 applies this framework and the proposed reconstruction models to concentric tube robot kinematics. Numerical examples are presented in Section 4.4 and conclusions appear in final section.

## 4.2 Shape Estimation for Continuum Robots

We begin this section with a brief review of the single backbone curve model for describing the kinematics of a general continuum robot. We then discuss shape reconstruction models, and show how optimal sensor locations can be determined via an optimization problem that minimizes the shape and tip errors between the reconstruction model and a mechanics-based model. In this section we adopt the notation  $SE(3)$  to denote the special Euclidean group of rigid body motions (or homogeneous transformations), and  $se(3)$  to denote its Lie algebra (see, e.g., [38]).

### 4.2.1 Kinematics of Continuum Robots

The continuum robots considered in this paper can be modeled by an arclength parametrized curve in three-dimensional space, referred to as the backbone curve. Letting  $s$  denote the arclength parameter, a right-handed reference frame  $T(s) \in SE(3)$  is then attached to each point of the backbone curve in such a way that (i) the  $z$ -axis is always tangent to the backbone curve, and (ii) no rotations about the  $z$ -axis (or backbone curve) are permitted. A reference frame defined in this way is referred to as a Bishop frame [24]. Taking the left-invariant derivative of  $T(s)$  with respect to  $s$ , we obtain

$$[V(s)] = T^{-1} \frac{dT}{ds} = \begin{pmatrix} [u(s)] & \nu \\ 0 & 0 \end{pmatrix} \in se(3), \quad (4.2.1)$$

where  $u(s)$  is given by

$$u(s) = \begin{pmatrix} u_x(s) & u_y(s) & 0 \end{pmatrix}^T \in \mathbb{R}^3. \quad (4.2.2)$$

The curve  $u(s) \in \mathbb{R}^3$  denotes the angular velocity of the frame  $T(s)$  per unit arclength, while  $\nu \in \mathbb{R}^3$  denotes the linear velocity of the origin of  $T(s)$  per unit

arclength; for the Bishop frame as defined, the  $z$ -component of  $u(s)$  is zero, and  $\nu = (0 \ 0 \ 1)^T \in \mathbb{R}^3$ . Various mechanics-based models have been developed for continuum robots [1]-[26] from which curvatures can be extracted via Equation (4.2.2), which can then be used as a benchmark for evaluating alternative models for shape sensing.

### 4.2.2 Shape Reconstruction Models

The estimation of shape begins with the reconstruction of the curvature function  $\tilde{u}(s)$  defined along the backbone curve (the tilde is used to denote functions defined in terms of the reconstruction model). The coordinate frames  $\tilde{T}(s)$  are obtained by integrating Eq. (4.2.1). The shape of the robot  $\tilde{p}(s)$  can then be obtained by taking the position vector of  $\tilde{T}(s)$ . The tip configuration is also obtained by taking the value of  $\tilde{T}(s)$  at  $L$  as  $\tilde{T}(L) \in SE(3)$ .

#### 4.2.2.1 Piecewise Constant Curvature Model

Given  $p$  sensors with respective locations  $s_k \in \mathbb{R}, i = 1, \dots, p$ , the simplest reconstruction method assumes that the curvature between sensors is constant; this implies that the function  $\tilde{u}(s)$  is of the form

$$\tilde{u}(s) = u^k = \begin{pmatrix} u_x^k & u_y^k & 0 \end{pmatrix}^T \quad (4.2.3)$$

for  $\beta s_{k-1} + (1 - \beta)s_k \leq s < \beta s_k + (1 - \beta)s_{k+1}$ , where  $u_x^k$  and  $u_y^k \in \mathbb{R}$  respectively denote the bending curvature sensor values at sensor location  $s_k$  in the  $x$  and  $y$  directions. The constant scalar  $\beta \in [0, 1]$  controls how the intervals are spaced around the sensor locations: if  $\beta = 0$ , the sensor covers the interval from its current location to the next sensor, whereas if  $\beta = 1$ , the sensor covers the interval from

the previous sensor location to its current location. The backbone coordinate frame  $\tilde{T}(s)$  is computed as follows when  $\beta$  is set to 0:

$$\tilde{T}(s) = T_0 e^{[V_{s_0}](s_1-s_0)} e^{[V_{s_1}](s_2-s_1)} \dots e^{[V_{s_k}](s-s_k)} \quad (4.2.4)$$

The term  $[V_{s_k}] \in se(3)$  is given by

$$[V_{s_k}] = \begin{pmatrix} [u^k] & \nu \\ 000 & 0 \end{pmatrix}. \quad (4.2.5)$$

#### 4.2.2.2 Basis Function Model

The shape reconstruction models introduced in this paper are based on the assumption that the curvature functions  $u(s)$  can be reconstructed as a linear combination of a certain set of basis functions. Consider that the  $x$  and  $y$  components of  $\tilde{u}(s)$  are given in the form

$$\tilde{u}_x(s) = \sum_{j=1}^q c_x^j B_x^j(s) \quad (4.2.6)$$

$$\tilde{u}_y(s) = \sum_{j=1}^q c_y^j B_y^j(s) \quad (4.2.7)$$

where  $B_x^j(s)$  and  $B_y^j(s) \in \mathbb{R}$  respectively denote basis functions in the  $x$  and  $y$  directions,  $c_x^j$  and  $c_y^j \in \mathbb{R}$  are the corresponding coefficients for the  $x$  and  $y$  components, and  $q$  denotes the total number of basis functions. Assume that the basis functions  $B_x^j(s)$ ,  $j = 1, \dots, q$  in Eq. (4.2.6) are given. To determine the coefficients  $c_x^j$ ,  $j = 1, \dots, q$ , we can use the sensor measurements at the arclength location  $s_k$ ,  $k = 1, \dots, p$ . Let  $f_k \in \mathbb{R}$  be a scalar-valued function associated with the  $k$ -th sensor location, defined as the difference between the curvature value  $\tilde{u}_x(s_k)$  computed from a reconstruction model and the sensor measurement  $u_x^k$ :

$$f_x^k = \tilde{u}_x(s_k) - u_x^k = \sum_{j=1}^q c_x^j B_x^j(s_k) - u_x^k \quad (4.2.8)$$

The  $c_x^j$  can be expressed as minimizers to the least-squares criterion involving  $f_k$ :

$$\{c_x^1, \dots, c_x^q\} = \arg \min_{c_x^1, \dots, c_x^q} \sum_{k=1}^p f_x^k{}^2. \quad (4.2.9)$$

The above can be rewritten in matrix form as

$$\bar{c}_x = \arg \min_{\bar{c}_x} \|B_x \bar{c}_x - \bar{u}_x\|^2, \quad (4.2.10)$$

where  $B_x \in \mathbb{R}^{p \times q}$ ,  $\bar{c}_x \in \mathbb{R}^q$  and  $\bar{u}_x \in \mathbb{R}^p$  are given by

$$B_x = \begin{pmatrix} B_x^1(s_1) & B_x^2(s_1) & \cdots & B_x^q(s_1) \\ B_x^1(s_2) & B_x^2(s_2) & & B_x^q(s_2) \\ \vdots & & \ddots & \vdots \\ B_x^1(s_p) & B_x^2(s_p) & & B_x^q(s_p) \end{pmatrix} \quad (4.2.11)$$

$$\bar{c}_x = \begin{pmatrix} c_x^1 & c_x^2 & \cdots & c_x^q \end{pmatrix}^T \quad (4.2.12)$$

$$\bar{u}_x = \begin{pmatrix} u_x^1 & u_x^2 & \cdots & u_x^p \end{pmatrix}^T \quad (4.2.13)$$

The generalized inverse  $B_x^\dagger$  of  $B_x$  can be used to compute the augmented coefficient vector  $\bar{c}_x$  as follows:

$$\bar{c}_x = B_x^\dagger \bar{u}_x \quad (4.2.14)$$

In general, if  $p = q$ , a unique solution  $\bar{c}_x$  can be obtained as

$$\bar{c}_x = B_x^{-1} \bar{u}_x. \quad (4.2.15)$$

This results in  $f_x^k = 0$  for all  $k = 1, \dots, p$ , in which case the reconstruction model reduces to an **interpolation** model. If on the other hand  $p > q$ , then Eq. (4.2.14) leads to the least squares sum of  $f_k$ , in which case the reconstruction model reduces to a **regression** model. Having the number of sensors  $p$  be smaller than the number of bases  $q$  is clearly undesirable. If  $p < q$ , the solution to Eq. (4.2.10) is not

uniquely determined, and the reconstructed shape tends to deviate in undesirable ways. The same procedure (4.2.8)~(4.2.15) can be applied to the  $y$ -component of  $\tilde{u}(s)$  in Eq. (4.2.7).

Without any knowledge of the mechanics for the target continuum robot, choosing a suitable basis function to efficiently approximate the shape becomes difficult. Popular choices for the basis function include the polynomial basis

$$B_x^j(s) = s^{j-1}, \quad j = 1, \dots, q, \quad (4.2.16)$$

as well as the Fourier series basis

$$B_x^j(s) = e^{i\frac{2\pi js}{L}}, \quad j = -q, \dots, q. \quad (4.2.17)$$

### 4.2.3 Optimal Sensor Location

Given  $p$  sensors and a reconstruction model  $\tilde{u}(\cdot)$ , the sensor locations can be determined as the solution to the following optimization problem:

$$\min_{s_k} w_1 J_1 + w_2 J_2, \quad k = 1, \dots, p, \quad (4.2.18)$$

where  $J_1$  and  $J_2$  denote the errors of the shape and tip configurations, respectively, and  $w_1$  and  $w_2$  denote the corresponding weight coefficients. Assume that we have  $M$  workspace samples, and denote the kinematic input variables corresponding to the  $l$ -th work space sample by  $\xi_l$ . Let  $u(s, \xi_l)$  and  $p(s, \xi_l)$  denote the corresponding kinematic curvature and backbone centerline solutions for  $\xi_l$  as determined from a mechanics-based model. The shape error function  $J_1$  can then be defined with respect to either the curvature or the backbone centerline as follows:

$$J_1 = \sum_{l=1}^M \frac{1}{L} \int_0^L \|u(s, \xi_l) - \tilde{u}(s, \xi_l)\| ds \quad (4.2.19)$$

$$J_1 = \sum_{l=1}^M \frac{1}{L} \int_0^L \|p(s, \xi_l) - \tilde{p}(s, \xi_l)\| ds. \quad (4.2.20)$$

Note that  $u(s, \xi_l)$  and  $p(s, \xi_l)$  can be computed from the appropriate mechanics-based kinematic model for all the workspace samples, while  $\tilde{u}(s, \xi_l)$  and  $\tilde{p}(s, \xi_l)$  are obtained from the chosen reconstruction model. The tip configuration error  $J_2$  over the  $M$  workspace samples can then be defined as

$$J_2 = \sum_{l=1}^M d_t(T(L, \xi_l), \tilde{T}(L, \xi_l)), \quad (4.2.21)$$

where  $d_t : SE(3) \times SE(3) \rightarrow \mathbb{R}$  denotes a suitable distance metric between a mechanics-based solution of the tip configuration  $T(L)$  and one obtained from the reconstruction model  $\tilde{T}(L)$ . One popular choice for  $d_t(\cdot, \cdot)$  is given by the scaled square sum of the position and orientation errors:

$$d_t(T_1, T_2) = \|p_1 - p_2\|^2 + \gamma \|\log(R_1^T R_2)\|^2, \quad (4.2.22)$$

where  $p_i \in \mathbb{R}^3$  and  $R_i \in SO(3)$ ,  $i = 1, 2$  denote the position and orientation components of  $T_i \in SE(3)$ , and  $\gamma > 0$  is a positive scalar that determines the relative weight between the position and orientation errors (or equivalently, represents a choice of length scale for physical space).

The objective function defined in (4.2.18) represent the averaged error over the workspace samples. The minimizer to (4.2.18) can provide the minimum averaged error, however, it does not guarantee to minimize the maximum error over the workspace samples. If one wants the maximum tip position error over the workspace to be minimized, one can consider an alternative optimization formula given by

$$\min_{s_k} \left( \max_l d_t(T(L, \xi_l), \tilde{T}(L, \xi_l)) \right). \quad (4.2.23)$$

Similar formula can be applied to the maximum curvature or position shape error.

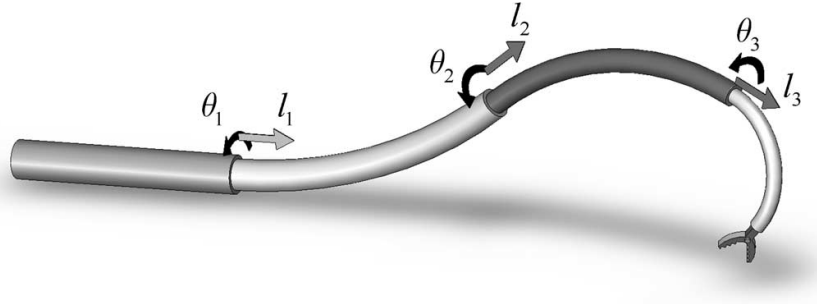


Figure 4.2: Concentric tube robot consisting of four telescoping sections that can be rotated and translated with respect to each other.

### 4.3 Case Study: Concentric Tube Robots

Concentric tube robots have recently received considerable attention as a new medical instrument for minimally invasive medical procedures. They are composed of pre-curved elastic tubes that are concentrically arranged. An example of a concentric tube robot is shown in Fig. 4.2. In this example, the concentric tube robot consists of four telescoping sections that can be rotated and translated with respect to each other. In this section, the proposed shape estimation framework is applied to concentric tube robots. It is assumed that the shape sensors are attached to a sensing tube or rod located inside the innermost robot tube that translates with this robot tube. It is also assumed that the sensing tube is very flexible in bending, but is torsionally stiff so that it bends, but does not twist with the innermost robot tube.

### 4.3.1 Kinematics of Concentric Tube Robots

For the shape computation of a concentric tube robot, the rotated angle  $\theta_i(s) \in \mathbb{R}$  and the three-component curvature vector  $u_i(s) = (u_{ix}(s) \ u_{iy}(s) \ u_{iz}(s))^T \in \mathbb{R}^3$  for every  $i$ -th tube need to be computed along the arclength parameter  $s$ . The mechanics-based kinematic equations for a general concentric tube robot with  $n$  tubes are derived in [1]; these are of the form

$$\begin{aligned} \frac{d\alpha_i}{ds} &= u_{iz} - u_{1z}, \quad i = 2, \dots, n \\ u_{1z} &= (-1/k_{1z})(k_{2z}u_{2z} + \dots + k_{nz}u_{nz}) \\ \frac{du_{iz}}{ds} &= (k_{ixy}/k_{iz})(u_{ix}\hat{u}_{iy} - u_{iy}\hat{u}_{ix}) \\ u_i|_{x,y} &= \left( \left( \sum_{j=1}^n K_j \right)^{-1} R_z^T(\alpha_i) \left( \sum_{j=1}^n R_z(\alpha_j) K_j \hat{u}_j \right) \right) \Big|_{x,y} \end{aligned} \quad (4.3.24)$$

where the relative twist angle  $\alpha_i \in \mathbb{R}$  is defined by  $\alpha_i = \theta_i - \theta_1$ .  $\hat{u}_i = (\hat{u}_{ix} \ \hat{u}_{iy} \ \hat{u}_{iz})^T \in \mathbb{R}^3$  and  $K_i \in \mathbb{R}^{3 \times 3}$  denote the pre-curvature vector and the frame-invariant stiffness tensor of  $i$ -th tube, respectively, while  $k_{ixy} \in \mathbb{R}$  and  $k_{iz} \in \mathbb{R}$  are the diagonal components of  $K_i$ . The kinematic inputs are the insertion distances  $L_i$  and the initial relative twist angles  $\theta_i(0)$  for every  $i$ -th tube. The shape of the concentric tube robot can be computed by solving the above boundary value problem for the following given boundary conditions:

$$\alpha_i(0) = \theta_i(0) - \theta_1(0), \quad i = 2, \dots, n \quad (4.3.25)$$

$$u_{iz}(L_i) = 0, \quad i = 2, \dots, n, \quad (4.3.26)$$

which are obtained from the kinematic input variables  $L_i$  and  $\theta_i(0)$ .

Assume that the curvature functions  $u_i(s), i = 1, \dots, n$  are given from the above split boundary value problem. Since we define the shape of a continuum

robot in terms of the Bishop frame attached at each point along the backbone curve, the untwisted curvature function  $u(s)$  needs to be computed. Consider the curvature function  $u_n(s)$  described with respect to the material coordinate frame attached to the  $n$ -th tube; by rotating  $u_n(s)$  along the  $z$ -axis by the amount of its twisted angle  $\theta_n(s)$ , the  $x$  and  $y$  components of  $u(s)$  can be obtained as follows:

$$\theta_n(s) = \int_0^s u_{nz}(\sigma) d\sigma \quad (4.3.27)$$

$$u(s)|_{x,y} = R_z(\theta_n(s)) u_n(s)|_{x,y} \quad (4.3.28)$$

$$u(s)|_z = 0. \quad (4.3.29)$$

The kinematic solution for the bending curvatures  $u_{ix}(s)$ ,  $u_{iy}(s)$  in the final equation of (4.3.24) can be discontinuous along the arclength, at locations where each tube ends or the pre-curvature of each tube changes discontinuously. The pre-curved shape and insertion length of the tubes determine where these discontinuous points are located. Using these points of discontinuity, the total arclength can be divided into several curvature sections. This discontinuity in the curvature functions should be taken into account during shape estimation of the concentric tube robot. We next address section-based reconstruction models that allow for discontinuous bending curvatures at the boundary of each curvature section.

### 4.3.2 Section-Based Principal Component Analysis Model

In the previous section we have introduced various choices of bases for the curvature function. Assume that mechanics-based kinematic solutions are available at a large number,  $M$ , of workspace samples. Denote the kinematic input variables by  $\xi = \{\theta_i(0), L_i\}_{i=1,\dots,n}$  and the corresponding solutions over the  $M$  workspace samples by  $\{u_x(s, \xi_l), u_y(s, \xi_l)\}_{l=1,\dots,M}$  (the subscript  $l$  in  $\xi_l$  is used to denote the index of the workspace samples).

Since the length of each section as well as the total length varies with the kinematic input variable  $\xi$ , we define a new length parameter  $\hat{s} \in [0, 1]$  to denote the normalized section length. The normalized locations of the junctions will be fixed with this new length parameter. The reconstructed curvature functions  $\tilde{u}_x(\hat{s})$  and  $\tilde{u}_y(\hat{s})$  in the  $x$  and  $y$  directions, along the normalized length parameter  $\hat{s}$  with  $q$  bases, is given by

$$\tilde{u}_x(\hat{s}) = \sum_{j=1}^q c_x^j B_x^j(\hat{s}) \quad (4.3.30)$$

$$\tilde{u}_y(\hat{s}) = \sum_{j=1}^q c_y^j B_y^j(\hat{s}), \quad (4.3.31)$$

where the bases are assumed to be orthogonal:

$$\int_0^1 B_x^j(\hat{s}) B_x^{j'}(\hat{s}) d\hat{s} = \begin{cases} 1 & \text{if } j = j' \\ 0 & \text{else} \end{cases} \quad (4.3.32)$$

$$\int_0^1 B_y^j(\hat{s}) B_y^{j'}(\hat{s}) d\hat{s} = \begin{cases} 1 & \text{if } j = j' \\ 0 & \text{else.} \end{cases} \quad (4.3.33)$$

The reconstruction error for the  $x$ -curvature function over the normalized length parameter  $\hat{s}$  is defined by

$$J_x = \sum_{l=1}^M \int_0^1 \|u_x(\hat{s}, \xi_l) - \tilde{u}_x(\hat{s})\|^2 d\hat{s}. \quad (4.3.34)$$

Natural bases can be obtain by minimizing  $J_x$  with respect to the bases  $B_x^l(\hat{s})$ :

$$\{B_x^1(\hat{s}), \dots, B_x^q(\hat{s})\} = \arg \min_{B_x^l(\hat{s})} J_x. \quad (4.3.35)$$

Discretizing every function of  $\hat{s}$  in the minimization (4.3.35) reduces the problem to a vector space minimization corresponding to the well-known principal component analysis. In this case the  $r$ -dimensional discretized bases  $B_x = ( B_x^1 \ \dots \ B_x^q ) \in$

$\mathbb{R}^{r \times q}$  can be obtained from a singular value decomposition of the given data matrix  $U = ( u_x(\xi_1) \ \dots \ u_x(\xi_M) ) \in \mathbb{R}^{r \times M}$ . The same procedure can be applied for the bases of the  $y$ -curvature function.

A useful property of concentric tube robots is that the initial bending curvatures  $u_x(0)$  and  $u_y(0)$  can be computed from the kinematic inputs  $\theta_i(0)$  via the final equation of (4.3.24) and Eq. (4.3.28), without actually having to solve the boundary value problem. This provides us with an additional curvature value at the proximal end of the robot. Using the sensor measurements together with this model-based value, the reconstruction follows Eq. (4.2.14) with the bases obtained from principal component analysis.

### 4.3.3 Section-based Polynomial Regression Model

Since the robot has been divided into piecewise continuous curvature sections, the curvature function within each section is guaranteed to be continuous. The simplest bases for continuous functions are polynomials. From observation of the dominant principal components, we can conclude that it is sufficient to use up to quadratic terms as the bases for each section (the number of basis functions  $q$  is 3 for the polynomial bases in Eq. (4.2.16)):

$$\tilde{u}_x(s) = \begin{cases} c_x^1 & \text{for 1 sensor.} \\ c_x^1 + c_x^2 s & \text{for 2 sensors.} \\ c_x^1 + c_x^2 s + c_x^3 s^2 & \text{for 3 or more sensors.} \end{cases} \quad (4.3.36)$$

If a single curvature value is available within the section, the curvature is interpolated by a constant function within the section. If two curvature values are available within the given section, the curvature can be linearly interpolated. If more than two curvature values are available within a given section, the curvature can

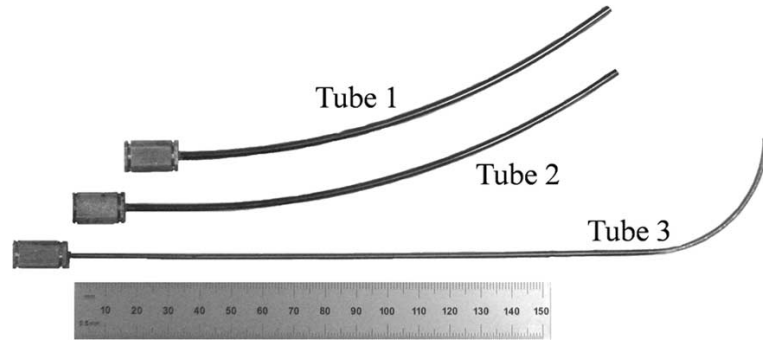


Figure 4.3: Three tubes comprising the concentric tube robot design used in the examples. Tubes 1 and 2 form a variable-curvature pair that are rotated with respect to each other to vary their composite curvature. Tube 3 can be arbitrarily rotated and extended and conforms to the curvature of the variable curvature pair when retracted.

be interpolated via Eq. (4.2.15), or regressed via Eq. (4.2.14) to a quadratic function. In the case of no sensor measurements on the given section, the interpolated or regressed function of an adjacent section can be used, although this will likely be inaccurate.

#### 4.4 Numerical Experiments for a Concentric Tube Robot

In this section we perform numerical experiments to determine how accurately the reconstruction models introduced in Sections 4.2 and 4.3 can determine the shape of a concentric tube robot. Consider the three-tube design shown in Fig. 4.3. The model parameters for each tube are given in Table 4.1. This design is described in detail in [1]. Tubes 1 and 2 are a balanced pair of tubes with fixed insertion lengths. The kinematic inputs for this robot are the initial rotated angles

Table 4.1: Concentric Tube Parameters

	<b>Tube 1</b>	<b>Tube 2</b>	<b>Tube 3</b>	
	Section 1	Section 1	Section 1	Section 2
Length (mm)	150	150	150	80
Curvature ( $\text{m}^{-1}$ )	4.525	4.525	0.0	16.667
Relative Stiffness	1	1	0.21	0.07

$\theta_i(0)_{i=1,2,3}$  of each tube, and the insertion length  $L_3$  of the innermost tube.

For this design, the centerline can be decomposed into three curvature sections by two locations of discontinuous curvature. The first discontinuity occurs at the distal tip of the variable curvature tube pair. The second discontinuity corresponds to the discontinuity in pre-curvature of Tube 3. This location lies in the interior of the variable curvature pair and varies with insertion length,  $L_3$ .

We fix the first sensor location at the distal end of the robot ( $s = L$ ). By doing that, we can always measure the curvature of the distal curvature section for the every extension length of Tube 3. For our specific concentric-tube robot, the distal curvature section has always a constant curvature determined by the twisted angle of Tube 3 at the distal.

The three reconstruction models compared here are the piecewise constant curvature model, the section-based PCA model, and the section-based polynomial regression model. For each reconstruction model, results are obtained for two sets of sensor locations: uniformly spaced sensor locations, and the optimized sensor locations obtained as a solution to the optimization problem (4.2.18).

To solve for the optimal sensor locations, we use the global optimization toolbox in MATLAB with the interior point algorithm for local search [39] and the scatter-search method for generating trial points [40].

#### 4.4.1 Selection of Basis Functions

Basis functions are needed for both the PCA-based model and the polynomial regression model. The PCA basis set can be selected using an eigenvalue analysis of the curvature functions over the workspace to obtain the principal component bases and their corresponding weights. In descending order of the weight values, the first five PC bases are chosen as the basis functions for the section-based PCA model.

As depicted in Fig. 4.4, the curvature basis functions for  $u_x(\hat{s})$  and  $u_y(\hat{s})$  can be interpreted geometrically. In particular, the most dominant principal component reproduces the constant pre-curvature of the distal portion of Tube 3. The second most dominant component represents Tubes 1 and 2 as constant in curvature over their length. The third basis elements predominantly model the approximately constant curvature corresponding to the portion of Tube 3 that is retracted into Tubes 1 and 2. The fourth basis elements model the variation from constant curvature of Tubes 1 and 2 as predicted by the mechanics model. The fifth basis elements predominantly model variation in curvature of the portion of Tube 3 that is retracted into Tubes 1 and 2.

Selection of basis functions for the section-based polynomial regression model involves choosing the appropriate order of the polynomial. Using the PCA bases as a guide, second order polynomial functions should be sufficient. Thus, the bases described in Section 4.3.3 are appropriate for each curvature section.

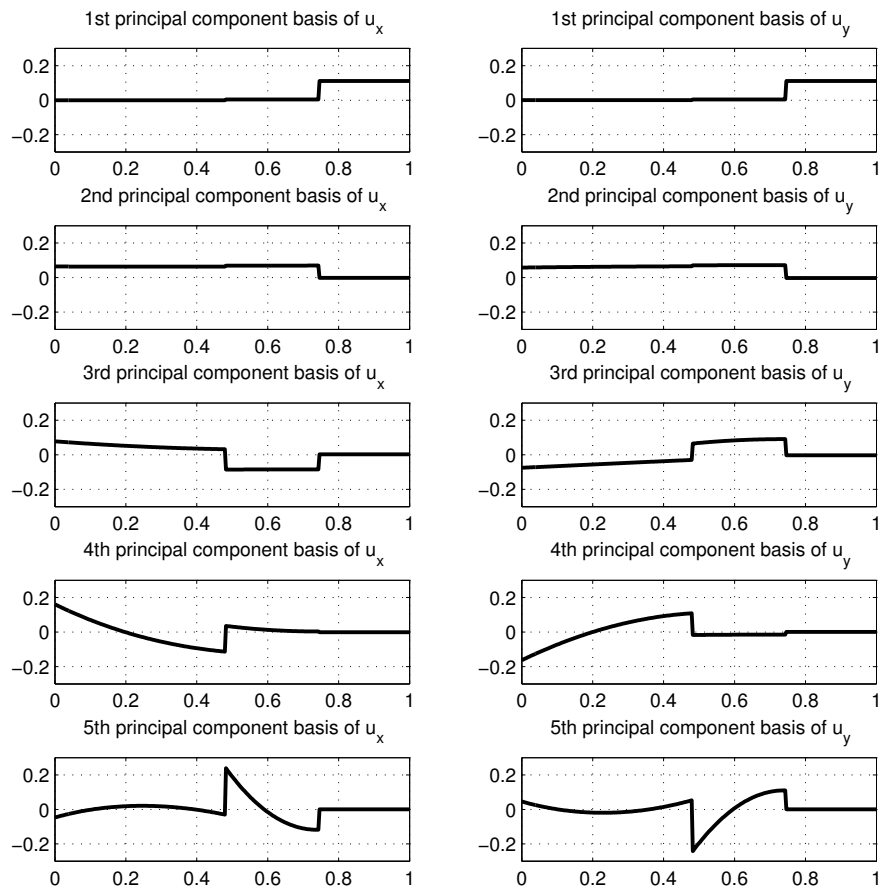


Figure 4.4: PCA bases versus normalized section parameters

#### 4.4.2 Number and Location of Sensors

For the piecewise constant curvature model, the error converges to zero as the number of sensors goes to infinity. For reconstruction models using basis functions, however, both an infinite number of sensors as well as an infinite number of basis functions are needed to guarantee perfect reconstruction. Nevertheless, the performance of reconstruction models using basis functions is far superior to that of the piecewise constant curvature model for small and practical numbers of sensors.

Fig. 4.5 compares the average tip position error over the workspace with respect to the number of sensors. Data for the piecewise constant curvature model is not shown since it is comparatively very large. The solid curves represent the tip position error for the uniformly spaced sensor locations, while the dashed curves are for the optimized sensor locations. When only two sensors are used, the PCA model exhibits the smallest error. As the number of sensors increases, the error of the polynomial model becomes smaller and, while not shown, the errors of both models converge to nonzero lower bounds.

An example of optimized sensor locations is depicted in Fig. 4.6. In this example, the section-based PCA reconstruction model is used with four sensors. The depicted configuration is when Tube 3 is fully extended such that the middle curvature section has zero arclength. As Tube 3 is retracted, this arclength increases from zero and the optimized location of sensor 2 enables measurement of this middle section's curvature for all possible retraction lengths.

#### 4.4.3 Comparison between Reconstruction Models

The accuracy of the reconstruction models can be evaluated using the error functions defined in Eqs. (4.2.19), (4.2.20) and (4.2.21): the curvature shape error, the

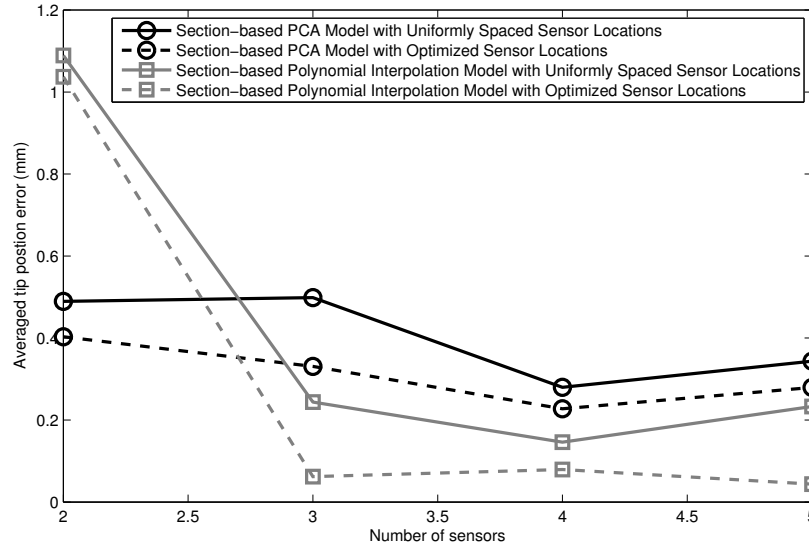


Figure 4.5: Average tip position error over the workspace versus the number of sensors.

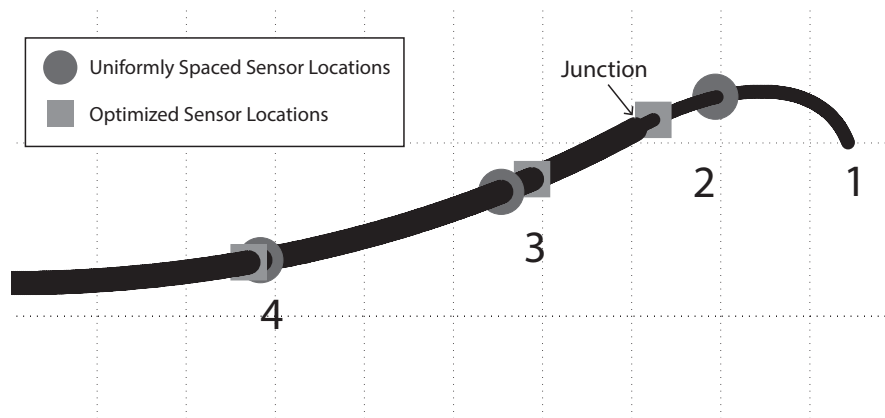


Figure 4.6: Optimized and uniformly spaced locations for four sensors using PCA model. Sensor at robot tip is not shown.

Table 4.2: Average and Maximum Error for Five Sensors

	Piecewise Constant		Section-based PCA		Section-based Polynomial	
	Uniform	Optimized	Uniform	Optimized	Uniform	Optimized
Avg. Tip Position Error (mm)	6.187	3.155	0.343	0.279	0.233	0.044
Max. Tip Position Error (mm)	18.820	14.163	1.838	1.872	1.441	0.527
Avg. Curvature Error ( $m^{-1}$ )	0.832	0.432	0.044	0.040	0.021	0.004
Max. Curvature Error ( $m^{-1}$ )	2.267	1.104	0.197	0.210	0.110	0.034
Avg. Backbone Centerline Error (mm)	0.844	0.518	0.062	0.049	0.045	0.009
Max. Backbone Centerline Error (mm)	2.924	2.177	0.327	0.331	0.247	0.098

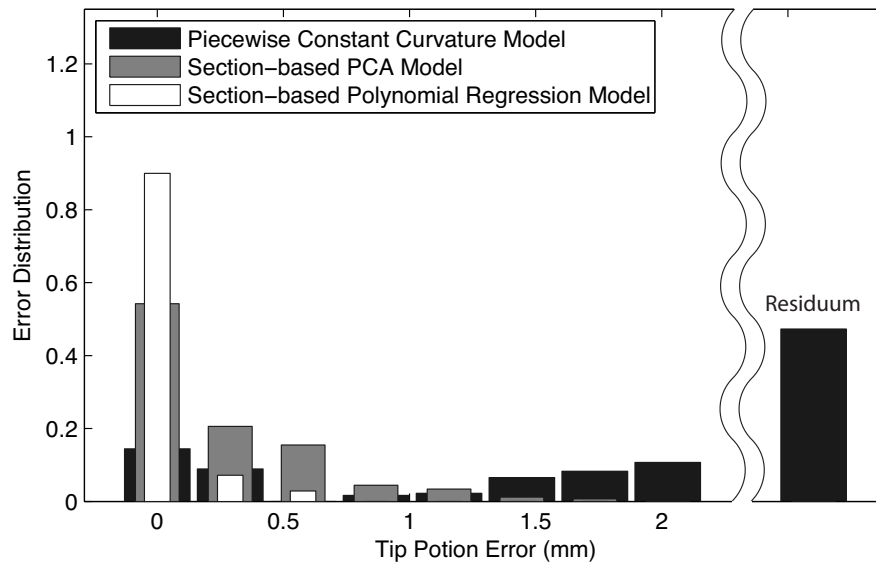


Figure 4.7: Histogram of tip position error for three different reconstruction models

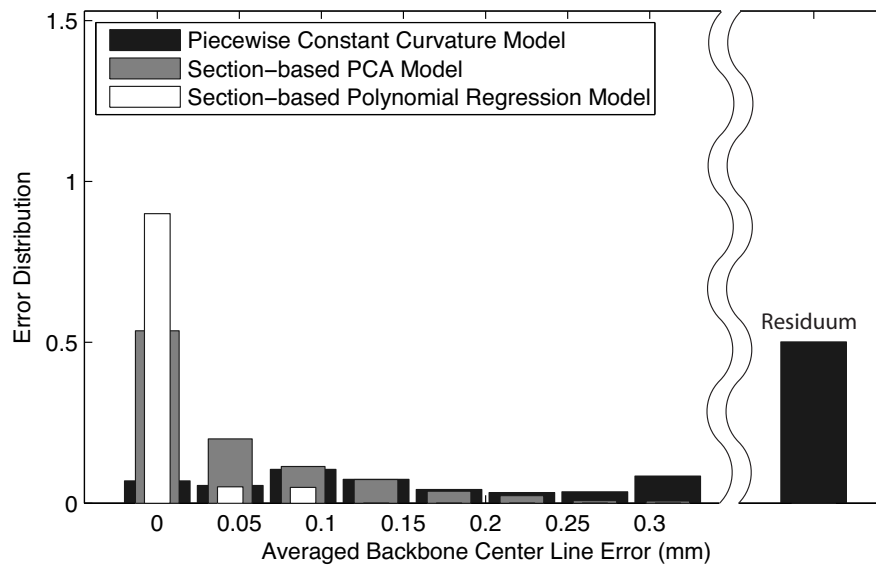


Figure 4.8: Histogram of average backbone centerline error for three different reconstruction models

backbone centerline error and the tip position error. Table 4.2 lists the average and maximum value of these error functions for the specific case of 5 sensors. The section-based polynomial regression model shows the smallest errors for both uniformly spaced and optimized sensor locations, followed by the section-based PCA model. The piecewise constant curvature model is substantially worse than the other models.

Fig. 4.7 shows the histogram of tip position error over the entire workspace. The maximum tip position error of the section-based polynomial regression model is 0.527mm and over 90 percent of workspace samples have errors less than 0.14mm, while the maximum tip position error of the section-based PCA model is 1.87mm and over 74 percent of workspace samples have errors less than 0.43mm. The histogram of backbone centerline error, shown in Fig. 4.8, depicts a similar distribution.



# 5

## Conclusion

### **Achieving Elastic Stability Through Precurvature Optimization**

Prior concentric tube robot designs have considered tubes of piecewise-constant pre-curvature for reasons of simplicity and also since the combined tube shape is approximately piecewise constant. The results of this research demonstrate, however, that stability is enhanced for curvatures that decrease with increasing arc length. In comparison with prior stability results for constant tube pre-curvatures, this approach removes the limits on both tip orientation range and tube length. The price paid for enhanced stability, though, is a larger average robot radius of curvature.

In the approach proposed in [[1]], concentric tube robots are designed as telescoping concatenations of variable and fixed curvature sections. Variable curvature sections correspond directly to the planar tube pairs considered in this research. Consequently, the new stability results can be directly incorporated into this design framework to create designs with larger stable workspaces.

### **Elastic Stability of Concentric Tube Robots Subject to External Loads**

This research presents the first general stability test for concentric tube robots. It applies equally well for robots with tubes of arbitrary number, pre-curvature and stiffness. It also enables the inclusion of any type of external distributed and tip load. Since its evaluation involves solving an initial value problem, it can be computed efficiently. While demonstrated here in the context of stable path planning, the technique can also be used for generating stable robot designs or, if combined with load sensing, could be used to evaluate safety in real time during robot operation.

While the criteria itself was derived by considering the constrained second order variation of the elastic energy function, an intuitive physical interpretation was also developed. It was shown that the stability test is equivalent to ensuring that the Jacobian relating the tip variation in state variables,  $\delta x(b_n)$ , to the variation at  $s$ ,  $\delta x(s)$ , has a nonzero determinant over the length of the robot. Thus, an instability corresponds to the situation in which differential tip motions map to zero magnitude kinematic input motions. This Jacobian is analogous to the inverse of the standard kinematic Jacobian defined in robotics, which maps variations in kinematic inputs to variations in tip motions.

As a metric for distance to instability, the path planning example above employed the magnitude of the Jacobian determinant. Recognizing the analogy with kinematic singularities, however, suggests that any of the various standard measures proposed for distance to a robot singularity [41] can be adapted for use as stability metrics.

### **Optimizing Curvature Sensor Placement for Shape Sensing**

FBG-based curvature sensing represents a promising approach to real-time shape

sensing for continuum robots. The shape reconstruction framework proposed in this research provides a standardized approach to predicting the accuracy of such a sensing system for any continuum robot whose curvatures are piecewise continuous over sections of varying arclength. Using this framework, reconstruction models can be compared and the number of sensors can be selected to meet specific accuracy requirements. In particular, the numerical experiments presented suggest that, in the case of concentric tube robots, high accuracy can be achieved with a small number of sensors. Current research is extending these results to consider the effects of error inherent in the nominal mechanics-based model as well as error in the curvature sensors.

# Bibliography

- [1] P. E. Dupont, J. Lock, B. Itkowitz, and E. Butler. Design and control of concentric-tube robots. *IEEE Trans. Robotics*, 26(2):209–225, 2010.
- [2] D Caleb Rucker, Robert J Webster, Gregory S Chirikjian, and Noah J Cowan. Equilibrium conformations of concentric-tube continuum robots. *The International Journal of Robotics Research*, 29(10):1263–1280, 2010.
- [3] R Xu and RV Patel. A fast torsionally compliant kinematic model of concentric-tube robots. In *Engineering in Medicine and Biology Society (EMBC), 2012 Annual International Conference of the IEEE*, pages 904–907. IEEE, 2012.
- [4] Tomer Anor, Joseph R Madsen, and Pierre Dupont. Algorithms for design of continuum robots using the concentric tubes approach: a neurosurgical example. In *Robotics and Automation (ICRA), 2011 IEEE International Conference on*, pages 667–673. IEEE, 2011.
- [5] J Burgner, P Swaney, R Lathrop, K Weaver, and R Webster. Debulking from within: A robotic steerable cannula for intracerebral hemorrhage evacuation. *IEEE transactions on bio-medical engineering*, 2013.
- [6] Andrew H Gosline, Nikolay V Vasilyev, Evan J Butler, Chris Folk, Adam Cohen, Rich Chen, Nora Lang, Pedro J Del Nido, and Pierre E Dupont. Percutaneous intracardiac beating-heart surgery using metal MEMS tissue approximation tools. *The International journal of robotics research*, 31(9):1081–1093, 2012.

- [7] Nikolay V Vasilyev, Andrew H Gosline, Evan Butler, Nora Lang, Patrick J Codd, Haruo Yamauchi, Eric N Feins, Chris R Folk, Adam L Cohen, Richard Chen, et al. Percutaneous steerable robotic tool delivery platform and metal MEMS device for tissue manipulation and approximation closure of patent foramen ovale in an animal model. *Circulation: Cardiovascular Interventions*, 6(4):468–475, 2013.
- [8] Christos Bergeles and Pierre E Dupont. Planning stable paths for concentric tube robots. In *Intelligent Robots and Systems (IROS), 2013 IEEE/RSJ International Conference on*, pages 3077–3082. IEEE, 2013.
- [9] Pierre E Dupont, Jesse Lock, and Evan Butler. Torsional kinematic model for concentric tube robots. In *Robotics and Automation, 2009. ICRA'09. IEEE International Conference on*, pages 3851–3858. IEEE, 2009.
- [10] DE Kirk. Optimal control theory: an introduction. *Prentice-Hall network series*, 1970.
- [11] Cabada Alberto. An overview of the lower and upper solutions method with nonlinear boundary value conditions. *Boundary Value Problems*, 2011, 2010.
- [12] J. Burgner, D. C. Rucker, H. B. Gilbert, P. J. Swaney, P. T. Russell, K. D. Weaver, and R. J. Webster III. A telerobotic system for transnasal surgery. *IEEE/ASME Trans. Mechatronics*, 19(3):996–1006, 2014.
- [13] L. A. Lyons, R. J. Webster III, and R. Alterovitz. Motion planning for active cannulas. *IEEE/RSJ Int. Conf. Intelligent Robots and Systems*, pages 801–806, 2009.

- [14] L. Lyons, R. Webster III, and R. Alterovitz. Planning active cannula configurations through tubular anatomy. *IEEE Int. Conf. Robotics and Automation*, pages 2082–2087, 2010.
- [15] L. G. Torres, R. J. Webster III, and R. Alterovitz. Task-oriented design of concentric tube robots using mechanics-based models. *IEEE/RSJ Int. Conf. Intelligent Robots and Systems*, 2012.
- [16] C. Bedell, J. Lock, A. Gosline, and P. E. Dupont. Design optimization of concentric tube robots based on task and anatomical constraints. *IEEE Int. Conf. Robotics and Automation*, pages 398–403, 2011.
- [17] N. V. Vasilyev, A. Gosline, A. Veeramani, M.T. Wu, G. Schmitz, R. Chen, V. Arabagi, P. J. del Nido, and P. E. Dupont. Tissue removal inside the beating heart using a robotically delivered metal mems tool. *Int. J. Robotics Research*, 34(2):236–247, 2015.
- [18] RJ Webster, Joseph M Romano, and Noah J Cowan. Kinematics and calibration of active cannulas. In *Robotics and Automation, 2008. ICRA 2008. IEEE International Conference on*, pages 3888–3895. IEEE, 2008.
- [19] Robert J Webster, Joseph M Romano, and Noah J Cowan. Mechanics of precurved-tube continuum robots. *Robotics, IEEE Transactions on*, 25(1):67–78, 2009.
- [20] Steven M LaValle. Rapidly-exploring random trees: A new tool for path planning. 1998.
- [21] C. Bergeles, A.H. Gosline, N.V. Vasilyev, P.J. Codd, P.J. del Nido, and P.E. Dupont. Concentric tube robot design and optimization based on task and

- anatomical constraints. *Robotics, IEEE Transactions on*, 31(1):67–84, Feb 2015.
- [22] Junhyoung Ha, Frank C Park, and Pierre E Dupont. Achieving elastic stability of concentric tube robots through optimization of tube precurvature. In *Intelligent Robots and Systems (IROS 2014), 2014 IEEE/RSJ International Conference on*, pages 864–870. IEEE, 2014.
- [23] Ran Xu, S Farokh Atashzar, and Rajni V Patel. Kinematic instability in concentric-tube robots: Modeling and analysis. In *Biomedical Robotics and Biomechatronics (2014 5th IEEE RAS & EMBS International Conference on*, pages 163–168. IEEE, 2014.
- [24] Richard L. Bishop. There is more than one way to frame a curve. *Amer. Math. Monthly*, 82(3):246–251, March 1975.
- [25] J. Lock, G. Laing, M. Mahvash, and P. E. Dupont. Quasistatic modeling of concentric tube robots with external loads. *IEEE/RSJ Int. Conf. Intelligent Robots and Systems*, pages 2325–2332, 2010.
- [26] D. C. Rucker, B. A. Jones, and R. J. Webster III. A geometrically exact model for externally-loaded concentric-tube continuum robots. *IEEE Trans. Robotics*, 26(5):769–780, 2010.
- [27] Frank C Park and Bryan J Martin. Robot sensor calibration: solving  $ax=xb$  on the euclidean group. *IEEE Transactions on Robotics and Automation (Institute of Electrical and Electronics Engineers);(United States)*, 10(5), 1994.

- [28] Jang-Won Jo and John E Prussing. Procedure for applying second-order conditions in optimal control problems. *Journal of Guidance, Control, and Dynamics*, 23(2):241–250, 2000.
- [29] John E Prussing and Suzannah L Sandrik. Second-order necessary conditions and sufficient conditions applied to continuous-thrust trajectories. *Journal of Guidance, Control, and Dynamics*, 28(4):812–816, 2005.
- [30] J. Ding, R.E. Goldman, K. Xu, P.K. Allen, D.L. Fowler, and N. Simaan. Design and coordination kinematics of an insertable robotic effectors platform for single-port access surgery. *IEEE/ASME Trans. Mechatronics*, pages 1612–1624, 2012.
- [31] Bryan A Jones and Ian D Walker. Kinematics for multisection continuum robots. *IEEE Trans. Robotics*, 22(1):43–55, 2006.
- [32] Hongliang Ren and Pierre E Dupont. Tubular enhanced geodesic active contours for continuum robot detection using 3d ultrasound. pages 2907–2912, 2012.
- [33] Edgar J Lobaton, Jinghua Fu, Luis G Torres, and Ron Alterovitz. Continuous shape estimation of continuum robots using x-ray images. *IEEE Int. Conf. Robotics and Automation*, 2013.
- [34] M. Mahvash and P. E. Dupont. Stiffness control of continuum surgical manipulators. *IEEE Trans. Robotics*, 27(2):334–345, 2011.
- [35] M. Abayazid, M. Kemp, and S. Misra. 3D Flexible Needle Steering in Soft-Tissue Phantoms using Fiber Bragg Grating Sensors. *IEEE Int. Conf. Robotics and Automation*, May 2013.

- [36] Yong-Lae Park, Santhi Elayaperumal, Bruce Daniel, Seok Chang Ryu, Mihye Shin, Joan Savall, Richard J Black, Behzad Moslehi, and Mark R Cutkosky. Real-time estimation of 3-d needle shape and deflection for mri-guided interventions. *IEEE/ASME Trans. Mechatronics*, 15(6):906–915, 2010.
- [37] R. Roesthuis, S. Janssen, and S. Misra. On Using an Array of Fiber Bragg Grating Sensors for Closed-Loop Control of Flexible Minimally Invasive Surgical Instruments. *IEEE/RSJ Int. Conf. Intelligent Robots and Systems*, November 2013.
- [38] R. M. Murray, Z. Li, and S. S. Sastry. *A mathematical introduction to robotic manipulation*. CRC, 1994.
- [39] Richard H Byrd, Mary E Hribar, and Jorge Nocedal. An interior point algorithm for large-scale nonlinear programming. *SIAM Journal on Optimization*, 9(4):877–900, 1999.
- [40] Zsolt Ugray, Leon Lasdon, John Plummer, Fred Glover, James Kelly, and Rafael Martí. Scatter search and local nlp solvers: A multistart framework for global optimization. *INFORMS Journal on Computing*, 19(3):328–340, 2007.
- [41] Bruno Siciliano and Oussama Khatib. *Springer handbook of robotics*. Springer Science & Business Media, 2008.



# 국문초록

최소절개수술은 수술 도구가 작은 구멍을 통과하거나 민감한 조직 주위에 접근하는 경우 등을 동반한다. 컨센트릭 튜브 기술을 이용한 로봇 수술 기구는 얇고 복잡한 곡선 자세를 취할 수 있어 이러한 작업에 매우 적합하다. 그러나 이러한 로봇이 갖는 한가지 문제점은 로봇을 움직이는 도중에 갑자기 발생할 수 있는 탄성 불안정성이다. 튜브들을 돌리거나 밀고 당김에 따라 튜브의 굽힘과 뒤틀림에 의한 탄성 에너지는 점점 쌓이게 된다. 만약 어떠한 자세가 탄성적으로 안정적이지 않다면, 갑작스러운 탄성 에너지 방출로 인해 위험한 회전 동작이 나타날 수 있다.

이 논문에서는 컨센트릭 튜브 로봇의 탄성 안정성을 향상시키기 위해 다음과 같은 두 가지 연구를 수행하였다: i) 튜브 쌍의 최적 설계, ii) 불안정한 자세를 피하기 위한 국소적 안정성 테스트. 첫 번째 연구에서는, 기존의 연구들이 상수 함수 형태의 초기 곡률을 갖는 튜브들만을 고려한 것과 달리, 로봇의 아크 길이를 따라 변하는 초기 곡률 함수를 고려하였고, 이를 통해 탄성 안정성을 최대화하는 최적화 문제를 제시하고 풀었다. 두 번째 연구에서는 주어진 자세가 안정적인 자세인지 불안정한 자세인지를 판별하는 국소적 안정성 조건 및 테스트를 제시한다. 제시된 테스트는 이미 알려진 안정성 연구들의 결과와 비교하여 검증하였으며, 안정적인 동작생성 예제를 통해 그 활용성을 보여주었다.

비록 앞의 두 연구들이 컨센트릭 튜브 로봇의 탄성 불안정성 문제를 해결하는데 큰 도움을 줄 수 있지만, 이 연구들은 모두 이론적인 로봇의 기구학을 기반으로 하고 있다. 로봇을 제어하기 위해서는 이러한 로봇 기구학을 빠르게 풀어내야 하지만 이 기구학은 매우 복잡한 형태를 이루고 있다. 더욱이, 기구학을 통한 자세 계산은 기구학의 파라미터 오차나 모델 단순화 등의 이유로 부정확할 가능성이 있다. 대안으로는 optical fiber Bragg grating 기술을 이용한 국소 곡률 측정 센서는 통한 로봇의 자세 측정 방법이 있다. 이러한 관점에서, 이 논문의 세 번째 연구는

곡률 센서를 통해 자세를 계산해내고, 곡률 센서의 위치와 개수를 결정하기 위한 방법을 제시한다.

**주요어:** 컨센트릭 튜브 로봇, 연속체 로봇, 탄성 안정성, 자세 측정.

**학번:** 2008-22898